Interacting ultracold few-boson systems

Pere Mujal Torreblanca

Phd Thesis

Interacting ultracold few-boson systems

PERE MUJAL TORREBLANCA

Departament de Física Quàntica i Astrofísica

UNIVERSITAT DE
BARCELONA

Interacting ultracold few-boson systems

Programa de Doctorat en Física

PERE MUJAL TORREBLANCA

Directors:

Artur Polls Martí

Bruno Juliá Díaz

Tutor:

Domènec Espriu Climent

Departament de Física Quàntica i Astrofísica

Curs 2018-2019

UNIVERSITAT DE

BARCELONA

Contents

AGRAÏMENTS

Primer de tot, vull agrair als meus directors, l'Artur i el Bruno, tot el seu suport al llarg de tots aquests anys. Des que, per sort meva, vaig decidir de fer el treball final de màster amb ells fins ara mateix. Treballar amb vosaltres és reconfortant i això fa molt més fàcil l'aprenentatge. Us vull agrair també els vostres esforços i totes les oportunitats que m'heu donat.

Vull donar les gràcies pel bon ambient de feina als companys de despatx que he tingut. També a tota la resta de personal del departament de Física Quàntica i Astrofísica que sempre han estat amables quan els he necessitat. Especialment als membres del grup de física atòmica i nuclear.

A nivell professional vull destacar dues persones de les quals n'he après molta física. El Sebastiano Pilati, que va encoratjar-nos a col·laborar amb ell, i la Doerte Blume, que em va acollir al seu grup i em va transmetre el seu rigor.

A qui també he d'agrair haver pogut fer aquesta tesi és als meus amics, que m'han donat les estones d'esbarjo i l'estima que necessitava per poder afrontar els reptes que m'ha plantejat aquesta tesi.

Finalment, l'agraïment més gran el vull reservar per tota la meva família. Sense ella res d'això no hauria estat possible. Sempre he tingut tot el seu suport en tots els sentits.

RESUM

En aquesta tesi, estudiarem les propietats físiques de diversos sistemes de pocs bosons ultrafreds depenent de les interaccions entre els seus constituents. Avui dia, a nivell experimental, es té un gran control amb una gran precisió de la geometria i les interaccions entre les partícules, fet que fa aquest sistemes excel·lents per comprovar de forma directa els principis de la mecànica quàntica. Un punt d'interès és comprovar l'evolució de les seves propietats amb el nombre de partícules. L'estudi teòric d'aquests sistemes pretén entendre a nivell microscòpic els resultats experimentals actuals i donar suport pels nous avenços experimentals.

El mètode que farem servir serà la diagonalització exacta del hamiltonià del sistema. Com veurem, malgrat les millores que es poden implementar, ens trobarem amb la limitació de no poder estudiar sistemes de més d'unes quantes partícules. Els avantatges d'aquest mètode són diversos. En primer lloc, podrem obtenir no només l'estat fonamental del sistema sinó que també els primers estats excitats. En segon lloc, el mètode és variacional i sabem que convergeix cap a la solució exacta a mesura que ampliem l'espai de Hilbert en que diagonalitzem. A més a més, en tenir accés als estats del sistema, podem calcular qualsevol quantitat observable que sigui d'interès.

Primerament, estudiarem un sistema de bosons sense espín atrapats en un potencial harmònic bidimensional. L'efecte de la trampa és de mantenir el sistema lligat. En haver-hi una interacció repulsiva, veurem com canvia l'espectre d'energia del sistema i també altres propietats. Per exemple, la seva densitat, que habitualment es pot mesurar, i també la funció de distribució de dos cossos, que va íntimament lligada a l'existència de correlacions.

Tot seguit, ens centrarem en el cas particular de tenir només dos bosons en el sistema interaccionant a través d'una gran força repulsiva. Inspirats pel cas unidimensional en que té lloc el fenomen de la fermionitzсió en el limit d'interacció molt forta, estudiarem si en el cas bidimensional hi queda cap reminiscència d'aquest efecte. En altres paraules, analitzarem si hi ha propietats dels dos bosons fortament interactuants en dues dimensions que siguin com les de fermions no interactuants en el mateix sistema.

A continuació, tractarem el fenomen de la localització en un sistema unidimensional en el qual hi ha un potencial extern de tipus *speckle* que introdueix desordre en el sistema. Veurem que la localització és un fenomen robust en front de les interaccions repulsives.

Per últim, estudiarem la influència de l'espín-òrbita en un sistema de bosons amb dues components de pseudoespín, associades, per exemple, a dos nivells hiperfins, atrapats en un potencial harmònic bidimensional. Presentarem un anàlisi exhaustiu dels efectes conjunts de la interacció i l'espín-òrbita en l'espectre i en les propietats del sistema. En particular, mostrarem l'existència d'un encreuament en l'estat fonamental del sistema susceptible de ser identificat experimentalment.

ABSTRACT

In this thesis, we study the physical properties of several ultracold few-boson systems depending on the interactions between their constituents. Nowadays, experimentally, it is possible to have great control with high precision over the geometry and the interactions between the particles, making them an excellent setup to test directly the principles of quantum mechanics. A very interesting point is to study the evolution of their properties with the number of particles. The theoretical study of these systems pretends to microscopically understand the current experimental results and give support to new experimental developments.

The method that will be used is the exact diagonalization of the Hamiltonian of the system. As we will see, in spite of the attempts to improve it, the method is limited by the fact that, in practice, it is only useful to study few-particle systems. The method has several advantages. First of all, one has access to both the ground and the excited states. In second place, the method is variational and converges to the exact solution as long as the Hilbert space in which we diagonalize is enlarged. Moreover, since we have access to the states of the system, it is possible to calculate any observable quantity of interest.

First, we will study a system of spinless bosons trapped in a two-dimensional harmonic potential. The effect of the trap is to keep the system bound. It will be seen how the presence of a repulsive interaction changes the energy spectrum and other properties of the system. For instance, the density profile, which is usually measurable, and also the two-body distribution function, which is intimately related to the existence of correlations.

Afterwards, the focus will be on the particular case of having only two bosons in the system interacting through a strong repulsive force. Inspired by the one-dimensional case where the fermionization phenomenon takes place in the strongly-interacting limit, we will study whether in two dimensions there is a resembling reminiscent effect. In other words, we will analyze if there are properties of the two strongly-interacting bosons in two dimensions that are like the ones of two noninteracting fermions.

After that, we will tackle the localization phenomenon in a one-dimensional system that is caused by an external speckle potential that introduces disorder in the system. We will show that the localization is a robust phenomenon against repulsive contact interactions.

Finally, we will study the influence of the spin-orbit coupling in a system of bosons with two possible pseudospin components, associated, for instance, to two hyperfine levels, confined in a two-dimensional harmonic trap. We will present an exhaustive analysis of the combined effects of the interaction and the spin-orbit coupling in the spectrum and the properties of the system. In particular we show the existence of a crossover in the ground state of the system susceptible to be experimentally identified.

Chapter 1

INTRODUCTION

The main goal of this doctoral thesis is to study the effect of interactions in ultracold few-boson systems. In particular, four topics are analyzed: i) the formation of quantum correlations between the particles; ii) the fermionization of interacting bosons in two dimensions; iii) the few-body localization in a one-dimensional system with a speckle potential; and iv) spin-orbit coupling effects in interacting ultracold bosons in a two-dimensional harmonic trap. From a theoretical point of view, ultracold means that the temperature is fixed at absolute zero, thus temperature effects are not considered. We are interested in the ground state and the low-energy spectrum of these systems. To this aim, we have developed an exact diagonalization method that allows to obtain their eigenstates and eigenenergies. In addition, we have performed perturbative and variational calculations with trial correlated wave functions to enlighten the physics of these systems.

A major motivation to study ultracold atomic systems is the rapid experimental advances in the field. In particular, it is noticeable the high control that the experimentalists have over the geometry and interactions between the particles. Presently, the strength of the interactions has a wide range of variation, from being attractive to repulsive using Feshbach resonances [1]. Traditionally, weak interactions have been treated in mean-field approximations [2]. However, strongly-interacting regimes present in current experiments generate correlations beyond mean field. The proper theoretical description of these systems requires the use of sophisticated many-body methods [3]. That serves to understand the structure of the system and also to propose new experiments.

Atoms are usually prepared in a trap, that is engineered using magnetic and optical fields. In particular, the use of optical laser fields have opened up many possibilities. With it, it is possible

to create different trapping potentials. For instance, with two counter-propagating beams forming a standing wave an optical lattice is built [4]. Moreover, with appropriate laser configurations and taking advantage of the fact that the intensity of the laser is tunable, the atoms can be arranged in an effective one- or two-dimensional system, just tightly confining them in the desired directions [5].

In addition, the variety is also reflected in the fact that both fermionic and bosonic species are experimentally available and one can explore different statistics, including mixtures.

Apart from the experimental advances in the preparation and manipulation of these systems, a significant achievement is the improvements to measure their properties. Nowadays, the detection of single atoms is a reality [6] with a high resolution, by detecting its fluorescent emitted light. For instance, this allows to directly measure two-body correlations between atoms. It is also relevant the control over the number of particles, which allows to study quantum properties of few-body systems [7]. The interpretation and analysis of these experiments make necessary the theoretical microscopic calculations of these systems [8].

Another important feature of ultracold atomic systems is that they are sufficiently isolated to maintain quantum coherence. Therefore, time-evolution studies in these systems are performed and there are efforts to use that in the implementation of quantum protocols to efficiently produce interesting states for potential applications [9, 10].

In short, there are multiple reasons to consider ultracold atoms an excellent platform to study quantum systems. In particular, an interesting idea is to use them as quantum simulators [11, 12]. Quantum simulators are quantum systems that are prepared and controllable in the laboratory which can be used to describe (simulate) an analogous system whose properties are impossible to calculate.

The thesis is organized as follows. In Chapter 2, we introduce the formalism and explain in detail the diagonalization method and the improvements that we have proposed to optimize the Fock space and obtain reliable results with reduced Hilbert spaces. In Chapters 3–6, we report and discuss the main results obtained in each studied system. Below, we introduce these systems. Finally, the conclusions and summary of this thesis are found in Chapter 7.

Chapter 3 is mostly based on the article [13], published in Physical Review A. In this paper, we studied the properties of two, three, and four identical bosons interacting through a finite-range interaction confined in a two-dimensional isotropic harmonic trap.

The problem of a particle trapped in a harmonic trap is one of the best-known quantum systems. Going from a single particle to a system composed of N interacting particles is, however, far more involved. Interestingly, recent advances in ultracold-atomic gases have opened the possibility of studying systems of a few atoms, either fermions or bosons, trapped in potentials of different

kinds [7, 14–16].

For the bosonic case, there have been very interesting results in one dimension, where the fermionization of the bosonic gas was recognized by Tonks and Girardeau [17] for the case of infinitely repulsive bosons and later confirmed experimentally in ultracold atomic gases [18,19]. There are many works studying fermionization in one dimension, for instance, in optical lattices [20], in few-atom mixtures [21–23], for attractive interactions [24] and for few dipolar bosons [25]. In other cases, the focus is on quantum correlations [26, 27] and their effects in mixtures of distinguishable and identical particles [28] or in the construction of analytic ansatz to capture the physics in all interaction regimes [29].

The case of two particles with contact interactions was considered in one, two, and three dimensions in Ref. [30]. There, they obtained semianalytic results, finding the energies and wave functions as a solution of transcendental equations. More general cases of few-body systems have been studied mostly in three dimensions; see Ref. [8] and references therein.

In two dimensions, semianalytical approximate solutions to the case of two bosons with finite range interactions have been presented in Ref. [31]. Other two-dimensional works include two- and three-body exact solutions for fermions and bosons with contact interactions [32], fast-converging numerical methods for computing the energy spectrum for a few bosons [33], the study of finite-range effects [34,35] and universality [36–39], condensation in trapped few-boson systems [40], and interacting few-fermions systems [41, 42].

In this Chapter, we study with exact diagonalization the energy spectrum for the two-, three-, and four-boson systems depending on the interaction strength. The analysis is completed by using perturbation theory for weak interactions and it is extended to the strongly-interacting regime by introducing correlated variational ansatzes. In particular, we focus on the formation of correlations and explain the breaking of degeneracies in the energy spectrum. In addition, we characterize the ground state of the system by means of computing some representative properties, i.e., the different energy contributions, the density profile, the condensed fraction and the pair-correlation function.

In Chapter 4, we have revised and extended the contents of the article [43], published in Condensed Matter. In this paper, we compared the numerical calculations for the ground state of two interacting bosons in two dimensions with a short-range interaction with the properties obtained from the analytical wave functions that describe two noninteracting bosons, two noninteracting fermions, and the corresponding symmetrized wave function. The main purpose is to show if some of the properties of the interacting two-boson system resemble the noninteracting fermionic ones.

In one dimension, the Bose–Fermi mapping [17] theorem relates the ground state energy and the wave function of strongly interacting bosons with those corresponding to noninteracting fermions in the same trapping potential. Several works have discussed the onset of the Tonks–Girardeau

regime in one dimension [14, 15, 18–30, 44–46].

In contrast, in two or more dimensions, the theorem does not apply. However, the emergence of correlations between the particles due to the repulsive character of the interaction that we have found in the previous Chapter encourages us to study further the properties of the two-body system. Therefore, we have performed an exhaustive study of the possible existence of a certain mapping between bosons and fermions in two dimensions.

In this Chapter, we have carried out calculations using explicit variational wave functions that allow to understand the mechanism [47] that the particles use to avoid the repulsive interactions and to discuss the similarities and differences compared with the one dimensional case.

Chapter 5 is based on the article [48], published in Physical Review A. Since Anderson's 1958 seminal article [49], it is known that disorder can induce localization of noninteracting quantum particles. If and when Anderson localization can be stable against inter-particle interactions has been an outstanding open question ever since [50–52]. In recent years, this question has been addressed in innumerable theoretical articles, putting forward the theory of so-called many-body localization [53, 54]. This phenomenon is expected to occur in isolated one-dimensional systems with disorder.

While some previous theoretical predictions on many-body localization, based mostly on perturbative calculations, considered continuous-space models [53–56], most numerically-exact simulations considered one-dimensional discrete-lattice models within the tight binding formalism. In fact, whether many-body localization can occur in a continuum is still a controversial issue. In Ref. [57], it is claimed that many-body localization can occur even in continuous-space systems if the (non-deterministic) disorder is in the impurity limit, but it might be unstable if the correlation length of the disorder is finite. Ref. [58], instead, states that many-body localization cannot occur at all in a continuum. On the other hand, the continuous-space simulations of Ref. [59], which considered fermionic atoms in a quasi-periodic (hence, deterministic) potential and were based on time-dependent density functional theory within the adiabatic approximation, displayed one of the experimental hallmarks of many-body localization, namely the long-time persistence of an initially imprinted density pattern. This phenomenon has indeed been observed in the cold-atom experiments on many-body localization [60–62]. Resolving this controversy is essential. In this Chapter, we shed some light on this issue, considering a few-body setup. Specifically, it describes bosonic atoms in a one-dimensional continuum, interacting via a repulsive zero-range interaction. The atoms are exposed to the spatially correlated random potential corresponding to the disorder pattern that is generated when an optical speckle field is shone onto the atomic cloud. Due to the higher computational cost of continuous-space models, we focus on one-, two-, and three-boson systems. The main goal of our analysis is to verify whether localization is stable against the re-

pulsive contact inter-particle interaction, meaning that many-body localization can be observed in a few-body setup. Indeed, many-body localization has recently been experimentally identified for relatively small systems of eight atoms [63]. Previous theoretical studies investigated interaction effect in continuous-space bosons within the Gross-Pitaevskii theory [64, 65].

In this Chapter, we do an intensive use of the diagonalization method to find the spectrum and perform a statistical analysis of the energy levels over different speckle potentials to elucidate on the presence of localized states.

Chapter 6 is based on the article [66], which has been submitted for publication to Physical Review A. We make use of analytical approaches and numerical diagonalization techniques in order to describe the trapped single-particle and two-boson systems in the presence of Rashba spin-orbit coupling.

Spin-orbit coupling in ultracold atoms [67–72] has been an issue of great interests in the last years in the atomic physics community. Since the first experiment was carried out successfully [73] dressing the atoms with two Raman lasers, other works were performed. For example, studying temperature effects [74] or engineering the spin-orbit coupling in alternative ways: with a gradient magnetic field [75]; and within optical lattices [76–78]. Interesting phenomena have been observed in spin-orbit coupled systems, for instance, a negative effective mass [79].

In the absence of a confining potential, in a homogeneous system, the single-particle energy dispersion relation is simple and the Hamiltonian is solvable in momentum space in the presence of spin-orbit coupling. In that case, and at zero temperature, for the many-body system two phases were predicted in Ref. [80], the plane wave phase and the standing wave phase. The transition from one phase to the other was characterized depending on the inter and intraspecies interactions between the atoms. Further studies exploring the phase diagram of spin-orbit coupled Bose-Einstein condensates have been done within a mean-field description [81], studying the stability of the system in the presence of quantum and thermal fluctuations [82–86].

However, in the presence of a confining harmonic trap, the situation is fairly different due to the introduction of a new characteristic length and the fact that the momentum is no longer a good quantum number. At the single-particle level, even when the spin-orbit coupling is strong, the spectrum remains discrete, forming a Landau-level-like structure [87–91], which is altered when the trap is anisotropic [92, 93]. At the mean-field level, more phases, like a half-quantum vortex state, are found in the trapped system [87–89, 91, 94–96].

The inclusion of interactions between the atoms adds an additional challenge, specially in the strongly interacting regime [97–100], where quantum correlations are expected to dominate the physics [101]. Under these circumstances, it is evident that microscopic methods that go beyond mean field are required [102]. In this sense, the exact diagonalization provides a good tool to unveil the nature of the correlations present in the system. We derive the virial theorem in the presence of

spin-orbit and also check its fulfillment as a proof of the accuracy of the results. The contributions to the total energy of the different parts of the Hamiltonian serve to understand the interplay of the spin-orbit and the interaction terms. Moreover, the density profile of the system is also notably affected by them.

Chapter 2

METHODOLOGY AND FORMALISM

The methods used in this thesis to unveil the nature of different few-boson systems considered are analytic perturbation theory, variational Monte Carlo and exact diagonalization. In general, perturbative expansions only work for fairly small interactions and rarely capture the correlations appearing in the system. They are developed specifically for some of the problems considered. In Chapters 3 and 4, variational Monte Carlo methods are employed with a multiparametric wave function. In this way, fairly good upper bounds for the ground-state energy are obtained together with a clear physical interpretation of the results. The variational Monte Carlo method only allows us to study ground-state properties. To go beyond that, we resort to exact diagonalization techniques in Chapters 3, 4, 5, and 6. For this purpose, we make use of the ARPACK library that implements the Lanczos algorithm, that allows to find the lowest eigenvalues of a matrix and their corresponding eigenvectors. In general, the systems that we consider are described in a Hilbert space of infinite dimension. For this reason, the diagonalization in a finite Hilbert subspace provides approximations to the eigenstates and eigenenergies of the Hamiltonian. The method relies on the convergence of the approximate values to the exact ones by increasing the dimension of the Hilbert space in which the diagonalization is performed. In any case, the resulting eigenenergies are upper bounds to the exact ones because for any size of the subspace the method keeps its variational properties. After the diagonalization, due to the fact that we obtain also the eigenstates of the system, in principle, we have access to any observable quantity that can be computed numerically.

In the following sections, the second-quantized formalism used to implement the diagonalization method in a truncated Hilbert space is extensively explained. First of all, in Sec. 2.1, we present the general form of the Hamiltonians that are found in the other Chapters. After that, in Sec. 2.2, we introduce the Fock states that are built populating single-particle states with bosons and describe

how the many-body basis is constructed in Sec. 2.3. Later on, in Sec. 2.4, we discuss the degeneracies of the system in the noninteracting limit and their consequences when we increase the number of particles. Finally, we introduce the basis employed for both the two-dimensional and one-dimensional systems of bosons in Sec. 2.5 and Sec. 2.6, respectively.

2.1 The second-quantized Hamiltonian of a system of interacting bosons

In general, the Hamiltonian is decomposed in two pieces,

$$\hat{H} = \hat{H}_0 + \hat{H}_{\text{int}} . \tag{2.1}$$

In order to write explicitly each part of the Hamiltonian, we introduce the following creation and annihilation operators, $\hat{a}_i$ and $\hat{a}_j^\dagger$, associated to a single-particle basis, that fulfill the commutation relations

$$\begin{aligned} [\hat{a}_i, \hat{a}_j^\dagger] &= \delta_{ij} , \\ [\hat{a}_i, \hat{a}_j] &= [\hat{a}_i^\dagger, \hat{a}_j^\dagger] = 0 . \end{aligned} \tag{2.2}$$

The symmetry of the full system of bosons under the exchange of any pair of particles is guaranteed by these commutation relations. All in all, this procedure is equivalent to the use of symmetrized wave functions for bosons in the first-quantization formalism. The subindex i of an operator indicates in which single-particle state, $|\psi_i\rangle$, the bosons are created or annihilated. The set of states $\{|\psi_i\rangle\}$, with $i = 1, 2, ...$, form an orthonormal basis of the single-particle Hilbert space.

The first piece of the Hamiltonian in Eq. (2.1) corresponds to the single-particle part,

$$\hat{H}_0 = \sum_{i,j} \epsilon_{ij} \, \hat{a}_i^\dagger \hat{a}_j . \tag{2.3}$$

The coefficients ϵ_{ij} depend on the single-particle basis chosen and are computed as

$$\epsilon_{ij} = \langle \psi_i | \hat{H}_{\text{sp}} | \psi_j \rangle , \tag{2.4}$$

where $\hat{H}_{\text{sp}}$ is the Hamiltonian of the single-particle system. Eventually, one can use a basis where $\hat{H}_0$ is diagonal.

The second piece,

$$\hat{H}_{\text{int}} = \frac{1}{2} \sum_{i,j,k,l} v_{ijkl} \, \hat{a}_i^\dagger \hat{a}_j^\dagger \hat{a}_k \hat{a}_l , \tag{2.5}$$

is the interaction part. In the present work, we consider two-body interaction potentials, $\hat{v}$, in all cases. Consequently, $\hat{H}_{\text{int}}$ is a two-body operator. In this case, the interaction coefficients are given by:

$$v_{ijkl} = \langle \psi_i | \langle \psi_j | \hat{v} | \psi_k \rangle | \psi_l \rangle . \tag{2.6}$$

The formalism described in this section is applicable to any system of identical bosons with two-body interactions, regardless of the dimension of the real space or the internal degrees of freedom of the particles. In particular, in next Chapters, we will study one-dimensional and two-dimensional systems. The explicit forms of the single-particle Hamiltonian and the two-body potential will be given in each particular case, together with the considered single-particle basis.

2.2 The many-body Fock space

Once the single-particle basis is selected, the next step is to fix the number of states of this basis. In other words, we truncate the basis so that only the first M states, $|\psi_1\rangle, ..., |\psi_M\rangle$, in order of increasing energy, ϵ_{ii}, given by Eq. (2.4), are kept. Those chosen single-particle states are the ones that the bosons are allowed to populate. Notice that the truncation is based on an energy criterion as long as the focus of our interest is on the lowest-energy physics of the systems. This truncation is reflected in the Hamiltonian by the fact that the sums run over a finite number of single-particle states; Eqs. (2.3) and (2.5) are replaced, in practice, by:

$$\hat{H}_0 = \sum_{i,j=1}^{M} \epsilon_{ij}\, \hat{a}_i^\dagger \hat{a}_j, \tag{2.7}$$

and

$$\hat{H}_{\text{int}} = \frac{1}{2} \sum_{i,j,k,l=1}^{M} v_{ijkl}\, \hat{a}_i^\dagger \hat{a}_j^\dagger \hat{a}_k \hat{a}_l, \tag{2.8}$$

respectively.

The Fock states are constructed by adding particles to the vacuum state, $|\text{vac}\rangle \equiv |0, ..., 0\rangle$. In terms of creation operators, they are defined as

$$|n_1, ..., n_M\rangle \equiv \frac{(\hat{a}_1^\dagger)^{n_1} \cdots (\hat{a}_M^\dagger)^{n_M}}{\sqrt{n_1! ... n_M!}}\, |\text{vac}\rangle, \tag{2.9}$$

where n_i is the number of bosons populating the single-particle state $|\psi_i\rangle$. The factor $1/\sqrt{n_1! ... n_M!}$ ensures that they are normalized to unity and orthogonal to each other:

$$\langle n_1', ..., n_M'|n_1, ..., n_M\rangle = \delta_{n_1', n_1} \cdots \delta_{n_M', n_M}. \tag{2.10}$$

In all cases, we consider a fixed number of particles, N. Accordingly, the quantum numbers in each Fock state are constrained by the conservation of the total atom number,

$$\sum_{i=1}^{M} n_i = N. \tag{2.11}$$

The connection between Fock states and their equivalent first-quantized representation is shown in the following examples. For instance, the Fock state $|\Psi\rangle = |N, 0, ..., 0\rangle$, would be written in first-quantized notation as the product state $|\Psi\rangle = |\psi_1\rangle \cdots |\psi_1\rangle = |\psi_1\rangle^{\otimes N}$. A more illustrative example,

where the second-quantization formalism simplifies the notation, is considering the Fock state $|\Psi\rangle = |N - 1, 1, ..., 0\rangle$. In first-quantized notation it would be written as $|\Psi\rangle = \frac{1}{\sqrt{M}}(|\psi_2\rangle |\psi_1\rangle \cdots |\psi_1\rangle + |\psi_1\rangle |\psi_2\rangle |\psi_1\rangle \cdots |\psi_1\rangle + ... + |\psi_1\rangle \cdots |\psi_1\rangle |\psi_2\rangle)$, as we need to take into account the symmetric character of the state under the exchange of two particles.

The action of creation and annihilation operators on a Fock state is the following:

$$\hat{a}_i^\dagger |n_1, ..., n_M\rangle = \sqrt{n_i + 1} |n_1, ..., n_i + 1, ..., n_M\rangle \, ,$$
$$\hat{a}_i |n_1, ..., n_M\rangle = \sqrt{n_i} |n_1, ..., n_i - 1, ..., n_M\rangle \, . \tag{2.12}$$

The Fock states are our starting point before setting the many-body basis of our many-body Hilbert space. The conventional approach [103] uses all Fock states for the N-boson system and M single-particle states. That results in a Hilbert space of dimension

$$D_N^M = \frac{(M + N - 1)!}{(M - 1)! N!}, \tag{2.13}$$

which, for instance, in the cases $N = 2, 3,$ and 4, gives, respectively,

$$D_2^M = \frac{M(M + 1)}{2},$$
$$D_3^M = \frac{M(M + 1)(M + 2)}{6}, \tag{2.14}$$
$$D_4^M = \frac{M(M + 1)(M + 2)(M + 3)}{24}.$$

Notice that, even for a system of few bosons, the dimension of the Fock space grows rapidly with M. In our calculations, we need to increase M in order to obtain well-converged results in the presence of interactions between the particles. In practice, this issue is a real problem, because our computational resources in terms of memory and computational time are finite. However, we will show in the following section how to construct the many-body basis so that with smaller Hilbert spaces we are able to have well-converged results.

2.3   The many-body Hilbert space basis

For systems of more than one particle, we are usually interested in the lowest-energy physics. Consequently, we will consider Fock states with a noninteracting energy smaller than a given maximum energy of the noninteracting system. More precisely, for each Fock state, we compute the energy

$$E_{|n_1, ..., n_M\rangle} = \langle n_1, ..., n_M| \hat{H}_0 |n_1, ..., n_M\rangle = \sum_{i=1}^{M} \epsilon_{ii} \, n_i. \tag{2.15}$$

Following the approach in Ref. [104], the many-body basis is set taking the Fock states whose energy, $E_{|n_1, ..., n_M\rangle}$, is lower than a given cutoff, $E_{\max}$. Namely, we use the following energy criterion:

$$E_{|n_1, ..., n_M\rangle} \leqslant E_{\max}, \tag{2.16}$$

in order to truncate the many-body Hilbert space. The efficiency of the method for the description of the lowest part of the spectrum is also shown in Ref. [104]. In fact, one can use smaller Hilbert spaces without spoiling the quality of the results.

To better understand the procedure, it is more convenient to express the criterion in terms of noninteracting excitation energies in order to relate the truncation of the single-particle basis, determined by M, to the truncation of the many-body basis. For this purpose, we use the Fock state with less energy, the state $|N, 0, \dots, 0\rangle$, to establish an energy reference and rewrite (2.16) as

$$E^{\text{exc}}_{|n_1, \dots, n_M\rangle} \leqslant E^{\text{exc}}_{\text{max}}, \tag{2.17}$$

where $E^{\text{exc}}_{|n_1, \dots, n_M\rangle} = E_{|n_1, \dots, n_M\rangle} - E_{|N, 0, \dots, 0\rangle}$ and $E^{\text{exc}}_{\text{max}} = E_{\text{max}} - E_{|N, 0, \dots, 0\rangle}$. The number of single-particle modes, M, used is the minimal one that is required in order to include all the Fock states that accomplish the energy criterion in (2.17). Therefore, the truncation of the many-body basis determines the truncation of the single-particle basis. The Fock state with the largest energy that is included is the state $|N - 1, 0, \dots, 1\rangle$, with only one particle in the Mth mode. Consequently, its excitation energy is the maximum one reached,

$$E_{|N-1, 0, \dots, 1\rangle} - E_{|N, 0, \dots, 0\rangle} = \epsilon_{MM} - \epsilon_{11} = E^{\text{exc}}_{\text{max}}, \tag{2.18}$$

that is used to find the value of M once $E^{\text{exc}}_{\text{max}}$ is fixed. The explicit dependence of ϵ_{MM} on M is determined by the particular choice of the single-particle basis.

2.4 Degeneracies of noninteracting systems and many-body Hilbert space dimension

In this section, we determine the many-body Hilbert space dimension when it is constructed following the procedure described above. In the present section, we consider the single-particle basis formed by the set of eigenstates of $\hat{H}_{\text{sp}}$, so the single-particle part of the Hamiltonian is diagonal,

$$\hat{H}_0 = \sum_{i=1}^{M} \epsilon_i \, \hat{a}_i^\dagger \hat{a}_i, \tag{2.19}$$

and ϵ_i is the eigenenergy corresponding to the single-particle state $|\psi_i\rangle$. Then, at the many-body level, the Fock states are eigenstates of $\hat{H}_0$, so they are the eigenstates of the noninteracting system of bosons,

$$\hat{H}_0 |n_1, \dots, n_M\rangle = \sum_{i=1}^{M} \epsilon_i \, n_i |n_1, \dots, n_M\rangle = E |n_1, \dots, n_M\rangle, \tag{2.20}$$

where $E = \sum_{i=1}^{M} \epsilon_i \, n_i$.

The arguments presented above would also hold if $\hat{H}_0$ is not diagonal, since we can always write it as a diagonal part plus a non-diagonal one,

$$\hat{H}_0 = \hat{H}_0^{\mathrm{d}} + \hat{H}_0^{\mathrm{nd}}, \tag{2.21}$$

with $\hat{H}_0^{\mathrm{d}} = \sum_{i=1}^{M} \epsilon_{ii}\, \hat{a}_i^\dagger \hat{a}_i$, and $\hat{H}_0^{\mathrm{nd}} = \sum_{i\neq j, j=1}^{M} \epsilon_{ij}\, \hat{a}_i^\dagger \hat{a}_j$. Then, the discussion would refer to $\hat{H}_0^{\mathrm{d}}$ and its eigenstates, despite the fact that it would not describe all the effects present in the noninteracting system.

In general, using the method of building the many-body basis described previously, we do not know an expression, analogous to Eq. (2.13), that tells us the Hilbert space dimension given the number of bosons N and the number of single-particle modes M. The reason is that we have to care about the single-particle energies and their degeneracies that, together with the bosonic statistics of the many-body states, determine the degeneracies of the many-body states. However, we can state some general characteristics, distinguishing two possible situations, before we concentrate on specific cases.

The first situation is when the first single-particle state of the basis, $|\psi_1\rangle$, that has the smallest energy ϵ_1, is non-degenerate with the others. We assume that other degeneracies of the energies might be present for the rest of the states of the single-particle basis but the number of degenerate states is always finite. With these conditions, the Fock state $|N, 0, ..., 0\rangle$ is the non-degenerate ground state of the noninteracting system, that we label with $K_E = 0$. The higher-energy states of the many-boson system can be degenerate, and we label with K_E each manifold of degenerate excited states, with $K_E = 1, 2, ...$. The number of degenerate states in each manifold, d_{K_E}, has a maximum $d_{K_E}^{\mathrm{max}}$, that is reached when the total number of bosons, N, is equal or larger than a particular value, N_{K_E}, that depends on the manifold.

Theorem 2.1. $d_{K_E} = d_{K_E}^{\mathrm{max}} \iff N \geqslant N_{K_E}$

Proof. From left to right, the excited states are obtained by promoting particles to higher-energy modes. Since the number of degenerate single-particle states is finite, there is a finite number of ways to populate states with bosons and obtain the same energy E. Consequently, there is a maximum value for the number of degenerate states. If the maximum degeneracy is reached, the number of bosons of the system has to be sufficiently big in order to include all possible combinations of populating single-particle states that build Fock states with the same energy. From right to left, if the number of bosons is sufficiently large, increasing it does not change the degeneracy of a given manifold, since it does not introduce new possible ways of arranging the bosons and obtaining the same energy but the old ones remain there. Therefore, we have reached the maximum degeneracy in that energy manifold. $\square$

The main feature of this kind of systems is that the degeneracy of the lowest-energy states is independent of the number of particles of the system if this number is above a certain value.

The second situation is found when the first single-particle state of the basis, $|\psi_1\rangle$, is degenerate with one or more other states. In this case, the previous theorem (2.1) is not applicable. For instance, when $|\psi_1\rangle$ and $|\psi_2\rangle$ are degenerate, then all Fock states of the form $|N - k, k, 0, \dots, 0\rangle$, with $k = 0, \dots, N$, are degenerate, so the degenerate ground-state subspace of the noninteracting system, in this case, has dimension $N + 1$. In a more general scenario, where the first M_0 single-particle states, $|\psi_1\rangle, \dots, |\psi_{M_0}\rangle$, are degenerate, all the Fock states of the form $|n_1, \dots, n_{M_0}, 0, \dots, 0\rangle$ become degenerate and, as a result, the degeneracy of the ground state subspace is $\frac{(M_0+N-1)!}{(M_0-1)!N!}$. In this kind of systems, as the number of particles increases, so does the degeneracy of the ground state. The lowest-energy physics in this situation is explained, without interactions, by bosons populating only the first M_0 single-particle states, basically, and this effect would be more notorious in the case of increasing the number of particles.

In the following sections we explicitly consider practical situations, that we use for our calculations in the next Chapters. We will see that in some cases we are able to derive an analytic expression for the dimension of the truncated many-body Hilbert space.

2.5   Many-boson basis in a two-dimensional harmonic trap

In this section, we present the basis that is used in Chapter 3. The single-particle Hamiltonian for a particle of mass m in a two-dimensional isotropic harmonic trap of frequency ω is

$$\hat{H}_{\mathrm{sp}} = \frac{1}{2}\left(\hat{p}_x^2 + \hat{p}_y^2\right) + \frac{1}{2}\left(\hat{x}^2 + \hat{y}^2\right), \tag{2.22}$$

where we use harmonic oscillator units, i.e. energies in units of $\hbar\omega$, lengths in units of $\sqrt{\hbar/(m\omega)}$, and momenta in units of $\sqrt{\hbar m\omega}$. Their eigenstates are $|\psi_i\rangle = |n_x(i), n_y(i)\rangle$, where the index $i = 1, \dots, M$ runs through the pair of quantum numbers n_x and n_y, that take the values $0, 1, \dots$. The corresponding eigenenergies are $\epsilon_i = n_x(i) + n_y(i) + 1$. In the position representation, the wave functions associated to the states, $\psi_i(x, y)$, are written as

$$\psi_i(x, y) = N_{n_x} N_{n_y} H_{n_x}(x) H_{n_y}(y) e^{-\frac{x^2+y^2}{2}}, \tag{2.23}$$

with $H_n(x)$ the Hermite polynomials and the normalization constant

$$N_n = \left(\frac{1}{\sqrt{\pi} 2^n n!}\right)^{1/2}. \tag{2.24}$$

Thus, the creation and annihilation operators, $\hat{a}_i^\dagger$ and $\hat{a}_i$, create and destroy bosons in the previous states, $|n_x(i), n_y(i)\rangle$. The Hamiltonian of the noninteracting many-boson system is

$$\hat{H}_0 = \sum_{i=1}^{M} (n_x(i) + n_y(i) + 1)\, \hat{a}_i^\dagger \hat{a}_i, \tag{2.25}$$

Eigenstates	E	N_E	d_{N_E}
$\lvert N, 0, ..., 0 \rangle$	N	0	1
$\lvert N-1, 1, 0, ..., 0 \rangle$ $\lvert N-1, 0, 1, 0, ..., 0 \rangle$	N+1	1	2
$\lvert N-1, 0, 0, 1, 0, ..., 0 \rangle$ $\lvert N-1, 0, 0, 0, 1, 0, ..., 0 \rangle$ $\lvert N-1, 0, 0, 0, 0, 1, 0, ..., 0 \rangle$ $\lvert N-2, 2, 0, ..., 0 \rangle$ $\lvert N-2, 0, 2, 0, ..., 0 \rangle$ $\lvert N-2, 1, 1, 0, ..., 0 \rangle$	N+2	2	6
$\lvert N-1, 0, 0, 0, 0, 0, 1, 0, ..., 0 \rangle$ $\lvert N-1, 0, 0, 0, 0, 0, 0, 1, 0, ..., 0 \rangle$ $\lvert N-1, 0, 0, 0, 0, 0, 0, 0, 1, 0..., 0 \rangle$ $\lvert N-1, 0, 0, 0, 0, 0, 0, 0, 0, 1, 0, ..., 0 \rangle$ $\lvert N-2, 1, 0, 1, 0, ..., 0 \rangle$ $\lvert N-2, 0, 1, 1, 0, ..., 0 \rangle$ $\lvert N-2, 1, 0, 0, 1, 0, ..., 0 \rangle$ $\lvert N-2, 0, 1, 0, 1, 0, ..., 0 \rangle$ $\lvert N-2, 1, 0, 0, 0, 1, 0, ..., 0 \rangle$ $\lvert N-2, 0, 1, 0, 0, 1, 0, ..., 0 \rangle$ $\lvert N-3, 1, 2, 0, ..., 0 \rangle$ $\lvert N-3, 2, 1, 0, ..., 0 \rangle$ $\lvert N-3, 3, 0, ..., 0 \rangle$ $\lvert N-3, 0, 3, 0, ..., 0 \rangle$	N+3	3	14

Table 2.1: Eigenstates, energy, E, excitation energy number, N_E, and degeneracy, d_{N_E}, for the low-energy levels of a system of $N \geqslant 3$ noninteracting identical bosons trapped in a two-dimensional isotropic harmonic potential. The energies are in units of $\hbar\omega$.

so the energy of each Fock state is

$$E_{\lvert n_1, ..., n_M \rangle} = \sum_{i=1}^{M} (n_x(i) + n_y(i) + 1)\, n_i . \tag{2.26}$$

For this system, we are in the first case described above, where the Theorem 2.1 applies. The particular feature of this system is that the eigenenergies are equispaced at both single-particle and many-body levels. Moreover, the proof of the theorem is simpler than in the general case. That

allows us to directly relate the minimum number of bosons required to maximize the degeneracy of the Fock states manifolds. These manifolds are labeled with the excitation energy number $N_E = E - E_0$, with $E_0 = E_{|N,0,\ldots,0\rangle}$, and the maximum number of degenerate states, $d_{N_E}^{\max}$, is reached when $N \geqslant N_E$. We can rewrite the Theorem 2.1 in this particular case as follows:

Theorem 2.2. $d_{N_E} = d_{N_E}^{\max} \iff N \geqslant N_E$

Proof. From left to right, if we have reached $d_{N_E}^{\max}$, one of the degenerate states is the one with N_E bosons in the single-particle states with excitation energy, $E_{\mathrm{exc}}^{\mathrm{sp}} = E^{\mathrm{sp}} - E_0^{\mathrm{sp}} = 1$. Therefore, we have $N \geqslant N_E$ bosons. From right to left, if we have $N \geqslant N_E$ bosons, we have reached the maximum degeneracy because having less bosons would not allow us to have the previous discussed state, which is degenerate. Adding more bosons would not increase the number of degenerate states, since it is impossible to introduce new states with the same energy as the previous ones. This is due to the finite ways of decomposing N_E as a sum of positive integers, without considering the order, that is, the number of partitions $p(N_E)$ [105, 106]. $\square$

Therefore, the degeneracy of the first $N_E + 1$ energy levels is independent of the number of particles N for any $N \geqslant N_E$. In Table 2.1, we give the low-energy states with their corresponding energies, excitation energy numbers and degeneracies for a system of N bosons. In Table 2.2, we give $d_{N_E}^{\max}$ for the first values of N_E. Computing the maximum degeneracy is analogous to computing the number of partitions of the integer N_E where there are $n + 1$ different kinds of part n for $n = 1, 2, 3, \ldots$, [107] and we can obtain it from its generating function,

$$\frac{1}{\prod_{k=1}^{\infty}(1 - x^k)^{k+1}} = \sum_{N_E=0}^{\infty} d_{N_E}^{\max} x^{N_E}, \tag{2.27}$$

and also,

$$d_{N_E}^{\max} = \sum_{k=0}^{N_E} p(N_E - k) PL(k), \tag{2.28}$$

where $PL(k)$ are the planar partitions of k [108]. Notice that the number of partitions is a lower bound of the maximum degeneracy,

$$d_{N_E}^{\max} \geqslant p(N_E), \tag{2.29}$$

and the equality would hold for non-degenerate single-particle states, e.g. for the 1D case.

Finally, for the dimension of the truncated Hilbert space, $D_{MB}(N_E)$, if we want to include all the states up to the manifold $N_E^{\max}$, we can say that

$$D_{MB}(N_E^{\max}) \leqslant \sum_{N_E=0}^{N_E^{\max}} d_{N_E}^{\max}, \tag{2.30}$$

and the equality would hold when the number of bosons of the system accomplishes $N \geqslant N_E^{\max}$ (see Table 2.3). The number of single-particle modes required following the criterion (2.18), M, is

E	N_E	$p(N_E)$	$d_{N_E}^{\max}$
N	0	1	1
N+1	1	1	2
N+2	2	2	6
N+3	3	3	14
N+4	4	5	33
N+5	5	7	70
N+6	6	11	149

Table 2.2: Energy, E, excitation energy number, N_E, number of partitions of the excitation energy number, $p(N_E)$, and maximum degeneracy for the low-energy levels of a system of N noninteracting identical bosons in a two-dimensional isotropic harmonic potential, $d_{N_E}^{\max}$. The maximum degeneracy is equal to the degeneracy of the level N_E if and only if $N \geqslant N_E$.

obtained summing the single-particle modes involved up to the manifold $N_E^{\max}$, knowing that the single-particle degeneracy is $(k+1)$:

$$M = \sum_{k=0}^{N_E^{\max}} (k+1) = \frac{(N_E^{\max}+1)(N_E^{\max}+2)}{2}. \tag{2.31}$$

2.5.1   The spinless two-boson system

For the spinless two-boson system, that is considered in Chapters 3 and 4, the degeneracy of each energy manifold has an analytic expression (see Appendix A), that is

$$d_{N_E}^b = -\frac{1}{3}\left(\left\lfloor \frac{N_E}{2} \right\rfloor + 1\right)\left[4\left\lfloor \frac{N_E}{2} \right\rfloor^2 + (2 - 3N_E)\left\lfloor \frac{N_E}{2} \right\rfloor - 3(N_E+1)\right], \tag{2.32}$$

where $\lfloor N_E/2 \rfloor$ indicates the floor function of $N_E/2$. As a result, we can obtain an expression for the two-body truncated Hilbert space as

$$D_{2B}(N_E^{\max}) = \sum_{N_E=0}^{N_E^{\max}} d_{N_E}^b = \frac{1}{6}\left\{ 3(1+N_E^{\max})(2+N_E^{\max}) + \left\lfloor \frac{N_E^{\max}-1}{2} \right\rfloor \right.$$
$$\times \left(1 + \left\lfloor \frac{N_E^{\max}-1}{2} \right\rfloor\right)\left(2 + \left\lfloor \frac{N_E^{\max}-1}{2} \right\rfloor\right)\left(5 + \left\lfloor \frac{N_E^{\max}-1}{2} \right\rfloor\right) \tag{2.33}$$
$$\left. + \left\lfloor \frac{N_E^{\max}}{2} \right\rfloor\left(1 + \left\lfloor \frac{N_E^{\max}}{2} \right\rfloor\right)\left(3 + \left(5 + \left\lfloor \frac{N_E^{\max}}{2} \right\rfloor\right)\right) \right\}$$

$N_E^{\max}$	M	$D_{MB}(N_E^{\max})$
0	1	1
1	3	3
2	6	9
3	10	23
4	15	56
5	21	126
6	28	275

Table 2.3: Dimension of the many-body Hilbert space, $D_{MB}(N_E^{\max})$, depending on the truncation manifold labeled with $N_E^{\max}$, and the number of single-particle modes required, M, in a system of bosons with $N \geqslant N_E^{\max}$.

2.5.2 The two-boson system with two pseudospin components

In the case that we consider two possible pseudospin components, as in Chapter 6, the Hilbert space dimension of the two boson system is given by:

$$D_{2B}(N_E^{\max}) = \sum_{k=0}^{N_E^{\max}} \left(3d_{N_E}^b + d_{N_E}^f \right), \tag{2.34}$$

where $d_{N_E}^b$ and $d_{N_E}^f$ are the spatially symmetric and antisymmetric degenerate two-particle states in a two-dimensional harmonic trap (see Appendix A), and the factors 3 and 1 account for the triplet and singlet states of the spin part. The number of modes required in this case is

$$M = \sum_{k=0}^{N_E^{\max}} 2(k+1) = (N_E^{\max} + 1)(N_E^{\max} + 2), \tag{2.35}$$

with $E_{\max} = N_E^{\max} + 2$.

2.6 Many-boson basis in a one-dimensional hard-wall box

In Chapter 5, we study few-boson localization in one dimension. In this case, we construct the many-boson basis populating the single-particle eigenstates of the Hamiltonian,

$$\hat{H}_{\rm sp} = \frac{1}{2m}\hat{p}_x^2, \tag{2.36}$$

that has only a kinetic energy term and describes a particle of mass m in a one-dimensional box of length L with hard-wall boundary conditions centered at $x = 0$. The eigenstates of this Hamiltonian are the eigenstates of the momentum operator, $\hat{p}_x$. Due to the boundary conditions,

the linear momentum is quantized, as well as the energy levels of the system that are given below. Now, we write the energies in units of $\hbar^2/(m\ell^2)$ and the momentum in units of $\hbar/\ell$. Our unit length is ℓ, so, for instance, L is written in units of ℓ. Equivalently, we are working with the wave functions solution of the Schrödinger equation:

$$-\frac{1}{2}\frac{\partial^2 \psi_k}{\partial x^2} = \epsilon_k \psi_k \tag{2.37}$$

imposing the conditions that

$$\psi_k\left(-\frac{L}{2}\right) = \psi_k\left(\frac{L}{2}\right) = 0. \tag{2.38}$$

The eigenfunctions solution of Eq. (2.37) that satisfy Eq. (2.38) have the following form,

$$\psi_k(x) = \sqrt{\frac{2}{L}}\sin\left[\frac{k\pi}{L}\left(x+\frac{L}{2}\right)\right], \tag{2.39}$$

and they are an orthonormal basis in the box, i.e.,

$$\int_{-\frac{L}{2}}^{\frac{L}{2}} \psi_k^*(x)\psi_j(x)\,dx = \delta_{kj}. \tag{2.40}$$

Their eigenvalues, in the energy units $\hbar^2/(m\ell^2)$, are

$$\epsilon_k = \frac{k^2\pi^2}{2L^2} \quad,\quad k = 1,2,3,\,\dots. \tag{2.41}$$

In this case, the creation and annihilation operators, $\hat{a}_k^\dagger$ and $\hat{a}_k$, respectively, create and destroy bosons in the states of Eq. (2.39). The second-quantized Hamiltonian of the noninteracting many-boson system takes the form,

$$\hat{H}_0 = \sum_{k=1}^{M} \frac{k^2\pi^2}{2L^2}\,\hat{a}_k^\dagger \hat{a}_k\,, \tag{2.42}$$

and the energy of each Fock state, that we use to build the many-body basis following the energy criterion discussed in Sec. 2.3, is given by:

$$E_{|n_1,\dots,n_M\rangle} = \sum_{k=1}^{M} \frac{k^2\pi^2}{2L^2}n_k\,. \tag{2.43}$$

For this system, the theorem 2.1 also applies. However, the fact that the energy levels are not equispaced complicates the calculation of degeneracies and it is not possible to derive analytical expressions as we did in Sec. 2.5. Replacing the explicit form of the energies of the single-particle basis states given in Eq. (2.41) to Eq. (2.18), we find the relation between the number of single-particle modes, M, and the maximum excitation energy, $E_{\max}^{\text{exc}}$, of the truncation in the many-body basis:

$$\left(M^2-1\right)\frac{\pi^2}{2L^2} = E_{\max}^{\text{exc}}\,, \tag{2.44}$$

where, in this case, $E_{\max}^{\mathrm{exc}} = E_{\max} - N\pi^2/(2L^2)$ and, since M is a positive integer number, it can be obtained as:

$$M = \left\lfloor \sqrt{\frac{2L^2}{\pi^2}E_{\max} - N + 1} \right\rfloor \tag{2.45}$$

once $E_{\max}$ is fixed.

Chapter 3

FEW BOSONS INTERACTING IN A TWO-DIMENSIONAL HARMONIC TRAP

The system studied in this Chapter is formed by identical spinless bosons trapped inside a two-dimensional harmonic potential. Part of the contents of this Chapter were published in Ref. [13], where a different methodology for the diagonalization approach was used. Some of the properties of this system in the noninteracting case, for instance the degeneracy and its dependence on the number of particles, were presented in the previous Chapter, in Sec. 2.5, since they were a main ingredient in the construction of the many-body basis that we use in the present Chapter. Here, we concentrate on determining how the introduction of a two-body interaction potential affects the properties of the system when the strength and the range of the interaction vary.

We start, in Sec. 3.1, presenting the first-quantized form of the Hamiltonian, that can be written decoupling the center of mass from the relative part. After that, in Sec. 3.2, we discuss the convenience of using a two-body Gaussian potential chosen to model the atom-atom interaction. Next, we continue analyzing the effects of the interaction going from the noninteracting limit to the strongly-interacting one. We start, in Sec. 3.3, using first-order perturbation theory to describe the energy-level splittings for the N-boson system. Second, in Sec. 3.4, we propose two variational ansatzes for the ground state that capture the main effects induced by the interaction both in the weakly- and strongly-interacting cases. Then, in Secs. 3.5 and 3.6, we focus on the two-, three-, and four-boson systems and their low-energy spectra and eigenstates. In particular, in Sec. 3.7, we characterize the ground state of the system computing quantities as the energy contributions to the total energy, the condensed fraction, the spatial density profile and the two-body correlation function.

3.1 The first-quantized Hamiltonian: center-of-mass and relative parts

The numerical diagonalization method, presented in Chapter 2, is implemented using the second-quantization formalism. However, it is also useful to write the Hamiltonian of the system of N interacting bosons of mass m trapped by an isotropic harmonic potential in first-quantized form,

$$\mathcal{H} = \mathcal{H}_0 + \sum_{i<j}^{N} V(|\vec{x}_i - \vec{x}_j|), \tag{3.1}$$

with the noninteracting part,

$$\mathcal{H}_0 = \sum_{i=1}^{N} \left(-\frac{\hbar^2}{2m}\nabla_i^2 + \frac{1}{2}m\omega^2 \vec{x}_i^2 \right), \tag{3.2}$$

where ω is the trap frequency and $V(|\vec{x}_i - \vec{x}_j|)$ is a general two-body interaction potential. The reason is that, for any number of bosons N, we can split the Hamiltonian in two parts, $\mathcal{H} = \mathcal{H}_{\mathrm{cm}} + \mathcal{H}_{\mathrm{r}}$, using Jacobi coordinates,

$$\vec{R} \equiv \frac{1}{N}\sum_{i=1}^{N} \vec{x}_i,$$

$$\vec{r}_k \equiv \sqrt{\frac{2k}{k+1}}\left(\vec{x}_{k+1} - \frac{1}{k}\sum_{i=1}^{k} \vec{x}_i \right), \; k = 1, ..., N-1. \tag{3.3}$$

The center-of-mass and relative parts of the total Hamiltonian read, respectively,

$$\mathcal{H}_{\mathrm{cm}} = -\frac{\hbar^2}{2\mathcal{M}}\nabla_{\vec{R}}^2 + \frac{1}{2}\mathcal{M}\omega^2 \vec{R}^2, \tag{3.4}$$

$$\mathcal{H}_{\mathrm{r}} = \sum_{k=1}^{N-1} \left(-\frac{\hbar^2}{2\mu}\nabla_{\vec{r}_k}^2 + \frac{1}{2}\mu\omega^2 \vec{r}_k^2 \right) + \tilde{V}(\vec{r}_1, ..., \vec{r}_{N-1}), \tag{3.5}$$

with the definitions $\mathcal{M} \equiv Nm$ and $\mu \equiv m/2$. The interaction only appears in the relative part and takes the form

$$\tilde{V}(\vec{r}_1, ..., \vec{r}_{N-1}) \equiv \sum_{i<j}^{N} V\left(\left| \vec{x}_i(\vec{R}, \vec{r}_k, ..., \vec{r}_{N-1}) - \vec{x}_j(\vec{R}, \vec{r}_k, ..., \vec{r}_{N-1}) \right| \right). \tag{3.6}$$

Consequently, any change in the energy spectrum caused by the interaction is associated to $\mathcal{H}_{\mathrm{r}}$. The center of mass decouples and its Hamiltonian (3.4) corresponds to a two-dimensional harmonic oscillator. Therefore, the center-of-mass excitations present in the spectrum are expected to be separated by positive integer multiples of $\hbar\omega$. Moreover, the degeneracy of the center-of-mass part is $(n_{\mathrm{cm}} + 1)$, where each manifold is labeled with $n_{\mathrm{cm}} = 0, 1, ...$. These properties are used to check the convergence of our numerical results obtained by diagonalizing the truncated second-quantized Hamiltonian, which is not split in center-of-mass and relative parts.

Notice that, in the following sections, we will use harmonic-oscillator units, i.e. energies in units of $\hbar\omega$, lengths in units of $\sqrt{\hbar/(m\omega)}$, and momenta in units of $\sqrt{\hbar m\omega}$.

3.2   The interaction potential

In usual ultracold atomic gases experiments, the atom-atom interactions are well approximated by a contact potential [109]. An appropriate way of modeling this potential in a two-dimensional system is considering a regularized delta potential. In particular, for two particles in a harmonic trap, the problem of solving the Schrödinger equation with this model potential has an analytic solution [30]. However, for numerical calculations, it is more practical to use a smooth potential [110] with a finite range. This alternative approach facilitates the convergence of the results and, from a theoretical point of view, it allows to explore finite-range effects. In our case, we use a two-body Gaussian potential [31, 111–114],

$$V(|\vec{x}_i - \vec{x}_j|) = g \, \frac{1}{\pi s^2} e^{-\frac{|\vec{x}_i - \vec{x}_j|^2}{s^2}} , \tag{3.7}$$

where g and s characterize the strength and range of the interaction, respectively. g is written in units of $\hbar^2/m$ and s in units of $\sqrt{\hbar/(m\omega)}$, so $V(|\vec{x}_i - \vec{x}_j|)$ is in units of $\hbar\omega$, in accordance with the fact that we are using harmonic-oscillator units. Both parameters are considered to be tunable. For instance, g can be varied by means of a suitable Feshbach resonance [115]. The potential is normalized as:

$$\int_0^\infty V(r) \, 2\pi r \, dr = g. \tag{3.8}$$

In the limit of s going to zero, we recover a contact interaction with strength g [31]. As long as $g \geqslant 0$, the interaction between the particles is always purely repulsive. Using harmonic oscillator eigenstates, $\psi_i(x,y)$, as single-particle basis states for the second-quantized interaction term,

$$\hat{H}_{\text{int}} = \frac{g}{2} \sum_{i,j,k,l=1}^{M} V_{ijkl} \, \hat{a}_i^\dagger \hat{a}_j^\dagger \hat{a}_k \hat{a}_l , \tag{3.9}$$

the two-body matrix elements,

$$V_{ijkl} = \frac{1}{\pi s^2} \int_{-\infty}^\infty dx \, dy \, dx' \, dy' \, \psi_i^*(x,y)\psi_k(x,y)\psi_j^*(x',y')\psi_l(x',y') \, e^{-\frac{(x-x')^2+(y-y')^2}{s^2}} , \tag{3.10}$$

can be analytically calculated (see Appendix C). This is an advantage with respect to other ways of modeling the interaction, since we avoid the numerical evaluation of multidimensional integrals, which would introduce additional uncertainty.

3.3 First order perturbation theory for the N-boson system

In the weakly interacting limit, $g \ll 1$, the effects of the interaction in the lowest-energy levels of the N-boson system are well-approximated considering the interaction as a perturbation of the noninteracting system. We are able to treat explicitly the N-boson case because the degeneracy of the lowest-energy states is independent of the number of particles, as we explained in the previous Chapter. Using the analytic expressions for V_{ijkl}, that are given in Appendix C, we compute the energies of the first three energy manifolds, labeled with $N_E = 0, 1$, and 2 in Table 2.1, in first order perturbation theory.

For the unperturbed ground state of the system, $|N, 0, ..., 0\rangle$, the energy at first order of perturbation theory is given by

$$E_0 \simeq N + g \frac{N(N-1)}{2\pi (s^2 + 2)}. \tag{3.11}$$

The next energy level is two-fold degenerate and the interaction does not break this degeneracy. The two Fock states that form that subspace, $|N-1, 1, 0, ..., 0\rangle$ and $|N-1, 0, 1, ..., 0\rangle$, remain degenerated,

$$E_1 \simeq N + 1 + g \frac{N(N-1)}{2\pi (s^2 + 2)}, \tag{3.12}$$

where we observe that the term proportional to g is the same as in Eq. (3.11), because, with appropriate linear combinations of $|N-1, 1, 0, ..., 0\rangle$ and $|N-1, 0, 1, ..., 0\rangle$, one could describe the two possible center-of-mass excitations of the ground state.

The third energy manifold, formed by six states, splits in three sublevels. In the present case we need to use degenerate perturbation theory, i.e. we diagonalize the matrix of the interaction in this six-dimensional subspace. There are three states with energy

$$E_{2_1} \simeq N + 2 + g \frac{N(N-1)}{2\pi (s^2 + 2)}, \tag{3.13}$$

corresponding to center-of-mass excitations of the ground state. As we mentioned in Sec. 3.1 the perturbative correction affects only the relative motion, so the corrections included in E_0, E_1 and E_{2_1} are equal and the degeneracy is $(n_{cm} + 1)$, with $n_{cm} = 0, 1$, and 2, in each case, respectively.

Finally, there are two other states splitting from the third energy manifold in the noninteracting limit with

$$E_{2_2} \simeq N + 2 + g \frac{N \left(N(2 + s^2)^2 - s^2(8 + s^2) - 8 \right)}{2\pi (s^2 + 2)^3}, \tag{3.14}$$

and an additional single state whose energy is given by:

$$E_{2_3} \simeq N + 2 + g \frac{N \left(N(2 + s^2)^2 - s^2(8 + s^2) - 4 \right)}{2\pi (s^2 + 2)^3}. \tag{3.15}$$

The similarity in the excitation energy spectrum, $E - E_0$, for systems with different number of bosons for a small g can be understood using the previous expressions. For instance, in the
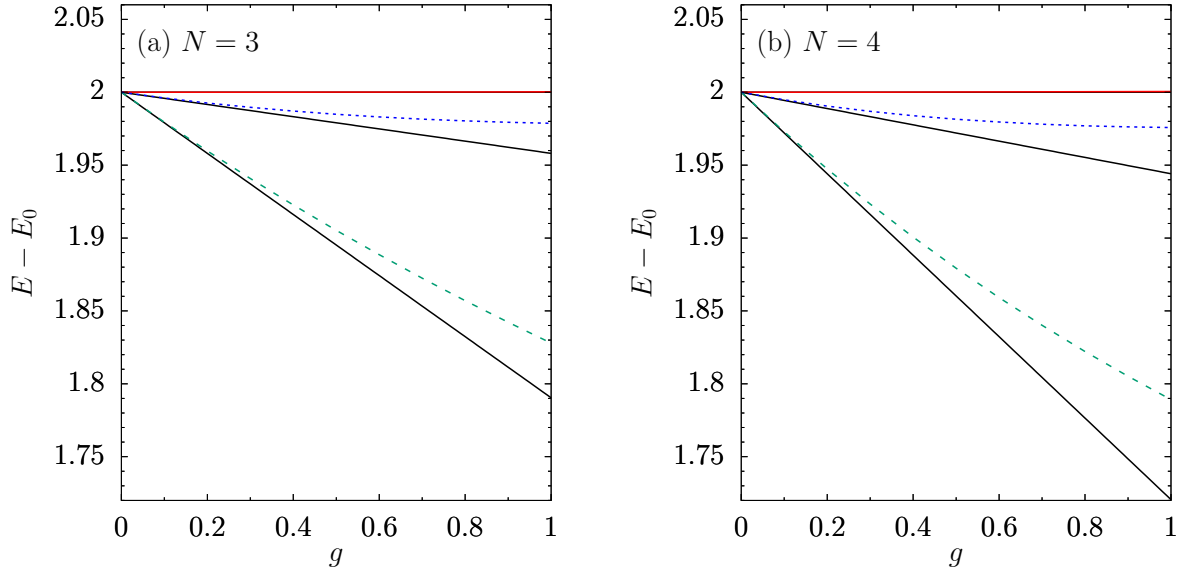
Figure 3.1: Splitting of the third energy level for (a) $N = 3$ and (b) $N = 4$ bosons depending on the interaction strength g. Solid red, dashed green and dotted blue lines: Numerically computed energy levels diagonalizing (see the caption of Fig. 3.4 for details). Solid black lines: Energy levels computed up to first order in perturbation theory corresponding to Eqs. (3.17), (3.18) and (3.19). Notice that red and black lines coincide.

case of $N = 3$ and $N = 4$ plotted in Fig. 3.1. The corresponding excitation energies are, in this approximation,

$$E_1 - E_0 = 1, \tag{3.16}$$

$$E_{2_1} - E_0 = 2, \tag{3.17}$$

$$E_{2_2} - E_0 = 2 - g\frac{2N\left(1+s^2\right)}{\pi\left(s^2+2\right)^3}, \tag{3.18}$$

$$E_{2_3} - E_0 = 2 - g\frac{2Ns^2}{\pi\left(s^2+2\right)^3}. \tag{3.19}$$

The presence of the factor N in the quantity $E_{2_2} - E_0$, in Eq. (3.18), explains why the slope of the green dashed lines is slightly bigger in absolute value for $N = 4$, panel (b), than for $N = 3$, panel (a), in Fig. 3.1. This effect would be notorious when comparing the spectrum for two very different numbers of particles. We also see that the second term in $E_{2_3} - E_0$ is proportional to N, but in that case, for small s, the second term becomes negligible. Therefore, the blue dotted lines are very close to the red solid lines in the spectra for $g \simeq 0$, as we have used $s = 0.5$. In the zero-range limit, this approximation gives $E_{2_3}(s \to 0) = E_{2_1}(s \to 0)$.

3.4   Variational calculations

In order to gain insight in the understanding of the ground-state properties of the system, we will compare our numerical results obtained by the exact diagonalization of the Hamiltonian in a truncated Hilbert space with the results provided by two variational ansatzes proposed below. Notice that both ansatzes provide upper bounds to the ground-state energy of the system.

3.4.1   Mean-field ansatz

The first variational ansatz that we propose is a mean-field wave function,

$$\Psi(\vec{x}_1, ..., \vec{x}_N) = \left(\frac{\alpha}{\pi}\right)^{\frac{N}{2}} \prod_{i=1}^{N} e^{-\frac{1}{2}\alpha \vec{x}_i^2}, \tag{3.20}$$

and we find the optimum α^* that minimizes the energy

$$E_0(\alpha) = \int_{-\infty}^{\infty} d\vec{x}_1 ... d\vec{x}_N \, \Psi^*(\vec{x}_1, ..., \vec{x}_N) \mathcal{H}\Psi(\vec{x}_1, ..., \vec{x}_N) = N\left(\frac{\alpha}{2} + \frac{1}{2\alpha}\right) + \frac{gN(N-1)\alpha}{2\pi\left(\alpha s^2 + 2\right)}. \tag{3.21}$$

This mean-field ansatz is expected to capture well the behavior of the ground state of the system for small values of g, as long as in the limit of $g \to 0$ we recover the noninteracting ground state of the system and $\alpha^* \to 1$. The parameter α characterizes the width of the Gaussian profile, that becomes wider when α gets smaller than 1. The variation of α allows the system of repulsively interacting atoms to be more separated in space. As we will see below, when the system develops strong beyond-mean-field correlations as g is increased this ansatz fails to describe the system.

3.4.2   Two-body-correlated variational many-body Jastrow-type ansatz

We also consider a two-body-correlated variational many-body ansatz of Jastrow type [116],

$$\Psi(\vec{x}_1, ..., \vec{x}_N) = \left(\frac{\alpha}{\pi}\right)^{\frac{N}{2}} \prod_{i=1}^{N} e^{-\frac{1}{2}\alpha \vec{x}_i^2} \prod_{j<i}^{N} \left(1 - ae^{-b|\vec{x}_i - \vec{x}_j|^2}\right), \tag{3.22}$$

where α, a and b are the variational parameters. Notice that this wave function is not normalized, so the energy to be minimized in this case is given by:

$$E_0(\alpha, a, b) = \frac{\int_{-\infty}^{\infty} d\vec{x}_1 ... d\vec{x}_N \, \Psi^*(\vec{x}_1, ..., \vec{x}_N) \mathcal{H}\Psi(\vec{x}_1, ..., \vec{x}_N)}{\int_{-\infty}^{\infty} d\vec{x}_1 ... d\vec{x}_N \, \Psi^*(\vec{x}_1, ..., \vec{x}_N)\Psi(\vec{x}_1, ..., \vec{x}_N)}. \tag{3.23}$$

The α parameter has the same role as in the mean-field ansatz of the previous section, that is recovered in the limit of $a \to 0$. In the opposite case, when $a = 1$, the wave function has zeros at $\vec{x}_i = \vec{x}_j$ for any pair i, j, with $i \neq j$, giving a zero probability of finding two particles at the same position. Consequently, a nonzero a value introduces correlations between the particles. The parameter b affects the two-body correlation length. In this case, we minimize the energy of this ansatz using standard Monte Carlo methods.

Here, we have considered a two-dimensional system. In the one-dimensional case, a variational ansatz that is able to describe a system of bosons with correlations is presented in Ref. [117].

3.5 Low-energy spectrum for the two-boson system

Below, we analyze the changes in the lowest-energy levels of the spectra of $N = 2$, 3, and 4 bosons, caused by interactions between the particles. The two-boson system presents particular properties and is treated separately, whereas we show that the systems with more particles have common features.

The two-boson system is a particular one because: i) the Jacobi coordinates, that allow to decouple the center-of-mass part from the relative part of the Hamiltonian, have a well-defined symmetry under the exchange of particles; ii) the states that have a relative wave function that is odd under the exchange of particles are unaffected by a contact interaction. These two features are used below to study the noninteracting system and, later on, in the understanding of the numerical results when the interaction is present.

3.5.1 The degeneracy for the noninteracting two-particle system

In the noninteracting case, for the two-boson system, we can write down the Hamiltonian splitting the center of mass and the relative motion. In polar coordinates,

$$\hat{H} = \hat{H}_{\text{cm}} + \hat{H}_{\text{r}} = \hat{n}_{\text{cm}} + \hat{n}_{\text{r}} + 2, \tag{3.24}$$

where $\hat{H}_{\text{cm}} = \hat{n}_{\text{cm}} + 1$ and $\hat{H}_{\text{r}} = \hat{n}_{\text{r}} + 1$. Therefore, we have a two-dimensional harmonic oscillator for each part of the Hamiltonian. The corresponding eigenstates can be labeled as $|n_{\text{cm}}, m_{\text{cm}}, n_{\text{r}}, m_{\text{r}}\rangle$, namely,

$$
\begin{aligned}
\hat{n}_{\text{cm}} |n_{\text{cm}}, m_{\text{cm}}, n_{\text{r}}, m_{\text{r}}\rangle &= n_{\text{cm}} |n_{\text{cm}}, m_{\text{cm}}, n_{\text{r}}, m_{\text{r}}\rangle, \\
\hat{n}_r |n_{\text{cm}}, m_{\text{cm}}, n_{\text{r}}, m_{\text{r}}\rangle &= n_{\text{r}} |n_{\text{cm}}, m_{\text{cm}}, n_{\text{r}}, m_{\text{r}}\rangle, \\
\hat{L}_{z,\text{cm}} |n_{\text{cm}}, m_{\text{cm}}, n_{\text{r}}, m_{\text{r}}\rangle &= m_{\text{cm}} |n_{\text{cm}}, m_{\text{cm}}, n_{\text{r}}, m_{\text{r}}\rangle, \\
\hat{L}_{z,\text{r}} |n_{\text{cm}}, m_{\text{cm}}, n_{\text{r}}, m_{\text{r}}\rangle &= m_{\text{r}} |n_{\text{cm}}, m_{\text{cm}}, n_{\text{r}}, m_{\text{r}}\rangle,
\end{aligned}
$$

$$\tag{3.25}$$

where $\hat{L}_{z,\text{cm}}$ and $\hat{L}_{z,\text{r}}$ are the third component of the center-of-mass orbital angular momentum and the relative orbital angular momentum, respectively, expressed in units of $\hbar$. However, those four quantum numbers have a restriction imposed by the symmetry of the wave function under the exchange of particles. The full wave function in polar coordinates for $\vec{R}$ and $\vec{r}$ reads

$$\chi_{n_{\text{cm}} m_{\text{cm}} n_{\text{r}} m_{\text{r}}} (R, r, \varphi_R, \varphi_r) = \chi_{n_{\text{cm}} m_{\text{cm}}} \left(\sqrt{2}, R, \varphi_R \right) \chi_{n_{\text{r}} m_{\text{r}}} \left(\frac{1}{\sqrt{2}}, r, \varphi_r \right), \tag{3.26}$$

with

$$\chi_{nm}\left(\alpha, r, \varphi\right) = N_{nm}\left(\alpha\right) e^{im\varphi} e^{-\frac{(\alpha r)^2}{2}} (\alpha r)^{|m|} L_{\frac{n-|m|}{2}}^{|m|}\left((\alpha r)^2\right). \tag{3.27}$$

The $L_n^k(x)$ are the associated Laguerre polynomials defined as

$$L_n^k(x) \equiv \sum_{m=0}^{n} (-1)^m \binom{n+k}{n-m} \frac{x^m}{m!} \tag{3.28}$$

and $N_{nm}\left(\alpha\right)$ is a normalization constant,

$$N_{nm}\left(\alpha\right) = \alpha \sqrt{\frac{\left(\frac{n-|m|}{2}\right)!}{\pi \left(\frac{n+|m|}{2}\right)!}}. \tag{3.29}$$

The wave function corresponding to the center of mass is symmetric under the exchange of particles, because R and φ_R remain unchanged upon exchanging particles 1 and 2, since $\vec{R} = \frac{1}{2}\left(\vec{x}_1 + \vec{x}_2\right)$. However, the relative wave function is symmetric or antisymmetric depending on the quantum number m_r. We have defined the relative coordinate as $\vec{r} = \vec{x}_1 - \vec{x}_2$, therefore, exchanging the particles is equivalent to a change in φ_r to $\varphi_r + \pi$ and, due to the form of the wave function, see Eq. (3.27), a factor $(-1)^{m_r}$ appears. For this reason, only the states with an even m_r can describe the two-boson system. This implies that n_r must also be an even number. To sum up (see Table 3.1), the four quantum numbers are

$$\begin{cases} n_{cm} = 0, 1, 2, 3, 4, \ldots \\ m_{cm} = -n_{cm}, -n_{cm} + 2, \ldots, n_{cm} \\ n_r = 0, 2, 4, 6, \ldots \\ m_r = -n_r, -n_r + 2, \ldots, n_r. \end{cases} \tag{3.30}$$

With the previous possible quantum numbers, we can determine the degeneracy for each energy level labeled with $N_E = E - E_0$. The degeneracy for a given value of N_E (see Appendix A) is

$$d_{N_E}^b = -\frac{1}{3}\left(\left\lfloor \frac{N_E}{2} \right\rfloor + 1\right)\left[4\left\lfloor \frac{N_E}{2} \right\rfloor^2 + (2 - 3N_E)\left\lfloor \frac{N_E}{2} \right\rfloor - 3(N_E + 1)\right], \tag{3.31}$$

where $\lfloor N_E/2 \rfloor$ indicates the floor function of $N_E/2$. The previous equation is valid for a system of two spinless bosons. However, for fermions and bosons with spin, the spatial antisymmetric states should also be considered. The degeneracy for those states (see Appendix A) is

$$d_{N_E}^f = -\frac{1}{3}\left(\left\lfloor \frac{N_E}{2} \right\rfloor + 1\right)\left[4\left\lfloor \frac{N_E}{2} \right\rfloor^2 + (8 - 3N_E)\left\lfloor \frac{N_E}{2} \right\rfloor - 6N_E\right]. \tag{3.32}$$

Notice that the total degeneracy is given by [118],

$$d_{N_E}^T = d_{N_E}^b + d_{N_E}^f = \frac{(N_E + 3)(N_E + 2)(N_E + 1)}{6}. \tag{3.33}$$

n_{cm}	n_{r}	m_{cm}	m_{r}	E	N_E	$d^b_{N_E}$	$d^U_{N_E}$
0	0	0	0	2	0	1	0
1	0	-1	0				
1	0	1	0	3	1	2	0
2	0	-2	0				
2	0	0	0				
2	0	2	0				
0	2	0	-2	4	2	6	2
0	2	0	0				
0	2	0	2				
3	0	-3	0				
3	0	-1	0				
3	0	1	0				
3	0	3	0				
1	2	-1	-2				
1	2	1	-2	5	3	10	4
1	2	-1	0				
1	2	1	0				
1	2	-1	2				
1	2	1	2				

Table 3.1: Quantum numbers, energy, excitation energy number, degeneracy, and number of states with $m_{\mathrm{r}} \neq 0$ for the low-energy levels of a system of two noninteracting identical bosons trapped in a two-dimensional isotropic harmonic potential. The energies are in units of $\hbar\omega$.

3.5.2 Unperturbed energy states

We are also interested in knowing how many states have $m_{\mathrm{r}} \neq 0$ for each energy level manifold, because these states are the ones that do not feel a zero-range interaction. For a finite but small range, these states are also expected to remain almost unperturbed for the considered range of interaction strengths. The number of states in each energy level such that their energy should not change significantly with a small Gaussian width (see Appendix A) is

$$d^U_{N_E} = \left(-\frac{4}{3} \left\lfloor \frac{N_E}{2} \right\rfloor + N_E + \frac{1}{3} \right) \left\lfloor \frac{N_E}{2} \right\rfloor \left(\left\lfloor \frac{N_E}{2} \right\rfloor + 1 \right) . \tag{3.34}$$

3.5.3   Two-boson energy spectrum

In Fig. 3.2, we show the low-energy spectrum for the system of two interacting identical bosons in the harmonic trap. In the figure, we compare results obtained with three different values of $s = 0.1$, 0.5 and 1. In all cases, the energy spectrum has a number of common features.

First, there are the states discussed above, that are called unperturbed states, which are essentially insensitive to the interaction. In the zero range limit, these are states with non-zero relative angular momentum, which do not feel the contact interaction [31]. With finite interactions with a small range, $s = 0.1$ and 0.5, they remain mostly flat for g up to 20. For $s = 1$, their energy increases slightly with g, deviating from the zero range prediction.

Second, the ground-state energy increases linearly with g for small values of g, according to first order perturbation theory, Eq. (3.11). However, the ground-state energy seems to saturate as g is increased. We show in all panels of Fig. 3.2 that with the variational Jastrow ansatz (3.22) we capture this phenomenon as the ground-state energy computed diagonalizing is very close to the variational one in the whole range of values of g displayed. This tendency is more apparent for smaller values of s. This fact is explained because the Gaussian potential extends to the whole space and building a zero of the wave function when two particles are at the same position is not sufficient to avoid the particles from interacting. Notice also that for a given value of g, the energy decreases when decreasing s.

Third, there are the energies coming from the relative part of the Hamiltonian with the center of mass at the ground state, i.e. $n_{cm} = 0$. The ground state is one of these states and there is one state of this type in each energy level manifold with an even N_E in the noninteracting limit.

Finally, the spectrum also contains center-of-mass excitations [30], which are easily recognized as constant energy shifts independent of g with respect to states with $n_{cm} = 0$.

For comparison, we depict also the approximate values of Ref. [31] in panel (a) of Fig. 3.2. As reported in Ref. [31], their approximate solution – which is not variational – starts to deviate from the numerical results, the ones obtained by diagonalizing, at values of $g \simeq 4$. In any case, the proposed approximation gives, however, a fairly good overall picture of the low-lying two-particle spectrum.
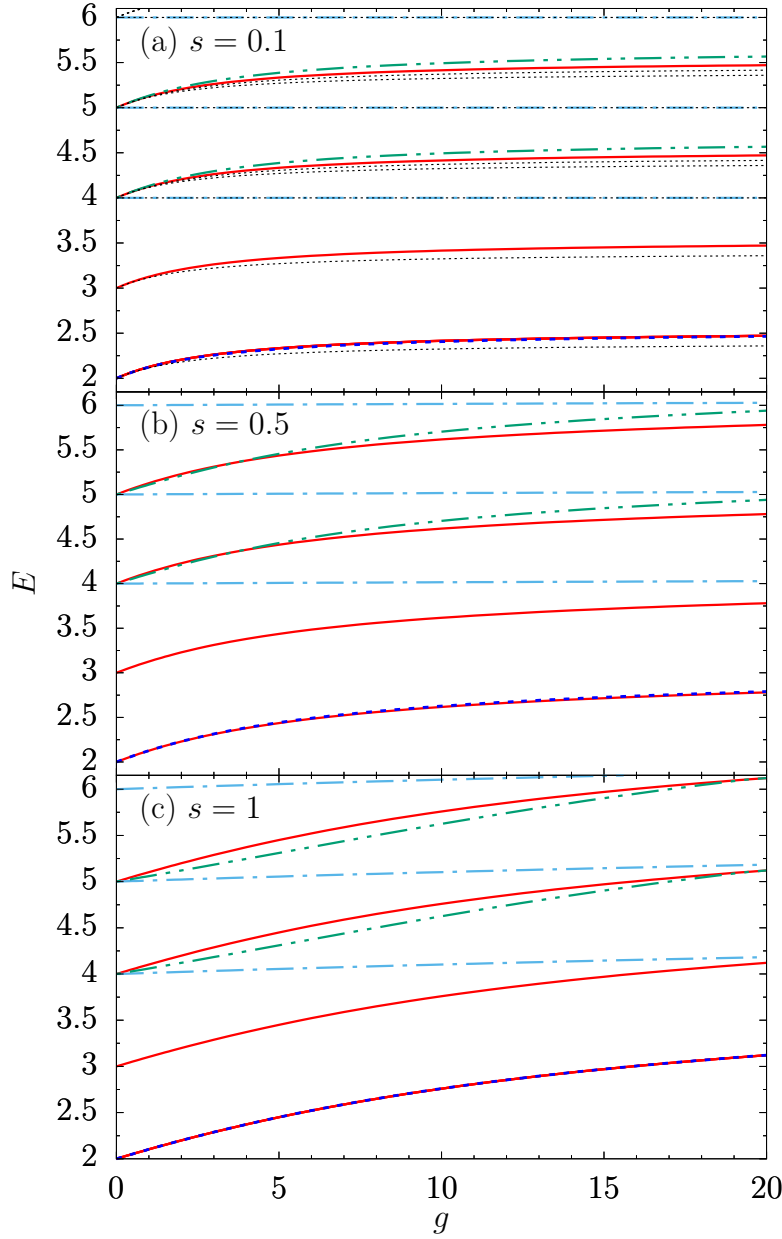
Figure 3.2: (a-c) Low-energy spectrum for $N = 2$ interacting bosons trapped in a two-dimensional isotropic harmonic potential depending on the interaction strength g for different values of the width s of the two-body Gaussian-shaped potential. Solid red lines: Energy of the ground state and its corresponding center-of-mass excitations. Long-dashed pointed cyan lines: Unperturbed states. Long-dashed double-pointed green lines: First relative excitation and its corresponding center-of-mass excitations. (a-c) Dashed blue lines: Energy of the ground state computed with the variational ansatz of Eq. (3.22). Dotted black lines: Analytic approximate energy levels using Eq. (17) of Ref. [31] shown only in panel (a). Numerical results with $M = 496$ single-particle states used corresponding to a Hilbert-space dimension $D_{2B} = 23256$ and a cutoff in energy $N_E^{\max} = 30$ (see Eq. 2.33).

3.5.4   The degeneracy for the interacting two-boson system

Considering the states with $m_r = 0$, which is fixed, we can label them with only three quantum numbers. Two are the ones corresponding to the center of mass, n_{cm} and m_{cm}, and the other is a new quantum number, ν_r, that labels the nondegenerate eigenstates of the relative part of the Hamiltonian. We can write those states as

$$\Psi_{n_{cm}m_{cm}\nu_r}^{m_r=0}(R,\varphi_R,r) = \chi_{n_{cm}m_{cm}}(\sqrt{2},R,\varphi_R)f_{\nu_r}(r), \tag{3.35}$$

where $\chi_{n_{cm}m_{cm}}(\sqrt{2},R,\varphi_R)$ is given in Eq. (3.27) and $f_{\nu_r}(r)$ is the relative wave function, that depends on g and s. The other states that are in the spectrum are the unperturbed ones (almost unaffected by the interaction). Their degeneracy is given by Eq. (3.34). The states of Eq. (3.35), for a given ν_r, are degenerate with degeneracy given by the two-dimensional harmonic oscillator of the center-of-mass part, i.e., their degeneracy is $n_{cm} + 1$. From each noninteracting energy level manifold with even N_E, a state with a new ν_r arises, and its center-of-mass excitations appear in higher energy levels with degeneracy $n_{cm} + 1$, too.

To sum up, the ground state is nondegenerate. The first excited state is two-degenerate and the two states are the two possible center-of-mass excitations of the ground state. The third noninteracting energy manifold (6 states with $E(g = 0) = 4$) splits in three: i) three center-of-mass excitations of the ground state, ii) two unperturbed states and, iii) the new relative state with quantum numbers $n_{cm} = 0$, $m_{cm} = 0$ and $\nu_r = 1$ with $E(g = 2) = 4.21$. We give the degeneracy and the quantum numbers of the low-energy states in Table 3.2.

n_{cm}	n_{r}	m_{cm}	m_{r}	ν_{r}	$E(g=0)$	$E(g=2)$	$d_{\mathrm{int}}(g=2)$
0	-	0	0	1	2	2.23	1
1	-	-1	0	1	3	3.23	
1	-	1	0	1	3	3.23	2
2	-	-2	0	1	4	4.23	
2	-	0	0	1	4	4.23	3
2	-	2	0	1	4	4.23	
0	-	0	0	2	4	4.21	1
0	2	0	-2	-	4	4.00	
0	2	0	2	-	4	4.00	2
3	-	-3	0	1	5	5.23	
3	-	-1	0	1	5	5.23	
3	-	1	0	1	5	5.23	4
3	-	3	0	1	5	5.23	
1	-	-1	0	2	5	5.21	
1	-	1	0	2	5	5.21	2
1	2	-1	-2	-	5	5.00	
1	2	1	-2	-	5	5.00	
1	2	-1	2	-	5	5.00	4
1	2	1	2	-	5	5.00	

Table 3.2: Quantum numbers, energy in the noninteracting limit, energy at $g=2$ and degeneracy, for the low-energy levels of a system of two interacting identical bosons trapped in a two-dimensional isotropic harmonic potential. The energies are in units of $\hbar\omega$ and the ones with $g=2$ correspond to a vertical cut in Fig. 3.2 panel (b), $s=0.5$.
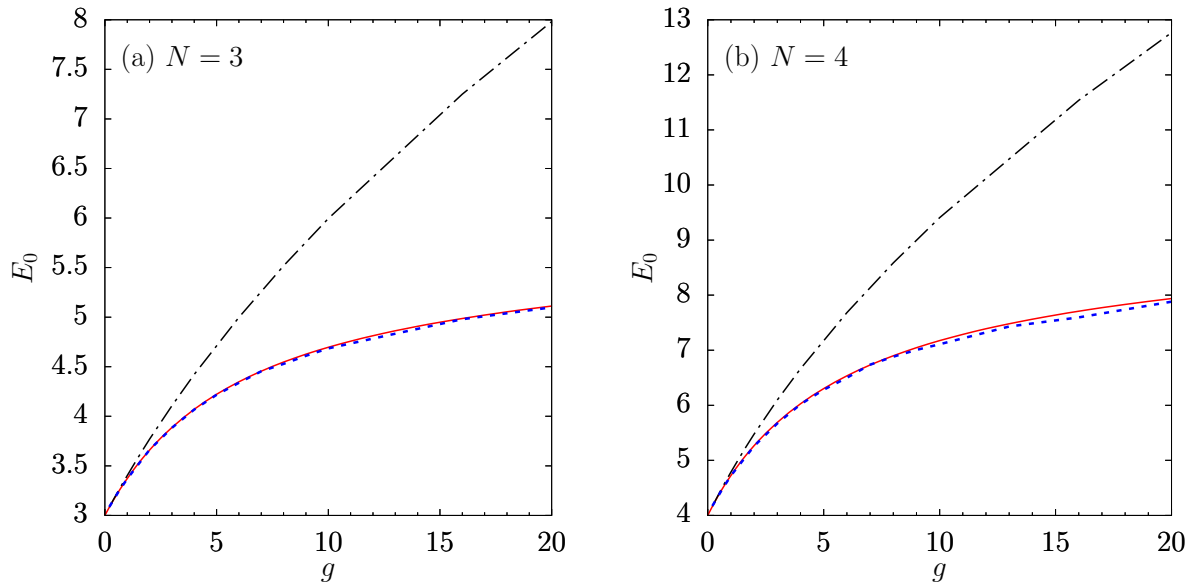
Figure 3.3: Ground-state energy for (a) N=3 and (b) N=4 interacting bosons trapped in a two-dimensional isotropic harmonic potential depending on the interaction strength g. Solid red line: Energy computed numerically, diagonalizing with $M = 210$ single-particle states that corresponds to a Hilbert-space dimension (a) $D_{3B} = 30846$ and (b) $D_{4B} = 107251$, and a cutoff in energy $N_E^{\max} = 19$, in both cases. Dashed blue line: Energy computed with the variational many-body Jastrow-type wave function of Eq. (3.22). Long-dashed dotted black line: Energy computed with a Gaussian mean-field variational ansatz, Eq. (3.20). The range of the interaction is $s = 0.5$.

3.6   Low-energy spectrum for the three- and four-boson systems

The ground-state energy of the systems with $N = 3$ and $N = 4$ bosons computed numerically, diagonalizing and with the two variational ansatzes, is represented in Fig. 3.3. As expected, the mean-field ansatz describes properly the changes in the ground-state energy for small values of g. However, for $g \approx 2$ we already observe substantial deviations, with the mean-field prediction overestimating the ground-state energy considerably. Nevertheless, the energies computed with the variational many-body ansatz of Jastrow type are very close to the exact-diagonalization ones. These results are a first indicator of the kind of physics produced by increasing the interaction strength, dominated by the presence of correlations, that is further analyzed in Sec. 3.7.

The low-energy spectrum for $N = 3$ and $N = 4$ at small values of g is fairly similar. This is not unexpected as the degenerate manifolds are the same irrespective of the number of particles, as it was explained in Chapter 2. The first excited state is a center-of-mass excitation, the Kohn mode (see [119] and references therein), as seen clearly in the excitation spectra shown in Fig. 3.4.

Even for g up to 20, the low-energy spectra for $N = 3$ and $N = 4$ are quite similar. The overall

picture is qualitatively the same for both cases, although for $N = 4$ there are extra levels crossing in the highest-energy part showed in Fig. 3.4. For instance, in Fig. 3.4 panel (b), there is a level (short-dashed brown line) that starts crossing the highest energy level depicted (solid red line) at $g \simeq 3$. This line in the spectrum comes from the fourth excited level in the noninteracting limit and is also expected to appear for systems with more particles, e.g. $N = 5$. It arises from the existence of a degenerate kind of states that are found only for $N \geqslant 4$, as it was explained in Chapter 2.

The degeneracy for the interacting three and four-boson system

For more than two particles, we do not find states unaffected by the interaction, the ones called unperturbed in the two-boson case. Moreover, the degeneracy of the eigenfunctions of the relative part of the Hamiltonian is not 1. Therefore, the states cannot be uniquely characterized by a single relative quantum number, ν_r, as before.

However, we can identify the states that correspond to center-of-mass excitations of lower energy states. In Fig. 3.4, in both panels, for example, for $g = 1$, we know the degeneracy of all the energy levels and we can identify them. Namely, the ground state is nondegenerate. As we have said before, the first excited state is a center-of-mass excitation, with degeneracy 2. The second excited state decomposes in three states corresponding to the next center-of-mass excitations of the ground state, two degenerate states corresponding to a relative excitation, and finally a different relative excitation. The third excited energy level in the noninteracting limit splits when g is increased in the next center-of-mass excitations of the states of the previous level, i.e., four center-of-mass excitations of the ground state, four center-of-mass excitations of the previous two-degenerate relative excited states, and two more degenerate states corresponding to two center-of-mass excitations of the single-degenerate relative energy level that appeared in the second excited state when g was increased. Moreover, there are two pairs of different relative excited states that split from the noninteracting third energy level. This behaviour is the same independently of N for g sufficiently small, for instance, for $N = 4$ up to $g = 3$, where we find the previous discussed crossing of levels.
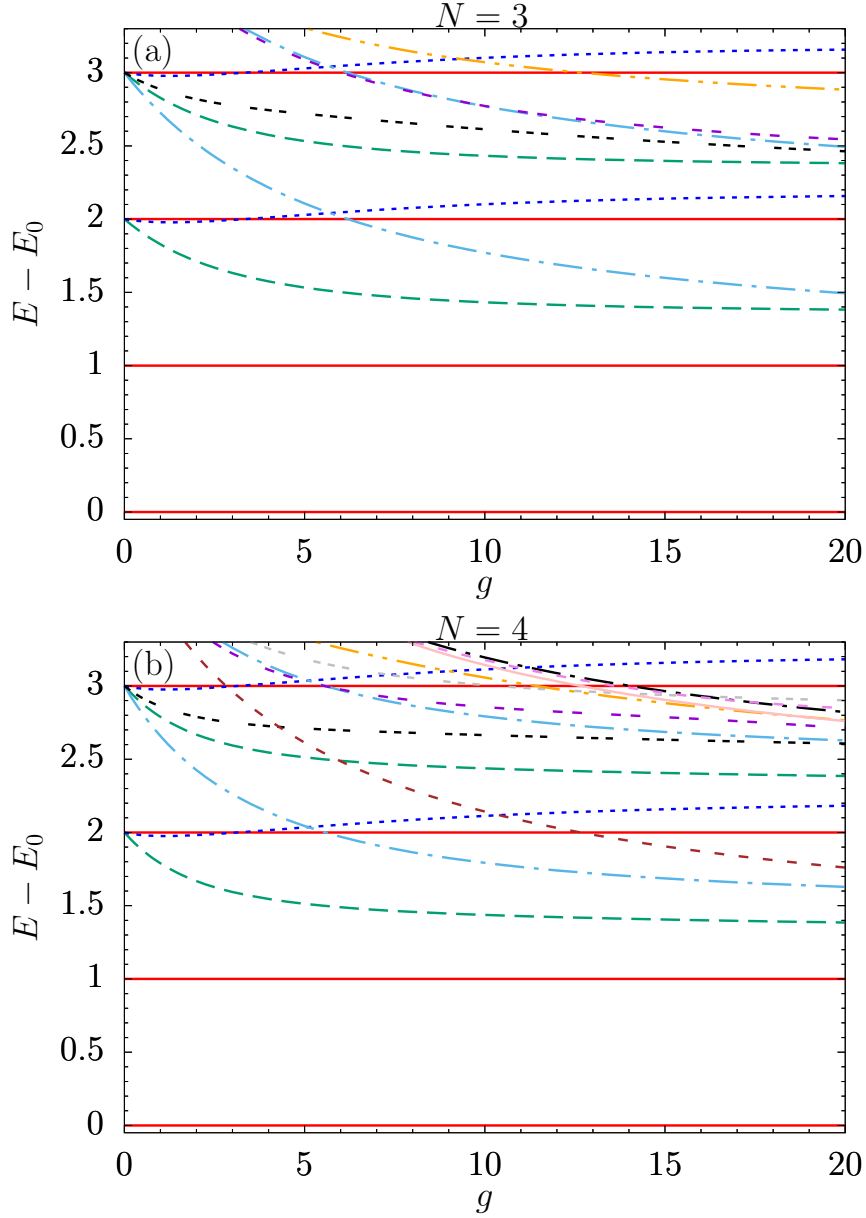
Figure 3.4: Low-energy spectrum for (a) $N = 3$ and (b) $N = 4$ interacting bosons trapped in a two-dimensional isotropic harmonic potential depending on the interaction strength g. Solid red lines: Energy of the ground state; dashed green lines: the first relative excitation; dotted blue lines: the second relative excitation; dashed-dotted cyan lines: the third relative excitation; triple-dotted black lines: the fourth relative excitation; and double-dotted black lines: the fifth relative excitation, and, respectively, their center-of-mass excitations in the same kind of line and color. The energies were computed numerically, diagonalizing with $M = 210$ single-particle states that corresponds to a Hilbert-space dimension (a) $D_{3B} = 30846$ and (b) $D_{4B} = 107251$, and a cutoff in energy $N_E^{\max} = 19$, in both cases. The range of the interaction is $s = 0.5$.

g	N=2			N=3			N=4		
	α	a	b	α	a	b	α	a	b
0	1	0	-	1	0	-	1	0	-
1	0.986	0.184	0.838	0.95	0.20	0.98	0.95	0.20	0.98
5	0.952	0.601	0.679	0.90	0.56	0.80	0.87	0.58	0.86
8	0.942	0.744	0.601	0.85	0.72	0.73	0.85	0.75	0.78
16	0.937	0.903	0.470	0.84	0.89	0.66	0.75	0.88	0.68

Table 3.3: Variational parameters obtained minimizing the energy of the correlated Jastrow-type wave function (3.22) depending on the interaction strength g for $s = 0.5$ and $N = 2$, 3, and 4 bosons.

3.7 Ground-state characterization for the few-boson system

As seen in Secs. 3.5 and 3.6, the ground-state energy of the system for $N = 2$, 3 and 4 seems to saturate as we increase the strength of the atom-atom interactions. This starts to occur for values g for which the mean-field variational ansatz starts to deviate from the exact results. This reminds one of a similar effect found in one-dimensional systems, where the ground state evolves from mean-field to Tonks-Girardeau gas as the interaction strength is increased [17]. In the Tonks-Girardeau limit, the atoms completely avoid the atom-atom contact interaction by building strong correlations which in 1D are easily understood from the Bose-Fermi mapping theorem [44]. In two-dimensions, no such mapping exist. However, we expect that the system should build suitable correlations to avoid interactions [47].

For the ground state, besides the exact diagonalization method, we have also made use of a correlated variational ansatz, Eq. (3.22), to clarify the discussion. The energies and properties associated to this variational ansatz are evaluated by means of Monte-Carlo methods (standard Metropolis algorithm). The physical meaning of the variational parameters is quite transparent. α directly affects the overall size of the cloud. The two-body Jastrow correlations are parameterized by a and b. Two limiting cases are illustrative. If the system is fully condensed we have $a = 0$, while $a = 1$ corresponds to building a zero of the wave function whenever two atoms are at the same position. b affects the two-body correlation length. Thus, we expect the following behavior: for values of $g \simeq 0$ we should have $a = 0$ (b is thus irrelevant) and α close to 1. For increasing g, α decreases to avoid the interaction by simply putting the atoms apart. As we increase g, two-body correlations build in, $a \neq 0$ and α should stop decreasing as the correlation is more efficient to separate the atoms. The numerical variational parameters obtained minimizing the energy are given in Table 3.3 for some values of g.

3.7.1 Energy contributions and virial theorem relation

The different energy terms that are present in the Hamiltonian in Eq. (3.1) are: the kinetic energy

$$\mathcal{K} = -\frac{1}{2} \sum_{i=1}^{N} \nabla_i^2 \,; \tag{3.36}$$

the harmonic potential

$$\mathcal{V}_{\text{ho}} = \frac{1}{2} \sum_{i=1}^{N} \vec{x}_i^2 \,; \tag{3.37}$$

and the interaction

$$\mathcal{V}_{\text{int}} = \frac{g}{\pi s^2} \sum_{i<j}^{N} e^{-\frac{|\vec{x}_i - \vec{x}_j|^2}{s^2}} \,. \tag{3.38}$$

Once we have the ground state, we compute each energy contribution as the expectation values $\langle \mathcal{K} \rangle$, $\langle \mathcal{V}_{\text{ho}} \rangle$, and $\langle \mathcal{V}_{\text{int}} \rangle$, respectively. The ground-state energy, E_0, is the total energy, so

$$E_0 = \langle \mathcal{K} \rangle + \langle \mathcal{V}_{\text{ho}} \rangle + \langle \mathcal{V}_{\text{int}} \rangle. \tag{3.39}$$

For any eigenstate of the Hamiltonian, and in particular for the ground state, the virial theorem establishes a relation between the energy contributions. In the present case, it translates into the following constrain:

$$2\langle \mathcal{V}_{\text{ho}} \rangle - 2\langle \mathcal{K} \rangle + \langle \mathcal{W} \rangle = 0 \,, \tag{3.40}$$

where the last term comes from the interaction part of the Hamiltonian (3.38), with

$$\mathcal{W} = -\frac{2g}{\pi s^4} \sum_{i<j}^{N} |\vec{x}_i - \vec{x}_j|^2 e^{-\frac{|\vec{x}_i - \vec{x}_j|^2}{s^2}} \,. \tag{3.41}$$

The previous energy terms and the left part of the virial relation, Eq. (3.40), are represented in Fig. 3.5 for the systems of $N = 2$, 3, and 4 bosons, depending on the interaction strength g.

First of all, since the bosons are in a two-dimensional system, at $g = 0$, the virial relation states that $\langle \mathcal{V}_{\text{ho}} \rangle = \langle \mathcal{K} \rangle$, so $E_0 = 2\langle \mathcal{V}_{\text{ho}} \rangle = 2\langle \mathcal{K} \rangle$. This is no longer true when $g \neq 0$. If the interaction strength is increased, we observe that the harmonic potential energy and the interaction energy increase. However, the kinetic energy slightly decreases. This effect is more notorious when we increase the number of particles of the system. At $g \approx 4$, the kinetic energy and the interaction energy exchange their roles. Increasing the value of g results in a decrease in the interaction energy and an increase in the kinetic one.

A second remarkable fact is that in the strongly-interacting limit, for large g, in Fig. 3.5, all energy terms tend to be constant, as well as the total energy shown in Fig. 3.2 panel (b) for $N = 2$, and panels (a) and (b) in Fig. 3.3 for $N = 3$ and 4, respectively. Regarding the virial relation, we observe that the ground state computed numerically fulfills it with good accuracy in the whole

range of g depicted; the left part of Eq. (3.40) remains very close to zero in all cases, within an error of less than 1% of E_0 for the two- and three-boson systems, and less than 2% of E_0 for the four-boson system. From a practical point of view, it provides a compelling nontrivial test for our numerics.
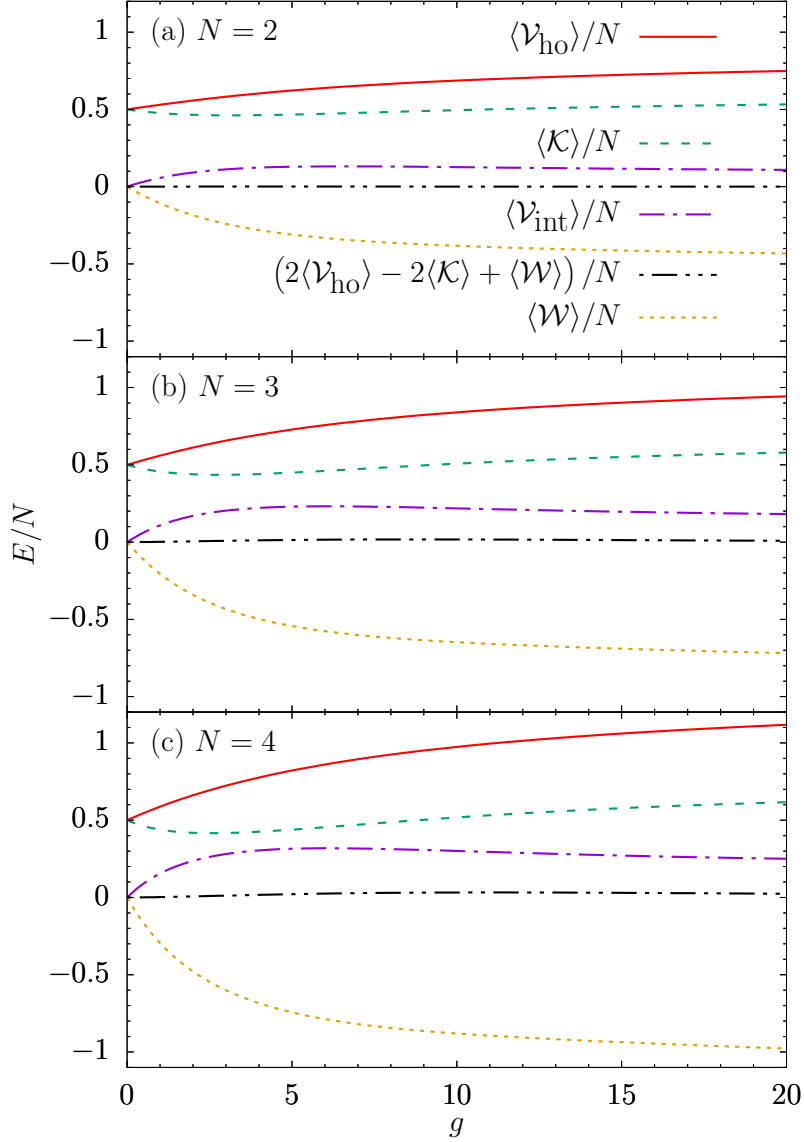

Figure 3.5: The energy terms contributing to the total energy and the ones involved in the virial theorem energy relation are depicted depending on the interaction strength g for (a) $N = 2$, (b) $N = 3$ and (c) $N = 4$ bosons. The energies were computed from the ground state obtained by diagonalizing with (a) $M = 496$ single-particle states corresponding to a Hilbert-space dimension $D_{2B} = 23256$ and a cutoff in energy $N_E^{\max} = 30$; in (b) and (c) $M = 210$ with (b) $D_{3B} = 30846$ and (c) $D_{4B} = 107251$, and a cutoff in energy $N_E^{\max} = 19$. The range of the interaction is $s = 0.5$.

3.7.2 Spatial density profiles

In this section, we show the effect of the interaction on the density of the system. The density is an observable quantity that is directly accessible in the current ultracold-atoms experiments with many particles. However, it is difficult to have access to it in few-particle systems because a high resolution is needed. To face this difficulty, new methods have been recently proposed [120–122].

In our calculations, we use the following definition of the density operator in first quantized form:

$$\hat{\rho}(\vec{x}) \equiv \frac{1}{N} \sum_{i=1}^{N} \delta(\vec{x} - \vec{x}_i). \tag{3.42}$$

We explicitly give the second-quantized form of this operator and we explain the details of the numerical computations in Appendix B. Additionally, we left there the demonstration that we only need to consider a dependence on the radial coordinate, $X = \sqrt{x^2 + y^2}$, for the ground state of the system. In short, the ground state is a state with zero total angular momentum, so it has radial symmetry setting the origin of coordinates at the center of the harmonic trap. Accordingly, the density function, which is the expectation value of the previous operator, is normalized to unity as

$$\int_0^\infty \rho(X) \, 2\pi X \, dX = 1. \tag{3.43}$$

In Fig. 3.6 we plot various density profiles computed with the ground state resulting from our diagonalization procedure. In panels (a), (b) and (c) we show results for $N = 2$, 3, and 4. In all cases, with the same value of $s = 0.5$. We compare the density profiles obtained for different values of g.

Irrespective of N we observe a number of common features. For $g = 0$, the system has a Gaussian density profile which, as g is increased, evolves into a profile with a flat region for $X \leq 1$ at $g \simeq 16$. As N is increased, the size of the inner plateau increases, thus tending towards an homogeneous density.

The quality of our variational approach is seen in Fig. 3.7. We compare density profiles obtained with the exact diagonalization procedure with those obtained variationally by means of Eq. (3.22). As seen in the figure, the variational correlated wave function provides a fairly accurate representation of the density profile for $N = 2$, 3, and 4. In particular, it captures well the appearance of the plateau.

Recently, the results presented in this section have been confirmed in Ref. [123], where they reproduce the density profiles by applying the methodology of path integral molecular dynamics.
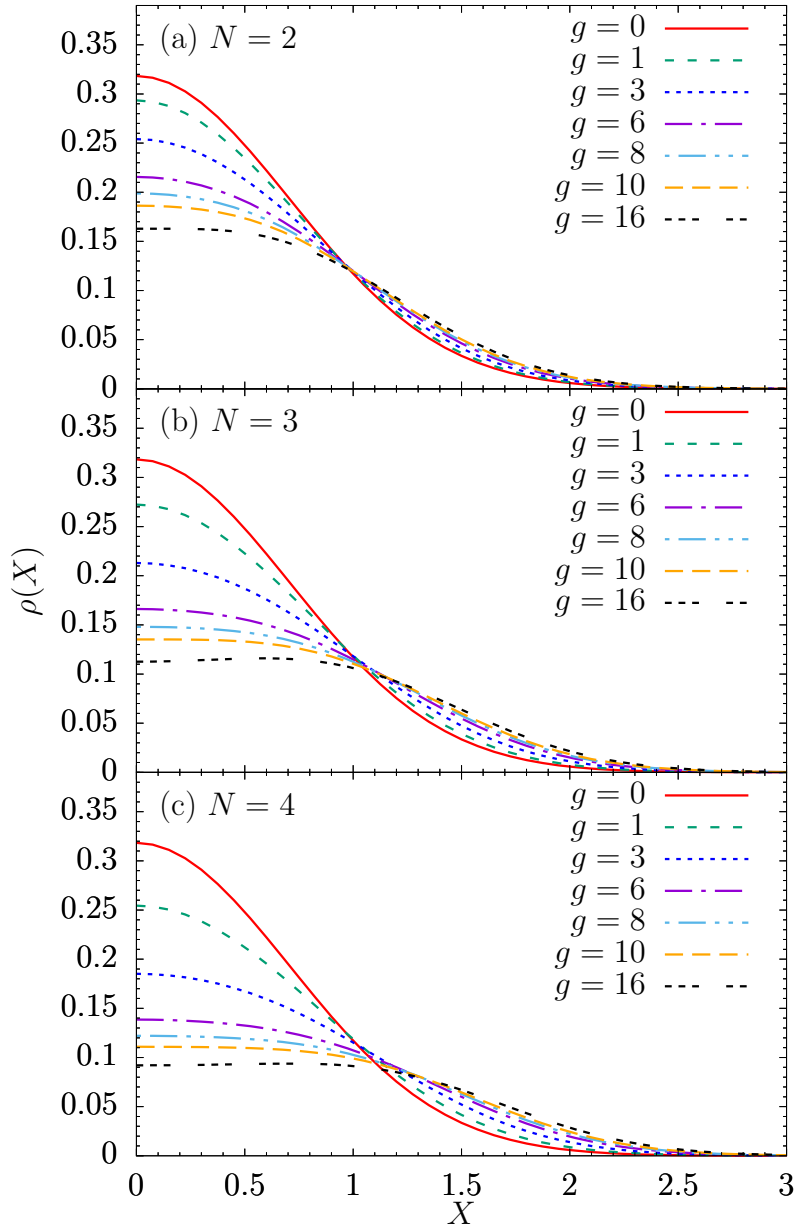
Figure 3.6: Density profile of the ground state for (a) $N = 2$, (b) $N = 3$ and (c) $N = 4$ interacting bosons trapped in a two-dimensional isotropic harmonic potential for different values of the interaction strength g for a fixed range $s = 0.5$. The profiles were computed numerically from the ground state obtained by diagonalizing with (a) $M = 496$ single-particle states corresponding to a Hilbert-space dimension $D_{2B} = 23256$ and a cutoff in energy $N_E^{\mathrm{max}} = 30$; (b) and (c) $M = 210$ single-particle states that corresponds to a Hilbert-space dimension (b) $D_{3B} = 30846$ and (c) $D_{4B} = 107251$, and a cutoff in energy $N_E^{\mathrm{max}} = 19$, in both cases.
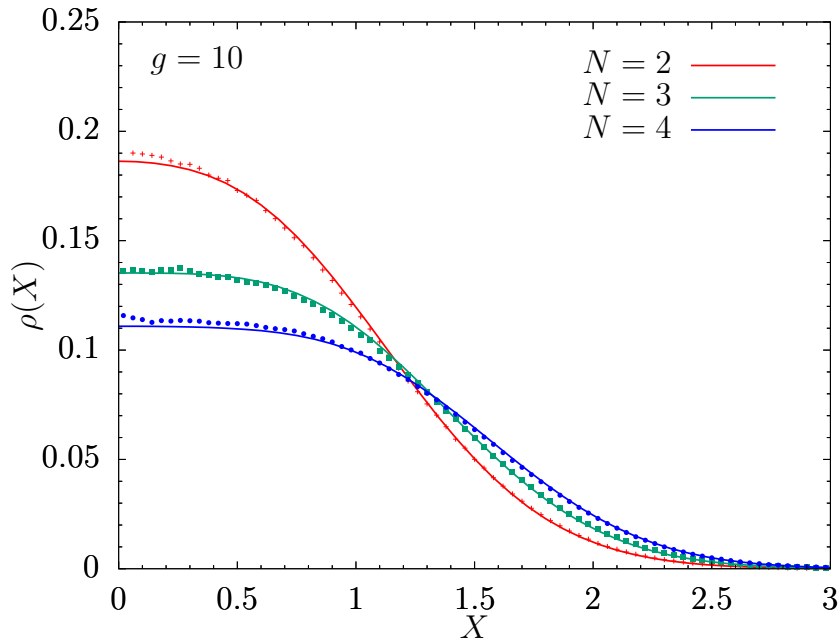
Figure 3.7: Density profile for $N = 2$, 3, and 4 interacting bosons trapped in a two-dimensional isotropic harmonic potential. Solid lines: Profiles computed with the ground state obtained diagonalizing (see details in the caption of Fig. 3.6). Crosses, squares and dots: Profiles obtained from the variational correlated Jastrow-type ansatz, Eq. (3.22). The range is $s = 0.5$. The variational parameters obtained are, for $N = 2$, $\alpha = 0.9$, $a = 0.8$ and $b = 0.7$, for $N = 3$, $\alpha = 0.85$, $a = 0.8$ and $b = 0.7$, and for $N = 4$, $\alpha = 0.85$, $a = 0.8$ and $b = 0.65$.

3.7.3 Condensed fraction

The effect of increasing the interaction among the atoms is manifold. The change in the density, seen before, is accompanied by a change in the correlations present in the system. Actually, it goes from a fully condensed state to a largely fragmented one as we increase the interaction. The condensed fraction is obtained from the one-body density matrix, defined as

$$\rho^{(1)}(\vec{x}, \vec{x}') = \int d\vec{x}_2 \ldots d\vec{x}_N \, \Psi^*(\vec{x}, \vec{x}_2, \ldots, \vec{x}_N) \Psi(\vec{x}', \vec{x}_2, \ldots, \vec{x}_N), \tag{3.44}$$

where $\Psi(\vec{x}_1, \vec{x}_2, \ldots, \vec{x}_N)$ is the ground state wave function. Since we truncate the Hilbert space using the first M single-particle eigenstates of the two-dimensional harmonic oscillator, the one-body density matrix is an $M \times M$ matrix in our case. The condensed fraction is the largest eigenvalue of this matrix and the most occupied single-particle state is the corresponding eigenstate. Both are obtained by diagonalizing $\rho^{(1)}(\vec{x}, \vec{x}')$ (see Appendix B).

In Fig. (3.8), we depict how the condensed fraction for $N = 2$, 3, and 4 decreases when increasing the interaction strength. For the same value of g, the fragmentation in the system is larger for
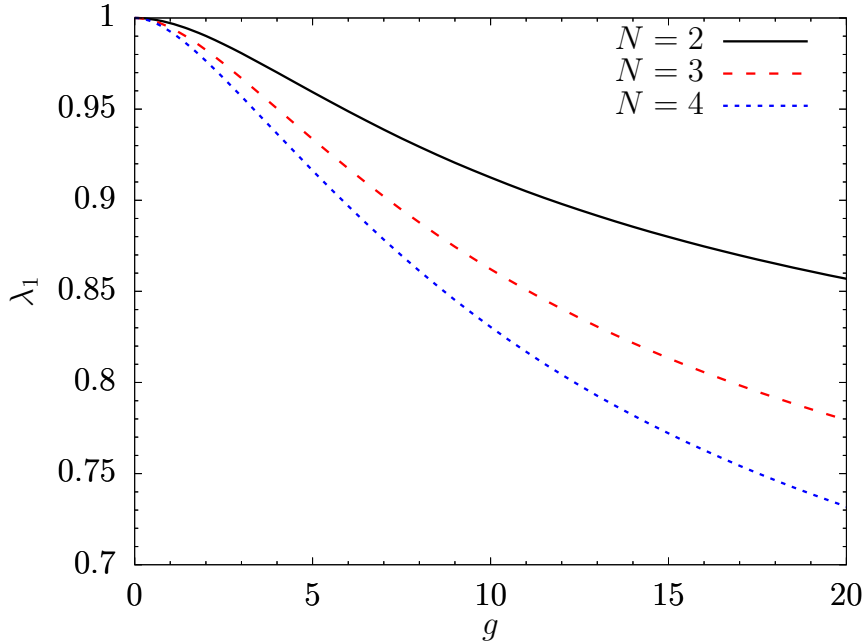
Figure 3.8: Condensed fractions of the ground state for (solid black line) $N = 2$, (dashed red line) $N = 3$ and (dotted blue line) $N = 4$ interacting bosons trapped in a two-dimensional isotropic harmonic potential depending on the interaction strength g for a fixed range $s = 0.5$. The number of modes that we have used is $M = 496$ for $N = 2$ and $M = 210$ for $N = 3$ and $N = 4$ (more details on the numerical calculation are given in previous Fig. 3.6). The rest of the eigenvalues of the one-body density matrix are much more smaller than the largest one.

larger number of particles.

The most populated eigenstate of the one-body density matrix (natural orbit), is found to have the approximate form, using the $|n_x, n_y\rangle$ basis,

$$|\phi_1\rangle \simeq C_0 |0,0\rangle + C_1 (|2,0\rangle + |0,2\rangle), \tag{3.45}$$

and its wave function reads

$$\phi_1(X) \simeq \frac{1}{\sqrt{\pi}} e^{-\frac{X^2}{2}} \left(C_0 - \sqrt{2}C_1 \left(1 - X^2\right)\right). \tag{3.46}$$

This natural orbit is a superposition of the two first single-particle states of the two-dimensional harmonic oscillator with zero angular momentum, $m = 0$, the state $|n = 0, m = 0\rangle$ and the state $|n = 2, m = 0\rangle$, thus the wave function has no angular dependence. For the noninteracting case, $C_0 = 1$ and $C_1 = 0$, since the particles condense in the ground state of the harmonic oscillator. When the interaction is increased, C_0 becomes smaller and C_1 starts to increase. In Fig. 3.9, we plot the wave function of Eq. (3.46) using the corresponding values of C_0 and C_1, given in Table 3.4, computed for $N = 2, 3, 4$ and different values of the interaction strength g.
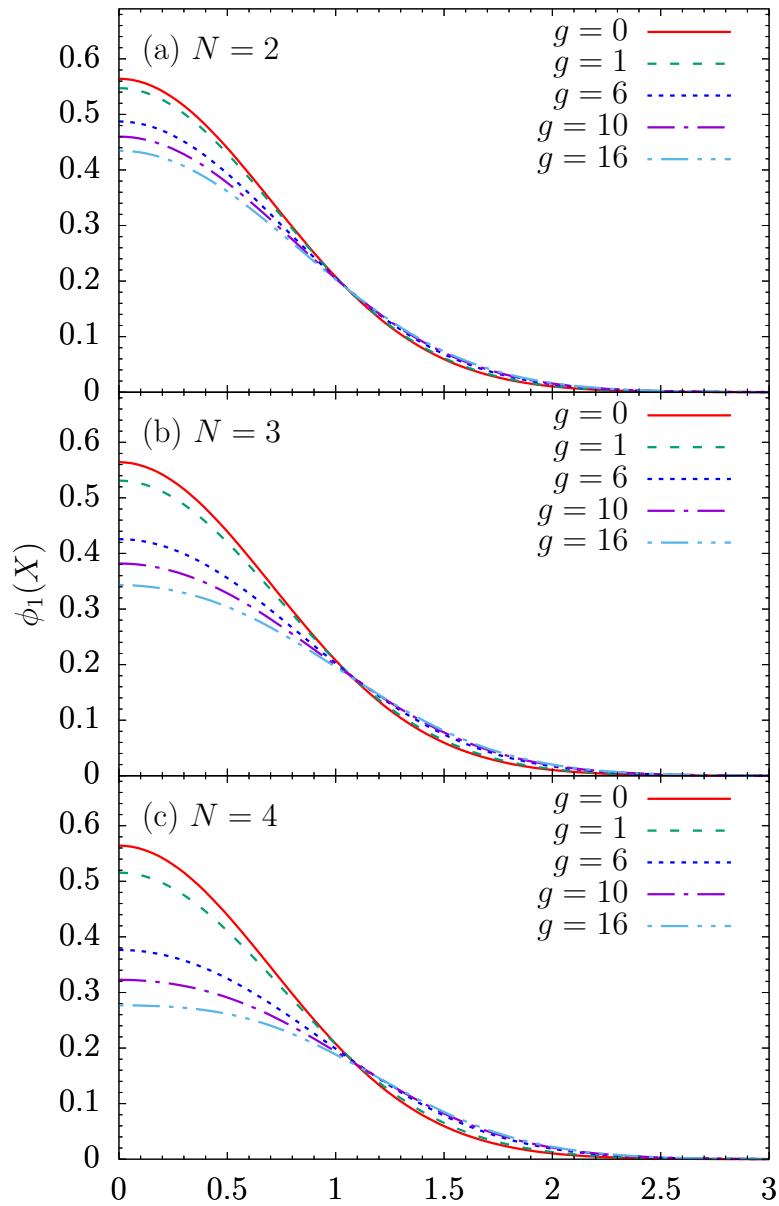
Figure 3.9: Single-particle eigenstate of the one-body density matrix in which the particles condense. We use the approximate form given in Eq. (3.46) and the values of C_0 and C_1 computed numerically diagonalizing the one-body density matrix, given in Table 3.4, for different values of g.

g	N=2		N=3		N=4	
	C_0	C_1	C_0	C_1	C_0	C_1
0	1	0	1	0	1	0
1	0.9995	0.0209	0.9983	0.0403	0.9965	0.0583
6	0.9915	0.0904	0.9752	0.1560	0.9571	0.2048
10	0.9851	0.1201	0.9592	0.1997	0.9325	0.2548
16	0.9778	0.1466	0.9424	0.2363	0.9077	0.2948

Table 3.4: Values of the coefficients C_0 and C_1 obtained numerically diagonalizing the one-body density matrix for $s = 0.5$ and $N = 2$, 3, and 4 bosons.

3.7.4 Two-body correlation functions

The advent of correlations beyond the mean-field ones should become more apparent when computing two-particle observables. In particular, we can evaluate the probability of finding two particles at given positions. To this end, we use the pair correlation operator, normalized to unity,

$$\hat{\eta}(\vec{x}, \vec{x}') \equiv \frac{1}{N(N-1)} \sum_{i=1}^{N} \sum_{j \neq i}^{N} \delta(\vec{x} - \vec{x}_i)\delta(\vec{x}' - \vec{x}_j). \tag{3.47}$$

The pair correlation function of a state, $\eta(\vec{x}, \vec{x}')$, the ground state in the present case, is computed as the expectation value of this operator. From the pair correlation and the density profile, we compute the probability of finding a particle at a distance $X \equiv \sqrt{x^2 + y^2}$ once we have found another particle at the origin, that is

$$P(X; 0) \equiv \frac{\eta(\vec{x}, \vec{0})}{\rho(\vec{0})}. \tag{3.48}$$

This probability density is normalized to unity, so that

$$\int_0^\infty P(X; 0)\, 2\pi X\, dX = 1. \tag{3.49}$$

As before, the details of the computations are given in Appendix B and here we concentrate on the analysis of the results.
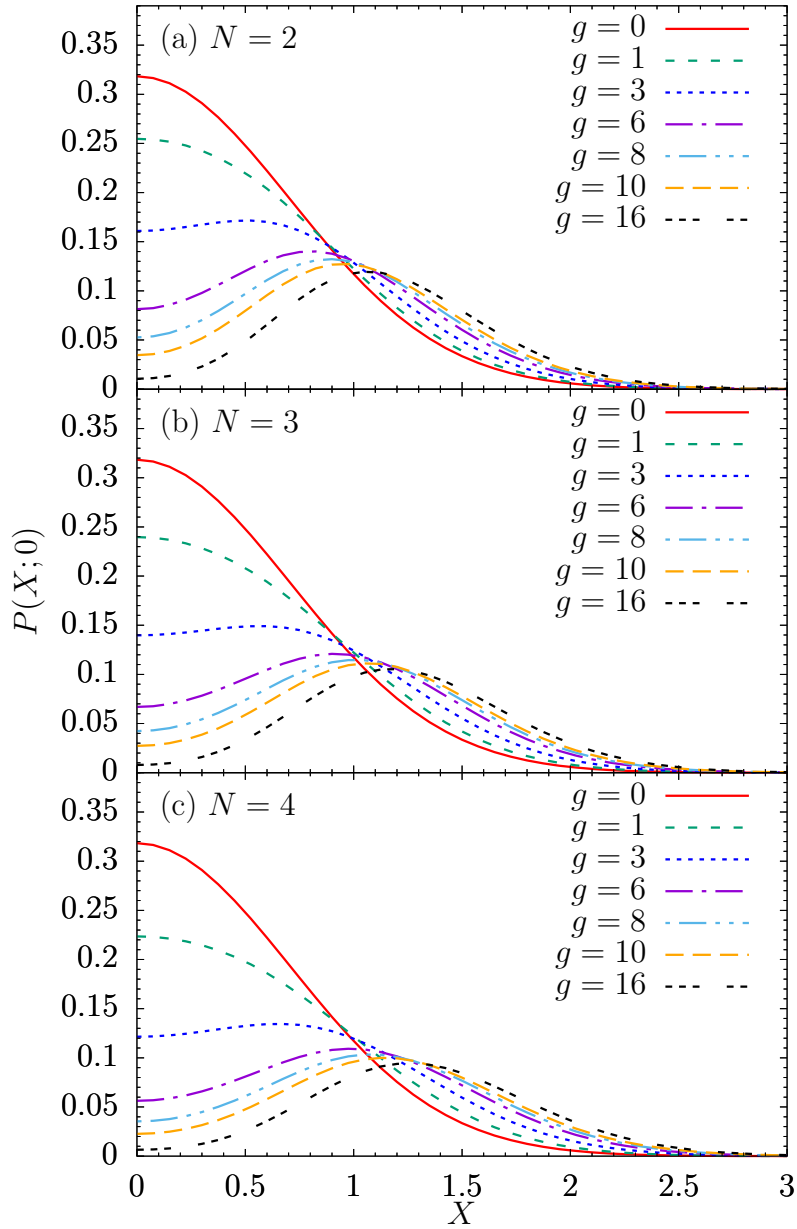
Figure 3.10: Probability density, $P(X;0)$, of finding a particle at position X once we have found one particle at the origin, $X = 0$, for (a) $N = 2$, (b) $N = 3$ and (c) $N = 4$ interacting bosons trapped in a two-dimensional isotropic harmonic potential for different values of the interaction strength g for a fixed range $s = 0.5$. The profiles were computed numerically from the ground state obtained by diagonalizing with (a) $M = 496$ single-particle states corresponding to a Hilbert-space dimension $D_{2B} = 23256$ and a cutoff in energy $N_E^{\max} = 30$; (b) and (c) $M = 210$ single-particle states that corresponds to a Hilbert-space dimension (b) $D_{3B} = 30846$ and (c) $D_{4B} = 107251$, and a cutoff in energy $N_E^{\max} = 19$, in both cases.

Without interactions, the pair correlation function is proportional to the density, since the probability density of finding a particle in a particular place is not correlated with the positions of the others. In Fig. 3.10, we show how $P(X;0)$ evolves with increasing the interaction for the systems with $N = 2$, 3, and 4 bosons. In all cases, the central peak gets lower when increasing the interaction, being fairly close to zero for $g \simeq 16$. This is in line with the fact that the atoms build correlations to avoid the interaction, e.g. as g is increased the probability of finding two atoms at the same location decreases. In between, next to the center of the trap, the function is uniform. When the interaction is strong there is a minimum at the position of the first atom, the probability density $P(X;0)$ develops a maximum corresponding to the preferred distance between particles. Increasing the number of bosons, this maximum shifts towards larger distances. The dependence of $P(X;0)$ on the particle number gives information about the many-body effects induced by the two-body correlations. Notice that, in the noninteracting case, $P(X;0)$ does not depend on the number of particles.

Chapter 4

FERMIONIC PROPERTIES OF TWO BOSONS IN A TWO-DIMENSIONAL HARMONIC TRAP

In this Chapter, we present a comparison between the ground state of the system of two repulsively interacting bosons and two noninteracting fermions trapped in a two-dimensional harmonic potential. The main motivation for extending the analysis of the previous Chapter comes from the fact that in one-dimensional systems there is the Bose-Fermi mapping theorem, that establishes a relation between strongly-interacting bosons and noninteracting fermions. Both systems have the same energy, and the ground-state wave function of the interacting bosonic system can be obtained by symmetrizing the noninteracting fermionic one by taking its absolute value [17].

However, the theorem does not apply in two or three dimensions. The particularity of one-dimensional systems is that if a particle is fixed at a point, the space becomes completely separated in two pieces. Then, another particle cannot move around the whole space without encountering the fixed one. Although this is not the case in two dimensions, our goal is to analyze whether strongly-interacting bosons can resemble noninteracting fermions. In the previous Chapter, we have showed that interacting bosons avoid feeling the repulsive interactions by building correlations in such a way that the probability of two particles being at the same position vanishes. Therefore, this mechanism, described by Girardeau in one dimension [17], remains as a possibility in the two-dimensional case.

As in the previous Chapter, we calculate numerically the ground state of the interacting two-boson system by diagonalizing the Hamiltonian in a suitable basis and also by using an appropriate

variational ansatz. Here, we concentrate on studying the dependence of the ground-state properties on the range and strength of the atom-atom interaction. In particular, we are interested in the strongly-interacting and the short-range limits.

First, in Sec. 4.1, we introduce the different analytic wave functions, which describe two noninteracting bosons, two noninteracting fermions, and the corresponding symmetrized wave function. Moreover, we present a modified version of the variational Jastrow ansatz given in the previous Chapter. Second, in Sec. 4.2, we analyze the behavior of the ground state energy and its different contributions. Finally, in Sec. 4.3, we show the interaction effects on the density profile and pair-correlation functions.

4.1   Analytic wave functions

The main issue is to understand how the two-boson system changes its structure as we increase the interaction strength or reduce its range. In particular, we want to discern whether any type of fermionization takes place in the strongly-interacting limit. To enlighten this discussion, we will compare the properties of the interacting two-boson system, with those of (i) the wave function of the ground state of two bosons in the noninteracting limit; (ii) the wave function of the ground state of two fermions in the noninteracting limit; and (iii) the wave function obtained by symmetrizing the previous one by taking its absolute value.

4.1.1   Noninteracting ground-state wave functions

The ground state of two noninteracting bosons described by the Hamiltonian in Eq. (3.2) is the nondegenerate state

$$\Psi_B(R, \varphi_R, r, \varphi_r) = \frac{1}{\pi} e^{-R^2 - \frac{r^2}{4}}. \tag{4.1}$$

This wave function has zero total angular momenta. Its energy is computed taking into account that it is an eigenfunction of the Hamiltonian in the noninteracting case, $\mathcal{H}_0 \Psi_B = 2\Psi_B$. The expectation value of the interaction term is given by:

$$\langle \mathcal{V}_{\text{int}} \rangle_{\Psi_B} = \frac{g}{\pi s^2} 4\pi^2 \int_0^\infty R \, dR \int_0^\infty r \, dr \, \frac{1}{\pi^2} e^{-2R^2 - \frac{r^2}{2}} e^{-\frac{r^2}{s^2}} = \frac{g}{\pi(2 + s^2)}. \tag{4.2}$$

Then, the expectation value of the Hamiltonian with this wave function reads

$$E_B = 2 + \frac{g}{\pi(s^2 + 2)}, \tag{4.3}$$

which is the first-order perturbation theory prediction for the energy of the system, given in Eq. (3.11). It is worth mentioning that the center-of-mass wave function contained in Eq. (4.1) is

the eigenfunction of $\mathcal{H}_{\text{cm}}$ with eigenvalue 1 energy unit.

For the noninteracting two-fermion system, the ground state would be two-fold degenerate, with a zero center-of-mass angular momentum, and the third component of the relative angular momentum equal to 1 or -1:

$$\Psi_F^{\pm}(R, \varphi_R, r, \varphi_r) = \frac{1}{\pi\sqrt{2}} e^{-R^2 - \frac{r^2}{4}} r e^{\pm i\varphi_r} . \tag{4.4}$$

These two states are also eigenstates of $\mathcal{H}_0$, $\mathcal{H}_0 \Psi_F^{\pm} = 3\Psi_F^{\pm}$. The expectation value of the interaction energy in this case is

$$\langle \mathcal{V}_{\text{int}} \rangle_{\Psi_F} = \frac{g}{\pi s^2} 4\pi^2 \int_0^{\infty} R\, dR \int_0^{\infty} r\, dr \frac{1}{2\pi^2} e^{-2R^2 - \frac{r^2}{2}} r^2 e^{-\frac{r^2}{s^2}} = g\frac{s^2}{\pi(2 + s^2)^2}, \tag{4.5}$$

and the total energy is

$$E_F = 3 + \frac{gs^2}{\pi(s^2 + 2)^2} . \tag{4.6}$$

Let us note that the contribution from the interaction vanishes, as it should, for the zero-range case, $s = 0$.

4.1.2 Bosonized two-fermion wave function

If we symmetrize the previous wave functions by taking their absolute value, $\Psi_{|F|} \equiv |\Psi_F^{\pm}|$, we obtain a bosonic wave function, as in 1D, that does not allow bosons to sit at the same position. Notice that both fermionic wave functions, (4.4), are transformed into the same symmetric one:

$$\Psi_{|F|}(R, \varphi_R, r, \varphi_r) = \frac{1}{\pi\sqrt{2}} r e^{-R^2 - \frac{r^2}{4}}, \tag{4.7}$$

which has no angular dependence. The main effect of this symmetrization is that $\Psi_{|F|}$ is not an eigenfunction of $\mathcal{H}_0$, and the expectation value of the energy in the noninteracting case is $\langle \mathcal{H}_0 \rangle_{\Psi_{|F|}} = 5/2$. The interaction energy is the same as before, $\langle \mathcal{V}_{\text{int}} \rangle_{\Psi_{|F|}} = (gs^2)/(\pi(s^2 + 2)^2)$, and the expectation value of the total energy in this case is

$$E_{|F|} = \frac{5}{2} + \frac{gs^2}{\pi(s^2 + 2)^2} . \tag{4.8}$$

The contribution of $\mathcal{H}_0$ to the previous expectation value, 5/2, is not equally distributed between kinetic and harmonic potential energies. Therefore, they do not fulfill the virial theorem. However, this is not a necessary condition, since $\Psi_{|F|}$ is not an eigenfunction of $\mathcal{H}_0$. The expectation values of the center-of-mass kinetic and harmonic potential energies are 1/2 each one, in agreement with the fact that the center-of-mass part of $\Psi_{|F|}$ is an eigenfunction of $\mathcal{H}_{\text{cm}}$ and, consequently, it verifies

the virial theorem, $\langle \mathcal{K}_{\mathrm{cm}} \rangle_{\Psi_{|F|}} = \langle \mathcal{V}_{\mathrm{cm}}^{\mathrm{ho}} \rangle_{\Psi_{|F|}} = 1/2$. To calculate the kinetic energy of $\mathcal{H}_{\mathrm{r}}$, we use the operator

$$\mathcal{K}_r = -\frac{\partial^2}{\partial r^2} - \frac{1}{r}\frac{\partial}{\partial r} - \frac{1}{r^2}\frac{\partial^2}{\partial \varphi_r^2}, \tag{4.9}$$

which results in

$$\mathcal{K}_r \Psi_{|F|} = -\frac{e^{-R^2 - \frac{r^2}{4}}(4 - 8r^2 + r^4)}{4\pi\sqrt{2}r}. \tag{4.10}$$

The expectation value then is

$$\langle \mathcal{K}_r \rangle_{\Psi_{|F|}} = -4\pi^2 \int_0^\infty r\,dr \int_0^\infty R\,dR\, \frac{e^{-2R^2 - \frac{r^2}{2}}(4 - 8r^2 + r^4)}{8\pi^2} = 1/2, \tag{4.11}$$

and, for the harmonic potential relative energy,

$$\langle \mathcal{V}_{\mathrm{ho}}^r \rangle_{\Psi_{|F|}} = 4\pi^2 \int_0^\infty r\,dr \int_0^\infty R\,dR\, \frac{1}{2\pi^2} e^{-2R^2 - \frac{r^2}{2}} r^2 \frac{r^2}{4} = 1. \tag{4.12}$$

Adding the relative and center-of-mass contributions, we have that the total kinetic energy is $\langle \mathcal{K} \rangle_{\Psi_{|F|}} = 1$, and the total harmonic potential energy is $\langle \mathcal{V}_{\mathrm{ho}} \rangle_{\Psi_{|F|}} = 3/2$.

Actually, $\Psi_{|F|}$ can be shown to be the best variational wave function, in the strongly-interacting limit, of the form

$$\Phi_a(R, \varphi_R, r, \varphi_r) = \frac{1}{\pi\sqrt{2^a \Gamma(1+a)}} e^{-R^2 - \frac{r^2}{4}} r^a. \tag{4.13}$$

For $a = 1$, we recover $\Psi_{|F|} = \Phi_1$. This set of functions are eigenfunctions of the center-of-mass Hamiltonian, $\mathcal{H}_{\mathrm{cm}}\Phi_a = 1\Phi_a$. The relative kinetic energy results to be independent of the parameter a, $\langle \mathcal{K}_r \rangle_{\Phi_a} = 1/2$, Therefore, $\langle \mathcal{K}_r \rangle_{\Psi_{|F|}} = \langle \mathcal{K}_r \rangle_{\Phi_a}$. On the other hand, the expectation value of the relative harmonic oscillator potential energy is $\langle \mathcal{V}_{\mathrm{ho}}^r \rangle_{\Phi_a} = (1+a)/2$ and the interaction energy reads

$$\langle \mathcal{V}_{\mathrm{int}} \rangle_{\Phi_a} = g\frac{\left(1 + \frac{2}{s^2}\right)^{-a}}{\pi(2 + s^2)}, \tag{4.14}$$

which tends to zero when $s \to 0$ only if $a \geqslant 1$. The total variational energy depending on a and s is

$$E(a, s)_{\Phi_a} = 1 + \frac{1}{2} + \frac{1+a}{2} + g\frac{\left(1 + \frac{2}{s^2}\right)^{-a}}{\pi(2 + s^2)}. \tag{4.15}$$

The energy minimum, in the short-range limit ($s \to 0$) and for strong interactions ($g \to \infty$), is reached when $a = 1$, which is precisely the case $\Psi_{|F|} = \Phi_1$ and the energy is $E(a = 1, s \to 0)_{\Phi_1} = E_{|F|}(s \to 0) = 5/2$.

4.1.3 Correlated variational two-boson Jastrow-type wave function

In the previous Chapter, we introduced in Eq. (3.22) a two-body-correlated variational many-body ansatz of Jastrow type for the N-boson system. With that wave function, we obtained very good upper bounds to the ground-state energies of the systems of $N = 2$, 3, and 4 bosons. An improved version of that ansatz for the two-boson system is the following one:

$$\Psi_J(R, \varphi_R, r, \varphi_r) = N_J \, e^{-R^2 - \beta \frac{r^2}{4}} \left(1 - ae^{-br^2} \right), \tag{4.16}$$

which has no angular dependence, being N_J a normalization constant given by:

$$N_J = \frac{1}{\sqrt{\frac{1}{\beta} + a \left(-\frac{2}{\beta + 2b} + \frac{a}{\beta + 4b} \right) \pi}}. \tag{4.17}$$

This last wave function is an eigenstate of the center-of-mass Hamiltonian, i.e. $\mathcal{H}_{\text{cm}} \Psi_J = \Psi_J$, and the kinetic and harmonic potential energies of this part are equal, $\langle \mathcal{K}_{\text{cm}} \rangle_{\Psi_J} = \langle \mathcal{V}_{\text{cm}}^{\text{ho}} \rangle_{\Psi_J} = 1/2$. The variational parameters only change the relative part of the wave function. The meaning of a and b is the same as in the previous Chapter. These two parameters characterize the two-body correlations in the wave function. β accounts for the interaction-induced mean-field effects in the relative motion by changing the width of the relative Gaussian profile.

The variational energy is written as:

$$E_J(\beta, a, b) = 1 + \langle \mathcal{V}_r^{\text{ho}} \rangle_{\Psi_J} + \langle \mathcal{K}_r \rangle_{\Psi_J} + \langle \mathcal{V}_{\text{int}} \rangle_{\Psi_J} \tag{4.18}$$

where the first term is the center-of-mass energy. The relative harmonic potential and relative kinetic energies are, respectively,

$$\langle \mathcal{V}_r^{\text{ho}} \rangle_{\Psi_J} = N_J^2 \pi^2 \left[\frac{1}{2\beta^2} + \frac{a^2}{2(\beta + 4b)^2} - \frac{a}{(\beta + 2b)^2} \right], \tag{4.19}$$

and

$$\langle \mathcal{K}_r \rangle_{\Psi_J} = N_J^2 \pi^2 \left[\frac{(a-1)^2(\beta^2 + 4\beta b) + 4(a^2 + 1)b^2}{2(\beta + 2b)^2} \right]; \tag{4.20}$$

while the interaction energy reads:

$$\langle \mathcal{V}_{\text{int}} \rangle_{\Psi_J} = N_J^2 g \pi \left[\frac{1}{2 + \beta s^2} - \frac{2a}{2 + (\beta + 2b)s^2} + \frac{a^2}{2 + (\beta + 4b)s^2} \right]. \tag{4.21}$$

The minimization of E_J is performed numerically with *Mathematica*, for a given s and g. The resulting optimal parameters, β^*, a^*, and b^*, are used to calculate the remaining quantities.

4.2   Ground-state energy analysis

4.2.1   Dependence on the interaction strength for a short-range interaction

In this section we investigate the effects of increasing the interaction strength, g, for a fixed range, $s = 0.01$, in the ground-state energy of the two-boson system. To this end, first, we compute the energy contributions to the ground-state energy, and, afterwards, we discuss the limiting cases using the analytical wave functions introduced previously. In particular, we are interested in the case where the range of the interaction is small compared with the harmonic oscillator length. On the one hand, it is representative of the situation in which the diagonalization method is no longer competitive because it requires a very large basis. On the other hand, this is the situation in which we can test if $\Psi_{|F|}$, that has the appropriate form to avoid a contact interaction, gives a good upper bound to the ground-state energy.

In Fig. 4.1, we present the ground-state energies provided by the diagonalization of the Hamiltonian matrix and by the minimization of the expectation value of $\mathcal{H}$ with the Jastrow-type wave
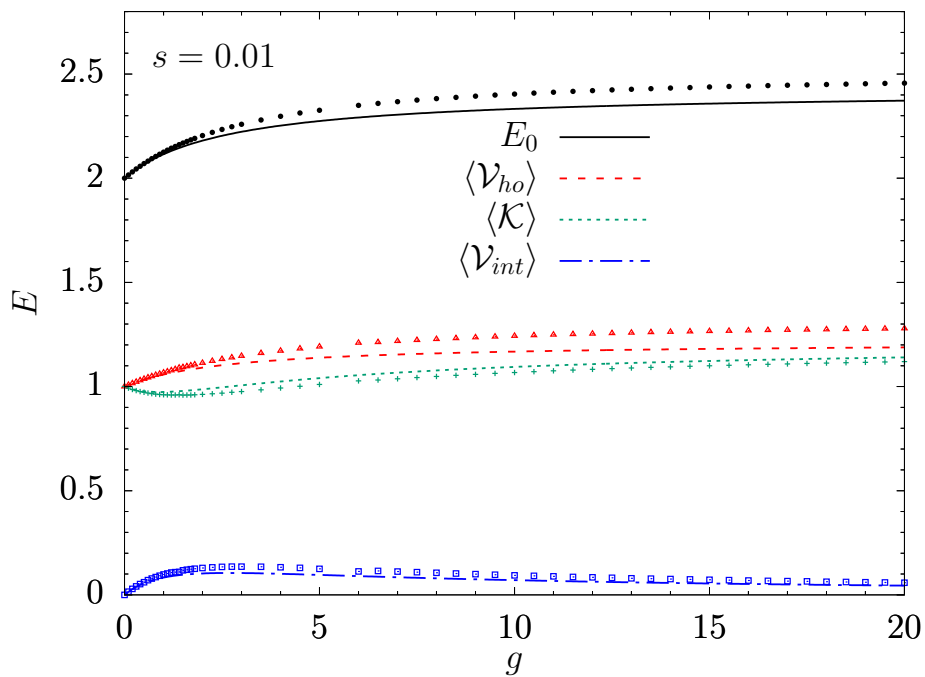

Figure 4.1: Ground state energy of two interacting bosons in a two-dimensional harmonic trap, E_0, depending on the interaction strength, g, for a fixed and small interaction range, $s = 0.01$. We present the harmonic potential, $\langle \mathcal{V}_{\mathrm{ho}} \rangle$, the kinetic, $\langle \mathcal{K} \rangle$, and the interaction, $\langle \mathcal{V}_{\mathrm{int}} \rangle$, energies. Symbols: Energies computed by numerical diagonalization of the Hamiltonian matrix. Lines: Energies computed with the variational ansatz Ψ_J given in Eq. (4.16).
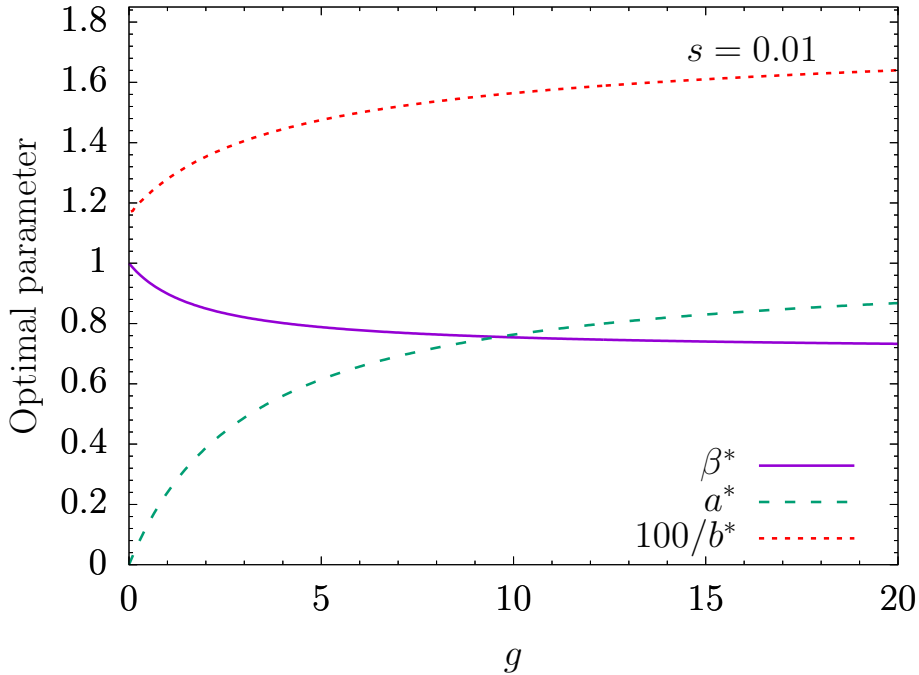
Figure 4.2: Variational parameters that minimize the energy E_J for a fixed range, $s = 0.01$, as a function of g.

function in Eq. (4.16). In the limit of $g = 0$, this function reduces to the wave function in Eq. (4.1). Then, the total energy is 2, arising from two equal contributions from the kinetic and potential energy. The most relevant contribution to the energy increase comes from the harmonic potential part. The kinetic energy remains close to 1 for $g < 1$ and then its value increases smoothly. Therefore, we can say that, at the beginning, the two particles avoid feeling the interaction mostly by separating one from the other. This reflects in an increase of the harmonic potential energy because they are further away from the center of the trap.

For small g values, the interaction part of the energy increases linearly with g, reaches a maximum at $g \approx 1$ and afterwards, decreases slowly. Finally, it remains mostly constant, getting close to zero for larger values of g. Since the interaction term in the Hamiltonian is proportional to g, this behavior reflects that the particles avoid feeling the interaction by building quantum correlations in the wave function of the ground state.

In the present situation, the diagonalization of the Hamiltonian and the minimization of the energy of Ψ_J, given in Eq. (4.18), disagree when g is large. We have to remark that both methods give an upper bound to the exact ground-state energy, since both are variational. The comparison is depicted in Fig. 4.1. Although we have used a Hilbert space of dimension $D_{2B} = 23256$, corresponding to $M = 496$ single-particle modes, this is not sufficient to obtain well-converged results

for $g > 2$. The Jastrow wave function, Ψ_J, provides a better upper bound to the ground-state energy. Most of the discrepancy between the two estimations comes from the fact that the harmonic potential energy obtained by diagonalizing is overestimated. Notice that, the kinetic and the interaction energies computed with both methods are fairly similar.

One advantage of describing the ground state with Ψ_J is that the variational parameters have a clean physical interpretation. The optimal values, that minimize the energy E_J, are plotted in Fig. 4.2. In accordance with the previous arguments, at small values of g, β^* is decreasing in order to allow the atoms to be further apart, whereas a^* is close to 0. The presence of correlations is signaled by the increasing value of a^* when g is increased, that goes from 0 in the noninteracting case and approaches 1 at $g = 20$. The fact that the range is small is reflected in a large value of b^*. This parameter is inversely related to the two-body correlation length, so $1/b^*$ is proportional to s in a first-order approximation. Consequently, in this case, the correlations between the two particles are decaying very rapidly as a function of the distance between them.

The comparison with the other analytical wave functions is done considering E_0 given by the
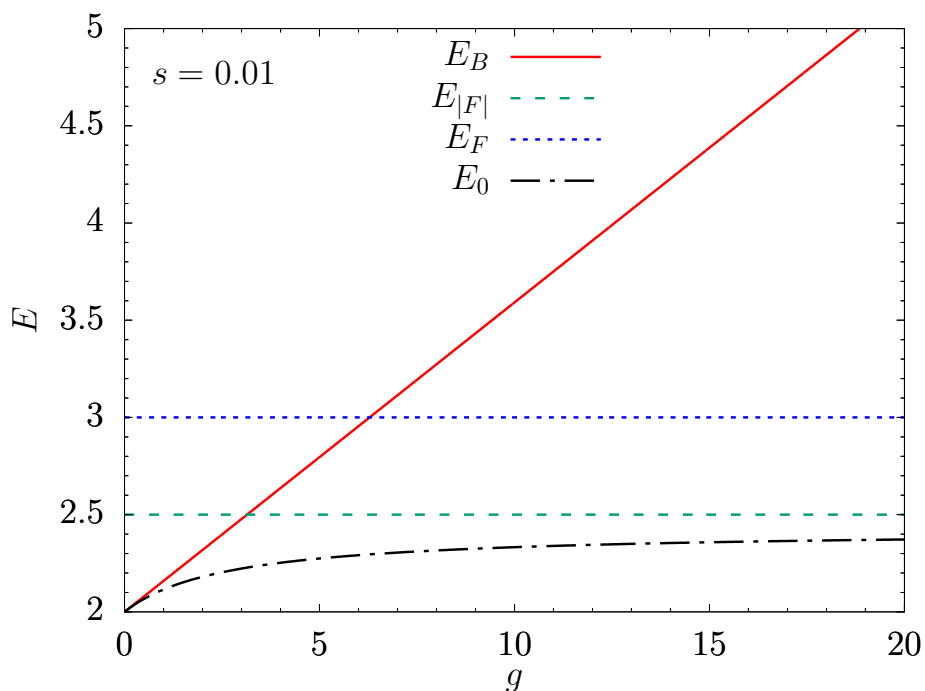

Figure 4.3: Ground state energy of two interacting bosons in a harmonic trap, E_0, depending on the interaction strength, g, and for a fixed range, s, computed by minimizing E_J. This value is compared with the expectation value of the energy of the wave functions of two noninteracting bosons, E_B, two noninteracting fermions, E_F, and the corresponding symmetrized wave function, $E_{|F|}$, which are given in Eqs. (4.3), (4.6), and (4.8), respectively.

minimized value of E_J. In Fig. 4.3, we see how this energy goes from E_B for $g \simeq 0$ to be close to $E_{|F|}$ when g becomes large. E_B, E_F and $E_{|F|}$ depend linearly on the interaction strength g (see, respectively, Eqs. (4.3), (4.6), (4.8)). However, the slope of the lines corresponding to E_F and $E_{|F|}$ in Fig. 4.3 is positive but very small, due to the small value of s.

In the strongly-interacting limit, in Fig. 4.3, we see that the upper-bound provided by $\Psi_{|F|}$ to the ground-state energy is closer to it than the one provided by Ψ_F, but it is still far from being compatible with E_0. Regarding the energy contributions of the kinetic and the potential energies corresponding to $\Psi_{|F|}$, they are 1 and 3/2, respectively, and do not coincide with the values found for the ground state for $s = 0.01$ (see Fig. 4.1). However, in the next section, we will see that, depending on the range of the interaction, the bosonized wave function, $\Psi_{|F|}$, can describe properly some of the features of the interacting two-boson system.

4.2.2 Dependence on the interaction range for a large interaction strength

In this section, we fix the interaction strength and we explore the dependence of the energy on the range, s, of the interaction. The main goal is to see if tuning s, the interacting two-boson system can be described by the bosonized wave function $\Psi_{|F|}$. In other words, we want to discern if there exists a regime where the ground-state energy is well-approximated by $E_{|F|}$, paying attention not only to the total energy but also to the partial energy contributions.

In Fig. 4.4, we compare the ground state energy of the interacting two-boson system computed numerically, both diagonalizing and minimizing E_J, with the expectation values given by the analytic wave functions. For a fixed and large interaction strength, $g = 20$, reducing the range of the interaction results in a decrease of the ground state energy of the system. The same kind of behavior is observed for Ψ_F and its symmetrized wave function, $\Psi_{|F|}$. Since their dependence on the interaction is the same, the shift in energy between them is due to the noninteracting part of the Hamiltonian. Differently, the energy for Ψ_B increases for decreasing s.

When using Ψ_J, the effect of changing the interaction range with $g = 20$ is reflected in the optimal variational parameters, that are shown in Fig. 4.5. The most sensitive one is β^*. In the short-range limit, when $s \to 0$, $1/b^*$ goes also to 0 as the interaction is only important at short distances. When the interaction range increases, the correlations between the particles extend to larger distances, which is reflected in a rapid increase of $1/b^*$ with increasing s. β^* also becomes larger at larger values of the range of the interaction. The value of a^* is not notably changing with s and is always close to 1, as we are in the large g limit, $g = 20$.

We observe, in Fig. 4.4, that in the whole interval of values of s, $E_{|F|}$ is a good upper-bound to the ground-state energy. In particular, when $s \in [0.3, 0.5]$ the energy given by the bosonized wave function is very close to E_0. Moreover, in Fig. 4.6, we observe that the way the energy is
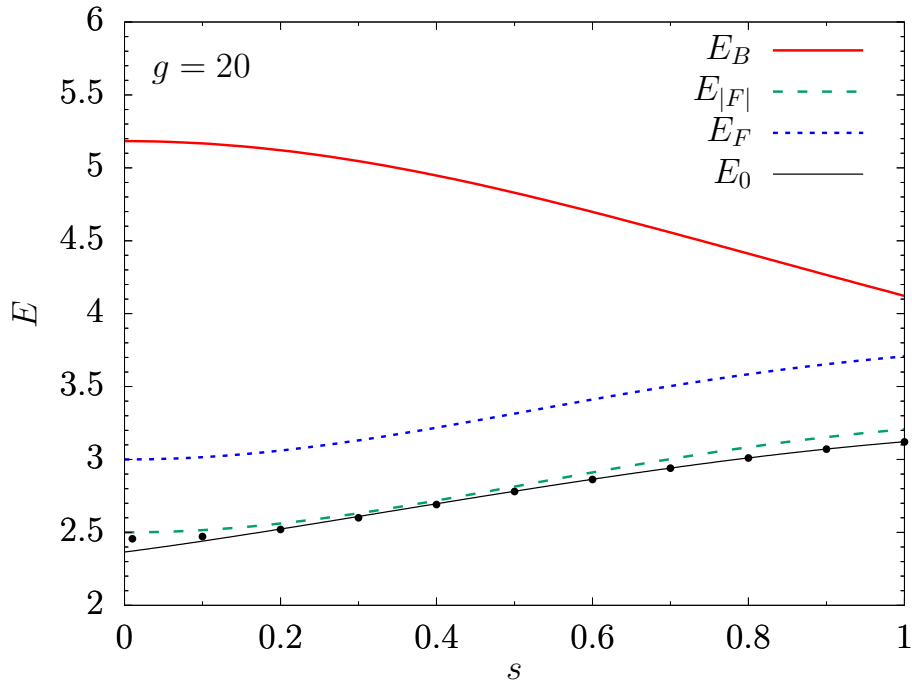
Figure 4.4: Ground state energy of two interacting bosons in a harmonic trap, E_0, depending on the interaction range, s, and for a fixed interaction strength, g. Black dots: Energies computed by numerical diagonalization of the Hamiltonian matrix. Solid black line: Energies computed with the variational ansatz Ψ_J given in Eq. (4.16). The numerical results are compared with the expectation value of the energy of the wave functions of two noninteracting bosons, E_B, two noninteracting fermions, E_F, and its symmetrized wave function, $E_{|F|}$, which are given, respectively, in Eqs. (4.3), (4.6), and (4.8).

distributed is comparable to the different energy contributions to $E_{|F|}$. For instance, at $s = 0.5$, we find that $\langle \mathcal{V}_{\text{ho}} \rangle \approx 1.50$, $\langle \mathcal{K} \rangle \approx 1.07$, and $\langle \mathcal{V}_{\text{int}} \rangle \approx 0.22$, and the corresponding values of $\Psi_{|F|}$ are very similar: $3/2$ for the harmonic potential energy and 1 for the kinetic energy. Regarding the interaction energy, we get 0.31 for the bosonized wave function. That value is larger than the one corresponding to the ground state and it is the main responsible for the difference between $E_{|F|}$ and E_0.
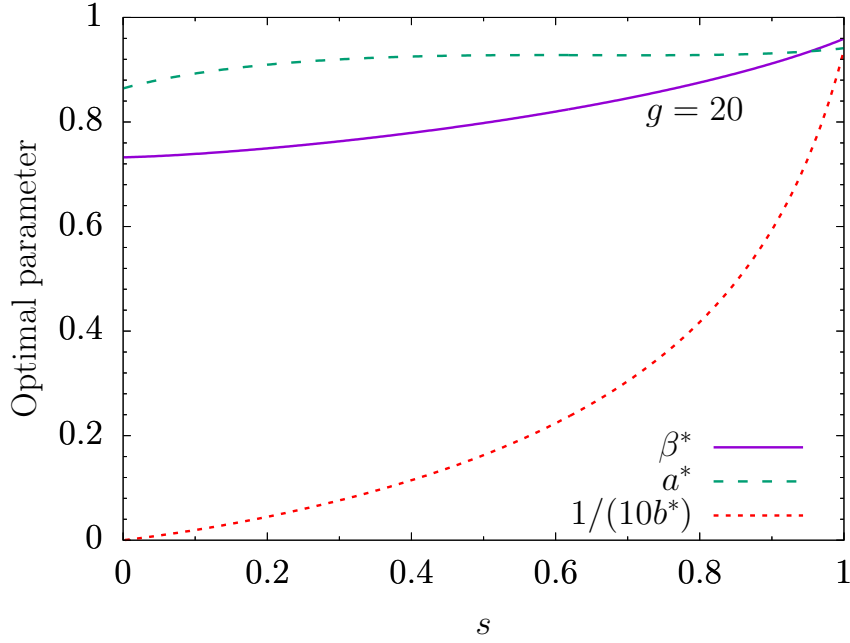
Figure 4.5: Variational parameters that minimize the energy E_J for a fixed interaction strength, $g = 20$, as a function of s.
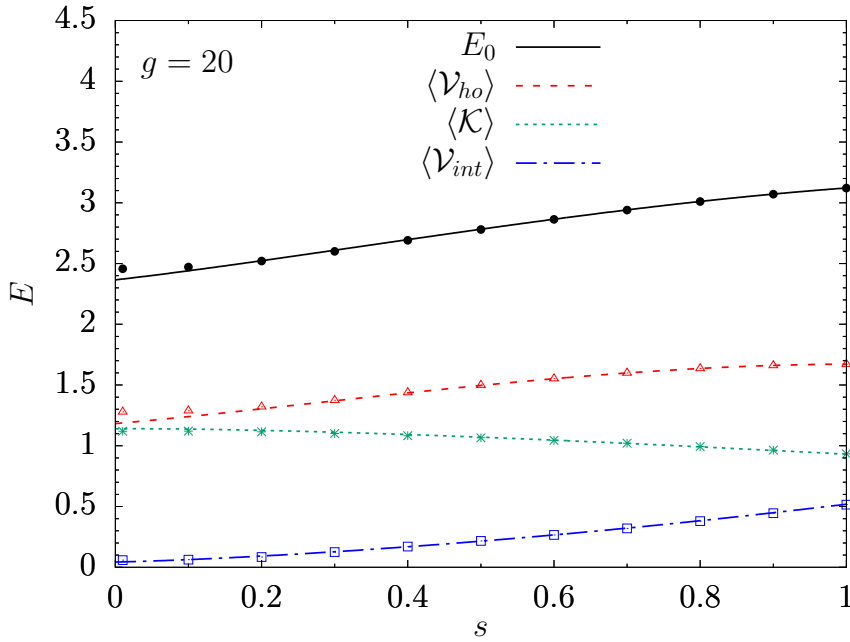

Figure 4.6: Ground state energy of two interacting bosons in a harmonic trap, E_0, depending on the interaction range, s, for a fixed interaction strength, g. We also show the different contributions, $\langle \mathcal{V}_{ho} \rangle$, $\langle \mathcal{K} \rangle$, and $\langle \mathcal{V}_{int} \rangle$. Symbols: Energies computed by diagonalization. Lines: Energies computed with the variational ansatz Ψ_J given in Eq. (4.16).

4.3   Spatial density profiles and two-body correlation functions

In this section, we compare the density profile and the pair correlation function of the ground state of the trapped two-boson system, with and without interactions, with the ones provided by Ψ_F and $\Psi_{|F|}$. The density operator and the pair correlation operator were defined in Eq. (B.1) and in Eq. (B.17) of the previous Chapter, respectively. Since we consider the case of two identical particles, we compute the density profile and the pair correlation function for a given state $\Psi(\vec{x}_1, \vec{x}_2)$, respectively, as follows: $\rho(\vec{x}) = \int d\vec{x}_2 \, |\Psi(\vec{x}, \vec{x}_2)|^2$, and $\eta(\vec{x}, \vec{x}') = |\Psi(\vec{x}, \vec{x}')|^2$.

Using Cartesian coordinates, the wave functions of Section 4.1 read

$$\Psi_B(\vec{x}_1, \vec{x}_2) = \frac{1}{\pi} e^{-\frac{1}{2}(x_1^2 + y_1^2 + x_2^2 + y_2^2)}, \tag{4.22}$$

$$\Psi_F^{\pm}(\vec{x}_1, \vec{x}_2) = \frac{1}{\pi\sqrt{2}} e^{-\frac{1}{2}(x_1^2 + y_1^2 + x_2^2 + y_2^2)} \left((x_1 - x_2) \pm i(y_1 - y_2) \right), \tag{4.23}$$

$$\Psi_{|F|}(\vec{x}_1, \vec{x}_2) = \frac{1}{\pi\sqrt{2}} e^{-\frac{1}{2}(x_1^2 + y_1^2 + x_2^2 + y_2^2)} \sqrt{(x_1 - x_2)^2 + (y_1 - y_2)^2}, \tag{4.24}$$

$$\Psi_J(\vec{x}_1, \vec{x}_2) = N_J e^{-\frac{1+\beta}{4}(x_1^2 + y_1^2 + x_2^2 + y_2^2)} e^{-\frac{1-\beta}{2}(x_1 x_2 + y_1 y_2)} \left(1 - a e^{-b\left((x_1 - x_2)^2 + (y_1 - y_2)^2 \right)} \right). \tag{4.25}$$

The corresponding density profiles and pair correlation functions read

$$\rho_B(\vec{x}) = \frac{1}{\pi} e^{-(x^2 + y^2)}, \tag{4.26}$$

$$\eta_B(\vec{x}, \vec{x}') = \frac{1}{\pi^2} e^{-(x^2 + y^2 + x'^2 + y'^2)}, \tag{4.27}$$

$$\rho_F(\vec{x}) = \rho_{|F|}(\vec{x}) = \frac{1}{2\pi} e^{-(x^2 + y^2)} (1 + x^2 + y^2), \tag{4.28}$$

$$\eta_F(\vec{x}, \vec{x}') = \eta_{|F|}(\vec{x}, \vec{x}') = \frac{1}{2\pi^2} e^{-(x^2 + y^2 + x'^2 + y'^2)} \left((x - x')^2 + (y - y')^2 \right), \tag{4.29}$$

$$\rho_J(\vec{x}) = N_J^2 2\pi e^{-2(x^2 + y^2)} \left(\frac{e^{\frac{2(x^2 + y^2)}{1+\beta}}}{1+\beta} - \frac{2a e^{\frac{2(x^2 + y^2)}{1+\beta+2b}}}{1+\beta+2b} + \frac{a^2 e^{\frac{2(x^2 + y^2)}{1+\beta+4b}}}{1+\beta+4b} \right), \tag{4.30}$$

$$\eta_J(\vec{x}, \vec{x}') = N_J^2 e^{-\frac{1+\beta}{2}(x^2 + y^2 + x'^2 + y'^2)} e^{(\beta - 1)(xx' + yy')} \left(1 - a e^{-b\left((x - x')^2 + (y - y')^2 \right)} \right)^2. \tag{4.31}$$

Note that both the fermionic and bosonized wave functions give the same density and pair correlation as $|\Psi_{|F|}(\vec{x}_1, \vec{x}_2)|^2 = |\Psi_F^{\pm}(\vec{x}_1, \vec{x}_2)|^2$.

From the pair correlation function and the density profile, we compute the probability of finding a particle at a distance $X \equiv \sqrt{x^2 + y^2}$ once we have located the other at the origin, defined in Eq. (3.48). We get the following distributions:

$$P_B(X; 0) = \frac{1}{\pi} e^{-X^2}, \tag{4.32}$$

$$P_F(X; 0) = P_{|F|}(X; 0) = \frac{1}{\pi} e^{-X^2} X^2, \tag{4.33}$$

$$P_J(X; 0) = \frac{e^{-\frac{1+\beta}{2}X^2} \left(1 - a e^{-bX^2} \right)^2}{2\pi \left(\frac{1}{1+\beta} - \frac{2a}{1+\beta+2b} + \frac{a^2}{1+\beta+4b} \right)}. \tag{4.34}$$

In Fig. 4.7, panels (a) and (c), we compare the density profiles obtained numerically for the ground state of the interacting two-boson system with the density profile corresponding to the noninteracting case and to the noninteracting two-fermion system. We show that, for a given range, there is an interaction strength such that the density profile of the interacting two-boson system is very well approximated by the noninteracting two-fermion density profile. The smaller the interaction range is, the greater the interaction strength is for which the density profiles coincide. Therefore, in the short-range limit a very strong interaction strength would be required to reproduce the noninteracting two-fermion profile with the two interacting bosons.

In the case of the probability of finding a particle in space once we have found the other at the origin, we observe, in Fig. 4.7, panels (b) and (d), that the numerically computed probabilities for the interacting two-boson system resemble the corresponding ones for two noninteracting fermions. However, the maximum peak does not coincide, and it is closer to the center of the trap for two noninteracting fermions.

The effect of decreasing the interaction range for a fixed interaction strength is shown in Fig. 4.8. The opposite situation, having a fixed range and a varying interaction strength, was studied in the previous Chapter. Regarding the density profile, in panels (a) and (c), we see that when the range decreases the profile approaches the one corresponding to noninteracting bosons. That is explained because the interaction strength, $g = 20$, is not sufficiently strong for the cases with the smallest ranges depicted. For instance, comparing with previous Fig. 4.7, in the case of $s = 0.3$ the profile ρ_F is approached at very large values of g, $g = 50$.

Looking at the probabilities $P(X; 0)$, for the larger values of s depicted in panels (b) and (d) of Fig. 4.8, the fermionic P_F is qualitatively reproduced, as there is a maximum peak at $X \approx 1$ and the probability of finding the two bosons together, at $X = 0$, vanishes. However, when the range is further reduced, in panel (d) we see that $P(X; 0)$ becomes closer to the one of the noninteracting two-boson system, P_B. The value of the interaction strength, $g = 20$, is sufficiently large in order to avoid finding the atoms at the same position but a stronger interaction strength would be necessary to find them more separately.
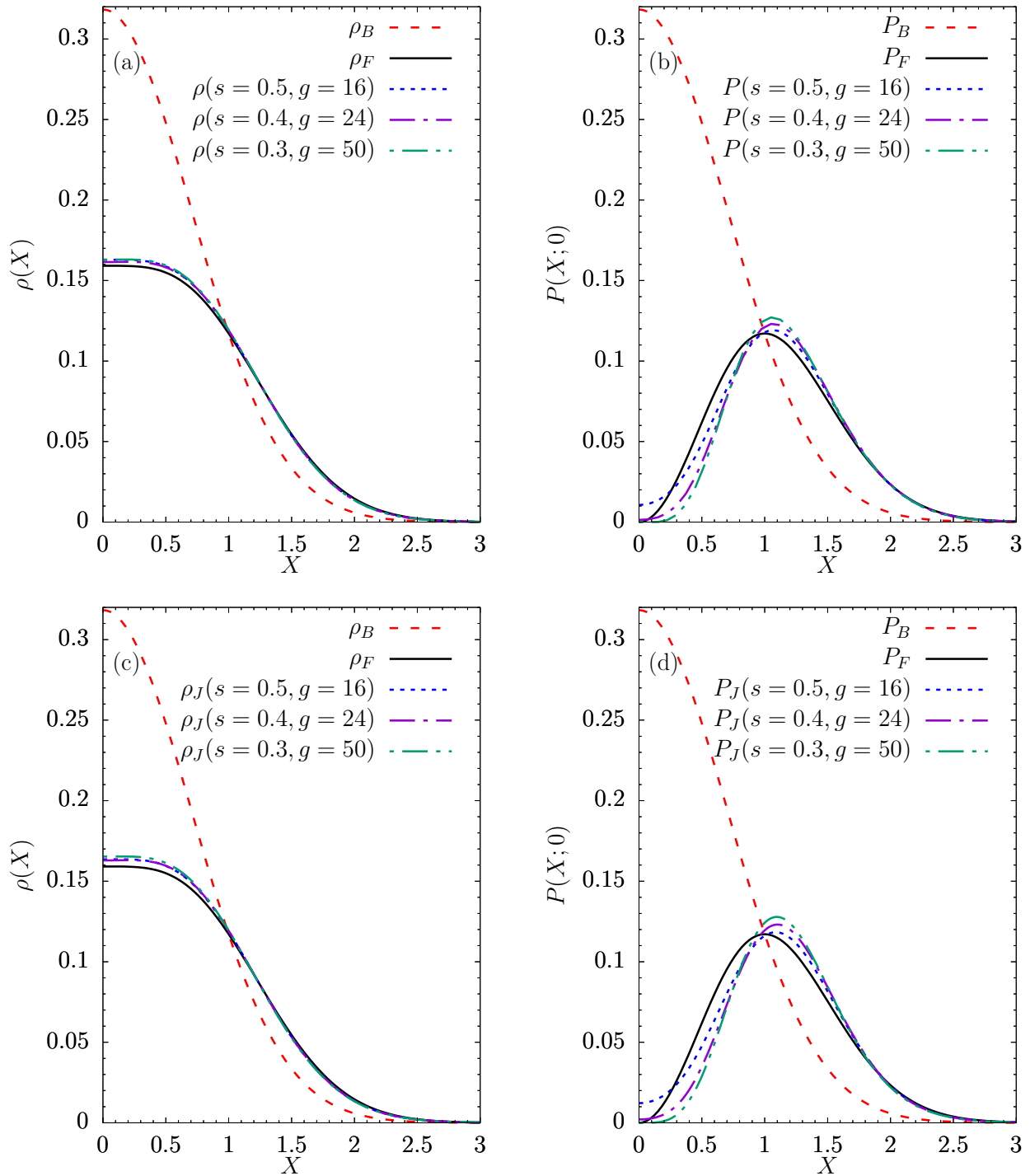
Figure 4.7: (a) Density profiles of two noninteracting bosons, ρ_B, two noninteracting fermions, ρ_F, and three profiles computed by numerical diagonalization for different ranges and interaction strengths for the interacting two-boson system. (b) Probability of finding a particle at a distance X from the origin once a particle is found at $X = 0$ under the same conditions. In (c) and (d) the same cases as in (a) and (b), respectively, but computed with the variational parameters that minimize E_J replaced in Eq. (4.30) and Eq. (4.34), respectively.

Figure 4.8: (a) Density profiles of two noninteracting bosons, ρ_B, two noninteracting fermions, ρ_F, and profiles computed by numerical diagonalization for different ranges fixing the interaction strength. (b) Probability of finding a particle at a distance X from the origin once a particle is found at $X = 0$ under the same conditions. In (c) and (d) the same cases as in (a) and (b), respectively, but computed with the variational parameters that minimize E_J replaced in Eq. (4.30) and Eq. (4.34), respectively. In (c) and (d), more cases are shown.
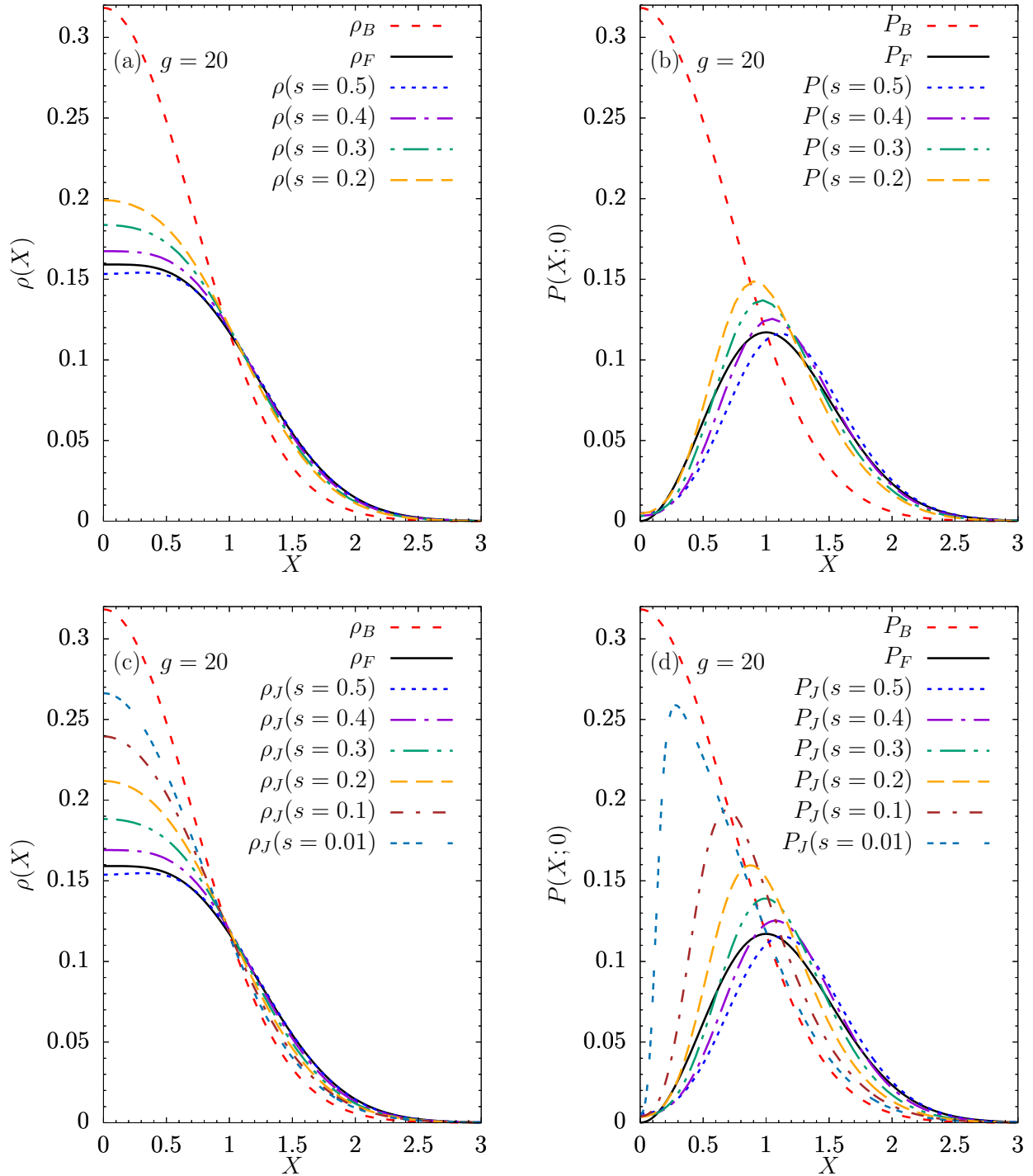
Chapter 5

FEW-BOSON LOCALIZATION IN A CONTINUUM WITH SPECKLE DISORDER

In the previous Chapters, we have studied the effect of interactions in few-boson systems in two dimensions. The main result was the appearance of correlations in the system. In this Chapter we explore the effect of interactions in a fairly different setup. We apply the diagonalization method described in Chapter 2 to study the phenomenon of localization in a one-dimensional system of interacting bosons. The localization is present at the single-particle level and occurs due to the presence of disorder, which is introduced by a correlated random potential in space. We discern if the system is localized or not through the statistical analysis of the spacings between the energy levels of the system over several different speckle potentials. Our goal is to determine if the few-boson system remains localized in the presence of a repulsive contact potential or the interactions delocalize it. The model we consider is tailored to describe a setup that can be implemented in cold-atom experiments [124, 125].

The analysis of the energy-level spacing statistics is familiar from quantum chaos and random matrix theories [126, 127]. In this framework, one discerns delocalized ergodic states from localized states by identifying the Wigner-Dyson statistical distribution and the Poisson distribution of the level spacings, respectively. This approach has been commonly adopted in studies on single-particle Anderson localization in discrete lattice models [128–131], and more recently also in continuous-space (single-particle) models relevant for cold-atoms experiments [132,133]. Chiefly, this approach has been established as one of the most sound criteria to identify many-body localized phases [134], since it allows one to identify the breakdown of ergodicity independently of the specific mechanism causing localization, including, e.g, localization in Fock space. In this context, it has been applied

to one-dimensional discrete systems, including spin models [135–138], spinless fermion models [134, 139], and recently also to bosonic models [140, 141].

In Sec. 5.1 we describe the continuous-space model with speckle disorder and the computational approach we adopt, analyzing in particular the convergence of the energy levels as a function of the basis size. In Sec. 5.2, we focus on a single particle in the speckle disorder. First, we analyze the spatial structure of the eigenstates of a single speckle potential. In second place, we present the statistical level-spacing analysis and apply it to the single-particle case in order to identify a proper localization phenomenon by tuning the speckle parameters. In this section, we also consider the noninteracting system of many-bosons. We show that the localization criterion has to be applied with care and that a possible strategy is to use a randomness filter. The results for two-boson and three-boson systems are presented in Sec. 5.3. Our analysis consists in determining if the system remains localized when the strength of the interaction is increased.

5.1 The Hamiltonian of interacting bosons in a speckle potential

In the general case, the model we consider consists in N identical bosons of mass m in a one-dimensional box of size L, with a random external field $V(x)$ that describes a blue-detuned optical speckle field [142]. The Hamiltonian reads,

$$\mathcal{H} = \sum_{i=1}^{N} \left(-\frac{\hbar^2}{2m}\frac{\partial^2}{\partial x_i^2} + V(x_i) \right) + \sum_{i<j}^{N} v(|x_i - x_j|). \tag{5.1}$$

The variables x_i, with $i = 1, \dots N$, indicate the particle coordinates. Hard-wall boundary conditions are considered, meaning that the wave functions vanish at the system boundaries. $v(|x_i - x_j|)$ indicates a zero-range two-body interaction potential between particles i and j, defined as,

$$v(|x_i - x_j|) = g\delta(|x_i - x_j|). \tag{5.2}$$

The coupling parameter g, which fixes the interaction strength, is related to the one-dimensional scattering length, a_0, as $g = -\hbar^2/(ma_0)$. In this work, we consider a repulsive interaction, $g \geqslant 0$. The one-dimensional Hamiltonian (5.1) accurately describes ultracold gases in one-dimensional waveguides with a tight radial confinement, and the interaction parameter g can be tuned either by varying the radial confining strength and/or tuning the three-dimensional scattering length via Feshbach resonances [143].

The external field $V(x)$ describes the potential experienced by alkali atoms exposed to optical speckle fields. Such fields are generated when coherent light passes through a rough (semitransparent) surface. An efficient numerical algorithm to create speckle fields in computer simulations has been described in Refs. [144–147], and we refer the readers interested in more details about the algorithm to those references.

Fully developed speckle fields in large systems are characterized by an exponential probability distribution of the local intensities V, which reads $P(V) = \exp(-V/V_0)/V_0$ for $V \geqslant 0$, and $P(V) = 0$ for $V < 0$ [142]. Here, $V_0 \geqslant 0$ is the average intensity of the field, and coincides with its standard deviation. V_0 is therefore the unique parameter that characterizes the disorder strength.

The two-point spatial correlation function of local intensities of a speckle field depends on the distance d between two given points and reads [145],

$$\Gamma(d) = \frac{\langle V(x+d)V(x)\rangle}{V_0^2} - 1 = [\sin(d\pi/\ell)/(d\pi/\ell)]^2 \,. \tag{5.3}$$

Here, the brackets $\langle \cdots \rangle$ indicate spatial averages. Notice that in a large enough system, the speckle field is self-averaging, meaning that spatial averages can be replaced by averages of local values over many realizations of the speckle field. The length scale ℓ is related to the inverse of the aperture width of the optical apparatus employed to create the optical speckle field and to focus it onto the atomic cloud. It characterizes the typical distance over which the local intensities loose statistical correlations, or, in other words, the typical size of the speckle grains. In the following, we will use this spatial correlation length as unit of lengths, setting $\ell = 1$. This length scale also allows one to define a characteristic energy scale, often referred to as correlation energy, which reads $E_c = \hbar^2/(m\ell^2)$. This quantity will be used in the following as the unit for energies, unless explicitly stated. The interaction parameter g will be expressed in units of $\hbar^2/(\ell m)$.

5.1.1 The second-quantized Hamiltonian

The few-body problem is solved by direct diagonalization of the second-quantized many-body Hamiltonian in the truncated many-body basis introduced in Sec. 2.6. The Hamiltonian (5.1) is written in second-quantization as the sum of three terms:

$$\hat{H} = \hat{K} + \hat{V} + \hat{v} \,. \tag{5.4}$$

Each term is written using the creation and annihilation operators introduced in Chapter 2, $\hat{a}_i^\dagger$ and $\hat{a}_j$, that create or annihilate bosons in the single-particle states written in Eq. (2.39), which are the eigenstates of the free particle moving in a one dimensional box with hard walls. The box size is chosen large enough compared to the spatial correlation length ℓ. In this basis, the kinetic energy, $\hat{K}$, has diagonal form,

$$\hat{K} = \sum_k \frac{k^2\pi^2}{2L^2}\hat{a}_k^\dagger\hat{a}_k \,. \tag{5.5}$$

The speckle potential reads

$$\hat{V} = \sum_{kj} V_{kj}\hat{a}_k^\dagger\hat{a}_j \,, \tag{5.6}$$

with

$$V_{kj} = \int_{-\frac{L}{2}}^{\frac{L}{2}} dx \ \psi_k^*(x)V(x)\psi_j(x) \,, \tag{5.7}$$

$E_{\max}$	M	D_{MB}	$E_{GS}(g=0)$	$E_{GS}(g=1)$	$E_{GS}^{h.o.}(g=1)$
20	142	7941	7.0266	7.7813	1.3249
40	201	15889	6.8818	7.5954	1.3191
60	246	23836	6.8328	7.5403	1.3167
100	318	39747	6.8309	7.5338	1.3143
120	348	47697	6.8308	7.5319	1.3136

Table 5.1: Convergence of the ground state energy for $N = 2$: for a given speckle and in the noninteracting case (forth column) and for $g = 1$ (fifth column); for an harmonic potential and $g = 1$ (sixth column) that should tend to the exact value $E_{GS}^{h.o.} \cong 1.30675$ [30]. $E_{\max}$ was used to truncate the many-body Hilbert space using an energy criterion which required M single-particle states and it corresponds to a many-body Hilbert space dimension D_{MB}. The system size is $L = 100\ell/\sqrt{2}$ and in the cases with a harmonic trap we have set $\sqrt{\hbar/(m\omega)} = \ell$, i.e., $\hbar\omega = E_c$. For the speckle potential $V_0 = 50E_c$.

where $\psi_k(x)$ was given in Eq. (2.39). These integrals are determined via numerical quadrature based on the composite five-point Bode's rule, using a sufficiently fine grid so that the residual numerical error due to the discretization is negligible.

The interaction term reads

$$\hat{v} = \frac{g}{2} \sum_{i,j,k,l} v_{ijkl} \hat{a}_i^\dagger \hat{a}_j^\dagger \hat{a}_k \hat{a}_l, \tag{5.8}$$

with

$$v_{ijkl} = \frac{1}{2L} \left(-\delta_{i,j+k+l} + \delta_{i,-j+k+l} + \delta_{i,j-k+l} - \delta_{i,-j-k+l} \right.$$
$$\left. + \delta_{i,j+k-l} - \delta_{i,-j+k-l} - \delta_{i,j-k-l} + \delta_{i,-j-k-l} \right). \tag{5.9}$$

Using the many-body basis of Sec. 2.6 translates here into including all states with a kinetic energy equal or smaller than a given threshold $E_{\max}$. The energy threshold, $E_{\max}$, represents an algorithmic parameter whose role has to be analyzed. In fact, while the computation is exact in the $E_{\max} \to \infty$ limit, a residual truncation error might occur for a finite $E_{\max}$ value.

Table 5.1 reports the analysis of the convergence with the energy truncation parameter $E_{\max}$ for a few representative setups. D_{MB} in this table indicates the number of states in the many-body basis set. Specifically, we consider the ground-state energy of two bosons in the noninteracting case ($g = 0$) and with a relatively strong interaction ($g = 1$). Here the disorder strength is set to $V_0 = 50E_c$. One notices that with the largest basis set the residual truncation error is much smaller than 0.1%. While the truncation effect becomes somewhat larger at higher energies, we consider in this work an energy range where this effect is negligible. An estimate of the accuracy of our numerical procedure can be obtained by considering the case of two interacting bosons trapped
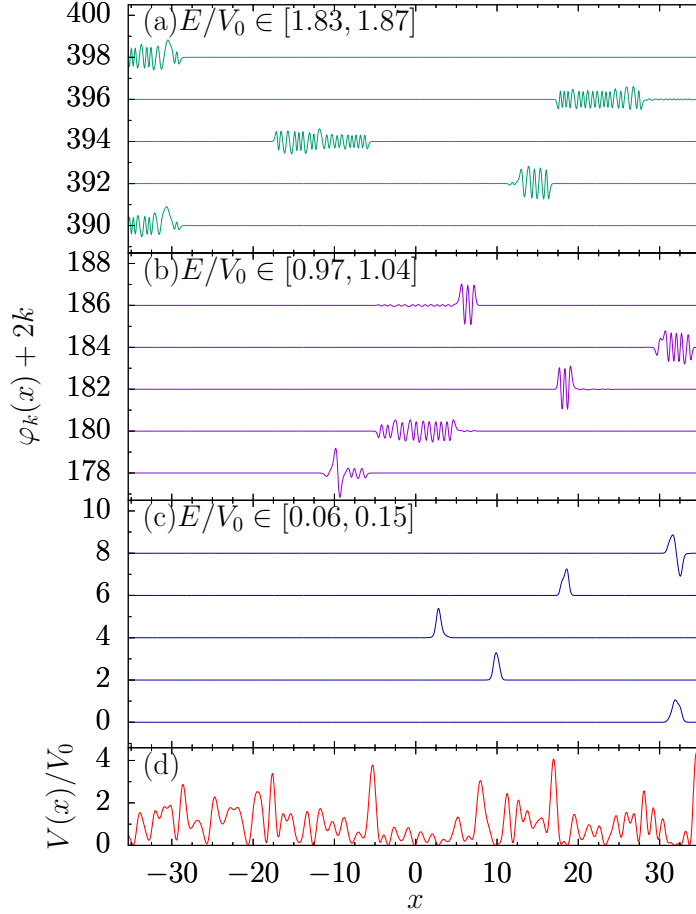
Figure 5.1: In panels (a-c), we present some eigenfunctions of the speckle potential, $V(x)$, from bottom to top, in order of increasing energy in the energy ranges written in the panels. A realization of the speckle potential with $V_0 = 50E_c$ is shown in panel (d). The system size is $L = 100\ell/\sqrt{2}$.

in a harmonic potential, which was exactly solved in Ref. [30]. We choose a harmonic oscillator of length ℓ, which is the typical size of the minima in the speckle potential, within our finite box of size $L = 100\ell/\sqrt{2}$. For an interaction strength $g = 1$ we reproduce the exact results up to the second decimal. This provides a reasonable estimate of the accuracy of our method. Furthermore, we mention here that the results of the analysis of the (ensemble averaged) level-spacing statistics are less sensitive to the truncation error than the individual energy levels of a single realization of the speckle field.

5.2   Localization in the single-particle case

5.2.1   Eigenstates of a speckle potential

First of all, we start studying the properties of the eigenstates of a single speckle potential that has been chosen arbitrarily. Fig. 5.1 displays the single-particle wave-functions at low, intermediate, and relatively high energies, for a given realization of a speckle field of intensity $V_0 = 50E_c$. For low-energy states, localization typically occurs in rare regions where the disorder creates a deep well confined by tall barriers. In fact, we observe that the spatial extent where these low-energy states have large amplitude is typically of the order of the disorder correlation length ℓ, meaning that they are indeed localized in a single well of the speckle field. However, this spatial extent rapidly increases as a function of the energy, becoming significantly larger than ℓ. On a qualitative level, this effect can be observed in Fig. 5.1, noticing that the states at intermediate and at relatively high energies have large amplitude in several wells of the speckle potential. To quantify this spatial extent, we compute the participation ratio, which is defined as $P_k = 1/\int \mathrm{d}x \, |\varphi_k(x)|^4$. For the low-energy states in the Lifshitz tail, we find, again for $V_0 = 50E_c$, $\langle P_k \rangle \simeq \ell$, indeed corresponding to trapping in a single deep well. Here the brackets $\langle \cdot \rangle$ indicate the average over many realizations of the speckle field. Instead, for states with energies above the average speckle-field intensity, e.g., with energy $E \simeq 2V_0$, the spatial extent is $\langle P_k \rangle \simeq 5\ell$, and it reaches $\langle P_k \rangle \simeq 11\ell$ at $E \simeq 3V_0$. At even higher energies the participation ratio is of the order of the system size (here $L = 100\ell/\sqrt{2}$) and finite-size effects due to the box become dominant. At these energies the single-particle states are weakly affected by the disorder, since in the finite system the speckle field typically develops only moderately high peaks, as opposed to an infinite system where a sufficiently high peak would always occur given that the speckle potential has no upper bound. Clearly, these finite-size effects have to be avoided (see also the discussion on the analysis of the level-spacing statistics reported below). The choice of inspecting that localization occurs in a sufficiently small length scale and in a reasonably broad portion of the energy spectrum, here taken of the order of the average speckle field intensity V_0, is motivated by the aim to address, in the second step, the effects of interparticle interactions. These will indeed induce population of relatively high-energy states even when noninteracting bosons would occupy only deeply localized low-lying modes. In fact, previous lattice calculations predicted that in one dimension the localization length of two interacting particles can be significantly larger than the spatial extent of the single-particle states [148]. In three-dimensional (lattice) systems two-particle repulsive interactions could even induce complete delocalization [149]. One should also consider that in cold-atom experiments the atomic energy distribution is inevitably broadened by thermal excitations, by interactions, and by the finite spatial spread of the atomic cloud, meaning that localization effects cannot be observed if only very few low-energy states are spatially localized. In this regard, it is worth mentioning

that if one aims at experimentally visualizing the exponentially decaying tails of the single-particle states, a feature that characterizes Anderson localized systems, it is convenient to consider rather weak disorder $V_0 \approx E_c$, since in this regime the spatial extent is much larger than the typical well size. For example, for a speckle-field intensity $V_0 = E_c$ we find $P_k \simeq 20\ell$ at $E = 3V_0$. In this case, in order to avoid finite-size effects in the participation-ratio calculation (and also in the analysis of the level spacing statistics discussed below), a system size larger than $L = 1000\ell/\sqrt{2}$ is required. Such system sizes cannot be addressed with the computational technique we employ for interacting systems, therefore in the following we consider larger disorder strengths where finite size effects can be more easily suppressed. Anderson localization in strong speckle disorder has been investigated also in Ref. [150].

It is also worth emphasizing that in an infinite one-dimensional system where the disorder has no upper bound (like the blue-detuned speckle potential), a classical particle is localized at any energy E, just like a quantum particle in the same setup [151]. Indeed, a position in space where $V(x) > E$ always occurs, prohibiting the particle from exploring the whole configuration space, resulting in a nonergodic behavior. This scenario is different from the one that occurs in two-dimensional [152] and in three-dimensional systems, where classical particles in a speckle potential are trapped only if their energy is lower than a finite threshold; above this energy threshold a (classical) percolation transition takes place. In particular, in three dimensional speckle potentials the classical percolation threshold turns out to be a tiny fraction of the average speckle-potential intensity V_0 [147, 153]. The mobility edge, i.e. the energy threshold that in three dimensional quantum systems separates localized states from extended states, is typically much larger than this classical percolation threshold, meaning that in a broad energy range particles are trapped purely by quantum mechanical effects. In the one-dimensional setup considered here, instead, both quantum and classical particles are localized at any energy in the infinite-size limit, meaning that classical and quantum trapping mechanisms cannot be rigorously separated.

5.2.2 Statistical analysis of the energy-level spacings

The analysis of the statistical distribution of the spacings between consecutive energy levels allows one to discern localized (i.e., nonergodic) states from delocalized ergodic states. Specifically, localized states are associated to the Poisson distribution of the level spacings, while delocalized states are associated to the Wigner-Dyson distribution typical of random matrices. An efficient procedure to identify these two distributions consists in determining the average over a large ensemble of speckle fields of the following ratio of consecutive level spacings [134]:

$$r_i = \min\left\{ \frac{E_{i+1} - E_i}{E_i - E_{i-1}}, \frac{E_i - E_{i-1}}{E_{i+1} - E_i} \right\}. \tag{5.10}$$
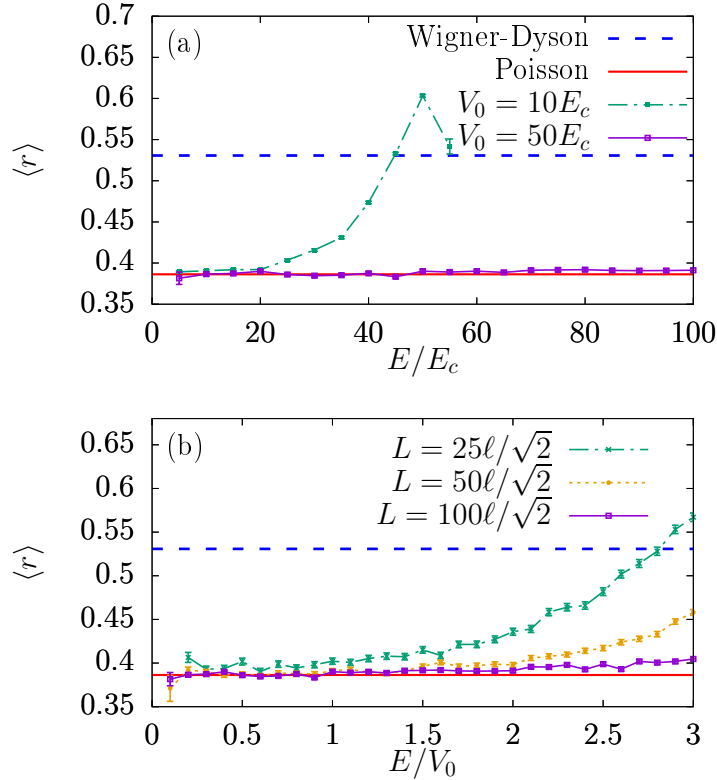
Figure 5.2: The value of $\langle r \rangle$ averaged over 2000 different speckle instances is shown. In (a) we compare two cases with different speckle intensity, V_0, and in (b) with different system sizes. In panel (a) $L = 100\ell/\sqrt{2}$ and in panel (b) $V_0 = 50E_c$. The distribution in energy is computed using energy windows $\Delta E = 5E_c$. The diagonalization was performed using Hilbert spaces of dimension 1000.

Notice that the ensemble averaging we perform, indicated as $\langle r \rangle$, is energy resolved, meaning that only states within a narrow energy window are considered. This allows us to address possible scenarios where both localized states and delocalized states occur, but in different sectors of the energy spectrum. The Poisson distribution translates to the ensemble average $\langle r \rangle \cong 0.38629$, while the Wigner-Dyson distribution translates to $\langle r \rangle \cong 0.53070$ [154].

As discussed above, the scaling theory of Anderson localization [151] predicts that in infinite one-dimensional disordered systems the localization occurs for any amount of disorder, even if this amount is vanishingly small. However, in finite-size systems the localization length might be comparable to the system size, hindering the observation of the Poisson distribution corresponding to localized systems. This effect is particularly relevant if the disorder is weak or if the energy window under consideration is high, since the localization length is large in these regimes, as previously discussed. It is, therefore, pivotal for our purposes to identify a disorder strength and
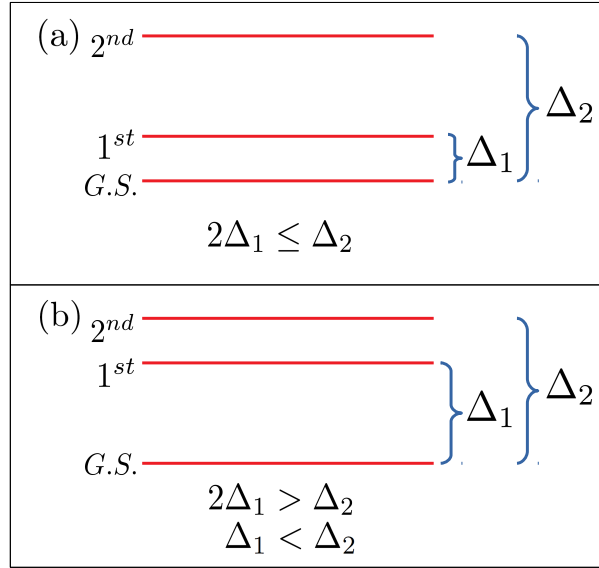
Figure 5.3: The lowest single-particle eigenenergies for a given speckle potential determine the lowest energy levels for the noninteracting many-body system. There are two possible situations: (a) a small gap between the single-particle ground state (*G.S.*) and the first excited state (1st); and (b) a small gap between the first excited state and the second excited state (2nd).

an energy range where the Poisson statistics can be observed in a system size that is feasible for our computational approach for interacting systems. Fig. 5.2 displays the energy-resolved analysis of the level-spacings statistics for a few representative setups of the optical speckle field. Specifically, panel (a) shows $\langle r \rangle$ versus E/E_c for a fixed system size and different disorder strengths, while panel (b) shows data corresponding to different system sizes at a fixed disorder strength. One observes that, at low energy, the $\langle r \rangle$ values precisely agree with the prediction for the Poisson distribution, indicating that the low-energy states are localized on a sufficiently small length scale. However, significant deviations occur at higher energies. We attribute them to the finite-size effect discussed above. In fact, one observes that for larger system sizes the Poisson-distribution result extends to higher energies. This finding is consistent with the expectation that in an infinite system the whole energy spectrum would be localized. In the following, we will consider the system size $L = 100\ell/\sqrt{2}$ and the disorder strength $V_0 = 50E_c$, where the $\langle r \rangle$ values precisely correspond to the statistics of localized systems in a reasonably broad energy range $0 < E \lesssim 100E_c$. Notice that the upper limit is twice as large as the average speckle-field intensity V_0.

It is worth pointing out that the linear system size of typical cold-atom experiments performed with optical speckle field is comparable to the system size considered here; it ranges from a few

tens to around thousand times the speckle correlation length ℓ. Therefore, this analysis also serves as a guide for experiments on localization phenomena in atomic gases.

5.2.3   Randomness in the noninteracting many-boson system

While the next section is devoted to systems with $N = 2$ or $N = 3$ interacting bosons, we address here the special case of $N > 1$ noninteracting particles. Clearly, the system properties in this case can be traced back to the single-particle problem. However, as we discuss here, special care has to be taken in order to properly extract the correct level spacing statistics.

In fact, in certain circumstances, the N-boson energy-level spacings in the noninteracting limit take specific, nonrandom values. For instance, for a given realization of the speckle potential, we can distinguish two possible scenarios, depicted in the two panels of Fig. 5.3, depending on the relative distances of the first and of the second single-particle levels from the single-particle ground-state; they are indicated below as Δ_1 and Δ_2, respectively. For the scenario displayed in panel (a) of Fig. 5.3, where $2\Delta_1 < \Delta_2$, the three lowest-energy eigenstates of the noninteracting N-boson system are

$$|E_0\rangle = |N, 0, ..., 0\rangle,$$
$$|E_1\rangle = |N - 1, 1, 0, ..., 0\rangle, \qquad (5.11)$$
$$|E_2\rangle = |N - 2, 2, 0, ..., 0\rangle,$$

and their associated energies are (see Fig. 5.3)

$$E_0 = NE_{GS},$$
$$E_1 = NE_{GS} + \Delta_1, \qquad (5.12)$$
$$E_2 = NE_{GS} + 2\Delta_1,$$

where E_{GS} is the single-particle ground state energy. In this situation, the value of r_1 associated to the lowest energy of the system is

$$r_1 = \frac{E_1 - E_0}{E_2 - E_1} = \frac{\Delta_1}{\Delta_1} = 1. \qquad (5.13)$$

One notices that this ratio does not randomly fluctuate for different speckle-field realizations. In the second scenario (see panel (b) of Fig. 5.3), where $2\Delta_1 > \Delta_2$, the three lowest-energy eigenstates of the system are

$$|E_0\rangle = |N, 0, ..., 0\rangle,$$
$$|E_1\rangle = |N - 1, 1, 0, ..., 0\rangle, \qquad (5.14)$$
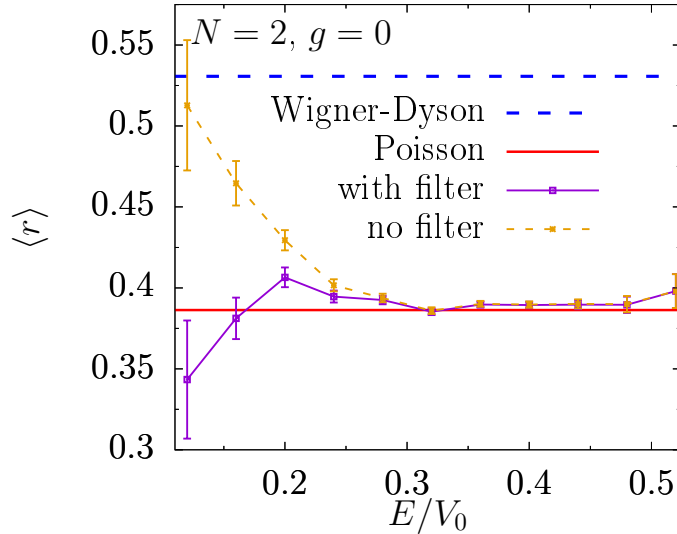$$|E_2\rangle = |N - 1, 0, 1, 0..., 0\rangle,$$

Figure 5.4: Mean value of r as a function of E/V_0 distributed in energy computed with and without a randomness filter for the noninteracting two-boson system. The filter removes the values $r_i \geqslant 0.999$.

and their associated energies are

$$E_0 = NE_{GS},$$
$$E_1 = NE_{GS} + \Delta_1, \tag{5.15}$$
$$E_2 = NE_{GS} + \Delta_2.$$

Therefore, we have

$$r_1 = \frac{E_2 - E_1}{E_1 - E_0} = \frac{\Delta_2 - \Delta_1}{\Delta_1}. \tag{5.16}$$

This is a random variable which depends on the level spacings, and one expects it to follow the Poisson (or eventually the Wigner-Dyson) distribution.

If the data emerging from both scenarios are included in the ensemble average, one obtains, in the low-energy regime, $\langle r \rangle$ values with an upward bias, therefore deviating from the Poisson statistics even in setups where the single-particle modes are localized on a short length-scale. This effect, displayed in Fig. 5.4, for the representative setup with $N = 2$, $L = 100\ell/\sqrt{2}$ and $V_0 = 50E_c$, should not be associated to a delocalization phenomenon. For this reason, in our calculations with $N > 1$ noninteracting particles we introduce a filter that removes the r_i values which are numerically indistinguishable from $r_i = 1$, i.e. the data corresponding to the first scenario described above. With this filter, the ensemble-averaged $\langle r \rangle$ values agree with the Poisson distribution result within statistical uncertainties (see Fig. 5.4). As expected, the filter has no effect at moderate to high energies. It is worth emphasizing that this effect occurs only for noninteracting particles. As soon as

$g > 0$, the many-body state is a superposition of many basis states; so, the two scenarios described above do not apply, and the r_i values randomly fluctuate for different speckle field realizations.

5.3   Localization in the repulsively interacting two- and three-boson systems

We start the discussion on the interacting few-boson setup with a qualitative analysis of the interaction effect on the ground-state energy. Specifically, we consider $N = 2$ bosons in a speckle field of intensity $V_0 = 50E_c$, in a $L = 100\ell/\sqrt{2}$ box. As discussed in the previous section, in this setup the single-particle modes are spatially localized in a broad energy-range $0 < E \lesssim 2V_0$.

In the noninteracting limit, the ground state is the Fock-basis state $|2, 0, ..., 0\rangle$, and the corresponding energy equals two times the single-particle ground-state energy. In the first excited state, one boson is promoted to the first single-particle excited state, obtaining the Fock-basis state $|1, 1, ..., 0\rangle$. The energy levels corresponding to the ground state and to the first excited state of a speckle field instance are displayed in Fig. 5.5, as a function of the interaction parameter g. One notices that, while the ground-state energy increases with g, the first excited-state energy is essentially unaltered. This is due to the fact that in the excited state the two bosons are localized in far apart wells; therefore, the zero-range interaction has an almost negligible effect. In the strongly interacting limit, $g \to \infty$, the lowest-energy state is $|1, 1, ..., 0\rangle$. This scenario is similar to the Tonks-Girardeau gas, where bosons with infinitely-strong zero-range repulsive interaction can be mapped to a system of noninteracting indistinguishable fermions, which occupy different single-particle modes due to the Pauli exclusion principle. Remarkably, the transition between the noninteracting and the strongly-interacting regimes is extremely sharp. This effect is due to the long separation between the two lowest-energy minima for this realization of the speckle potential. For the speckle field instance analyzed in Fig. 5.5, this sharp crossover occurs at $g \approx 2.8$. Beyond this pseudo-critical point the two-boson system is effectively fermionized, meaning that their ground-state energy essentially coincides with the one of two identical fermions in the same setup. Remarkably, this fermionization occurs at strong but finite values of the interaction parameter g, as opposed to homogeneous systems where bosons fermionize only in the $g \to \infty$ limit, which corresponds to the standard Tonks-Girardeau gas. Note that in the speckle instances in which the ground and first excited single particle states are localized in the same minima, the fermionization would be smoother, in line with, e.g. fermionization in a harmonic potential [155].

For different speckle field instances, this fermionization transition occurs at different values of the coupling parameter g. Also the energy levels in the noninteracting limit and in the strongly-interacting limit, as well as in the crossover region, randomly fluctuate. In Fig. 5.6, the average over many realizations of the speckle field of the two-boson ground-state energy is plotted as a
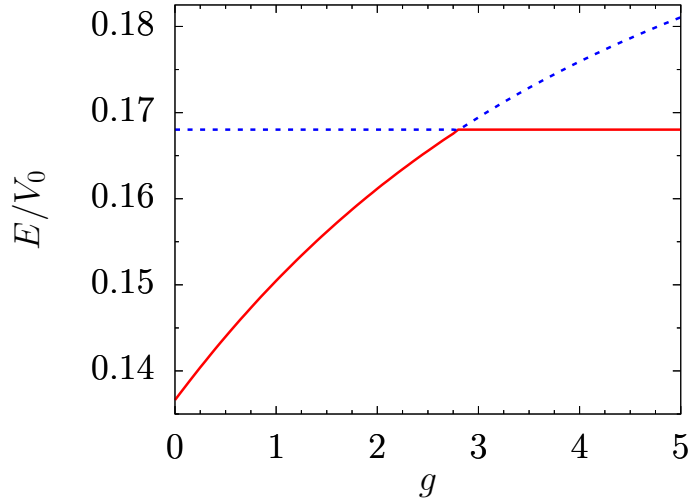
Figure 5.5: Energies of the ground state (red solid line) and first excited state (blue short-dashed line) of the system of $N = 2$ bosons in the speckle potential of Fig. 5.1, panel (b), as a function of the interaction strength g. This figure is obtained with $M = 636$, which results in a $D_{MB} = 159069$ for an $E_{\max} = 400$.
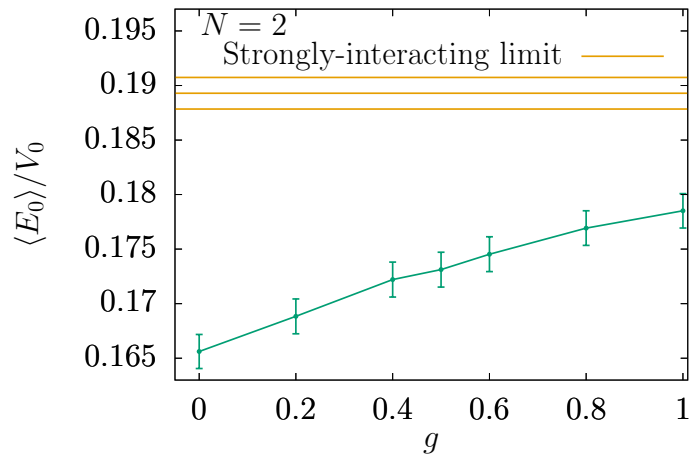

Figure 5.6: Mean value of the ground state energy averaged over $N_s = 985$ different speckle potentials as a function of the interaction strength g for the two-boson system. The error bars are computed as the standard deviation, $\sigma_{E_0} = \sqrt{\frac{\langle E_0^2 \rangle - \langle E_0 \rangle^2}{N_s}}$. The speckle realisations used to produce this plot are the same as those used in Fig. 5.8.

function of the interaction parameter g. Here, we consider interaction strengths ranging from the noninteracting limit to the moderately large interaction parameter $g = 1$. One notices that this interaction strength is sufficient to shift the ground-state energy away from the noninteracting-
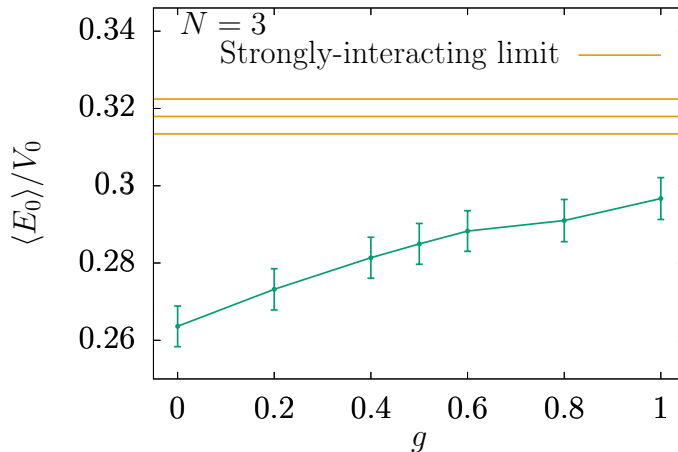
Figure 5.7: Mean value of the ground state energy averaged over $N_s = 250$ different speckle potentials depending on the interaction strength g for the three-boson system. The error bars are computed as the standard deviation, $\sigma_{E_0} = \sqrt{\frac{\langle E_0^2 \rangle - \langle E_0 \rangle^2}{N_s}}$. The speckle realisations used to produce this plot are the same as those used in Fig. 5.9.

limit result, reaching values in fact closer to the strongly-interacting limit — where the energy of a noninteracting identical fermions is reached — than to the noninteracting limit.

The same scenario occurs for the $N = 3$ boson system, which is analyzed in Fig 5.7. In the following, we focus on the interaction regime $0 \leqslant g \leqslant 1$, where any interesting interaction effect would take place. Stronger interactions require extremely large basis-set sizes, so that it is not computationally feasible for us to perform averages of many realizations of the speckle field. This regime of intermediate interaction strength $g \approx 1$ is, in fact, the one where one expects to have more pronounced delocalization effects. Indeed, in the strongly-interacting limit the system properties are again determined by the single-particle modes. Since the latter are localized for the disorder strength considered here, one expects the many-body system to be localized, too. This type of re-entrant behavior has been observed in the cold-atom experiments on many-body localization [60]. The experimentalists indeed found that in the strongly-interacting limit the system is many-body localized if the corresponding noninteracting system is localized. The experiment was performed with fermions with two spin states. In this case, in the strongly-interacting limit the system properties can be mapped to those of a fully polarized (noninteracting) Fermi gas, in analogy with the Tonks-Girardeau physics in Bose gases.

The analysis of the level-spacings statistics for the interacting two-boson system is displayed in Fig. 5.8. Specifically, we plot the disorder-averaged $\langle r \rangle$ values as a function of E/V_0, for different values of the interaction parameter g. The disorder strength V_0 and the linear system size L are the ones discussed above and in the previous section. We focus on the low-energy regime $E \lesssim V_0$.

Accurately computing more energy levels for many speckle-field instances, in particular, at high energies where larger basis sets are required, exceeds our computational resources.

For the computations of Fig. 5.8 the basis sets includes 23836 states, namely the ones with a kinetic energy less or equal to $E_{max} = 60E_c$; this corresponds to employing $M = 246$ single-particle modes. The disorder ensemble includes 985 realizations of the speckle field.

It is clear that the $\langle r \rangle$ values are always consistent with the prediction corresponding to the Poisson distribution of the level spacings, which is associated to nonergodic systems. The statistical uncertainty is larger in the $E \to 0$ limit due to the low density of states in the low energy regime, which reduces the available statistics. The agreement with the Poisson distribution implies that, for the range of coupling constant considered here, the zero-range interaction does not induce delocalization of the two-boson system. It is possible that a two-body mobility edge, separating low-energy localized states from high-energy extended states, would occur at higher energies. However, addressing higher energies requires larger computational resources and it is beyond the scope of the present Chapter.

The results for the $N = 3$ bosons systems are shown in Fig. 5.9. Here, the basis-set size is 117977, corresponding to the Fock basis states with a kinetic energy less or equal to $E_{max} = 12E_c$, in turn implying the use of $M = 110$ single-particle modes. The disorder-ensemble includes 250 realizations of the speckle field. We observe that also in the three-boson system localization is, in the low energy regime and for the coupling parameters considered here, stable against the effect of zero-range interactions.
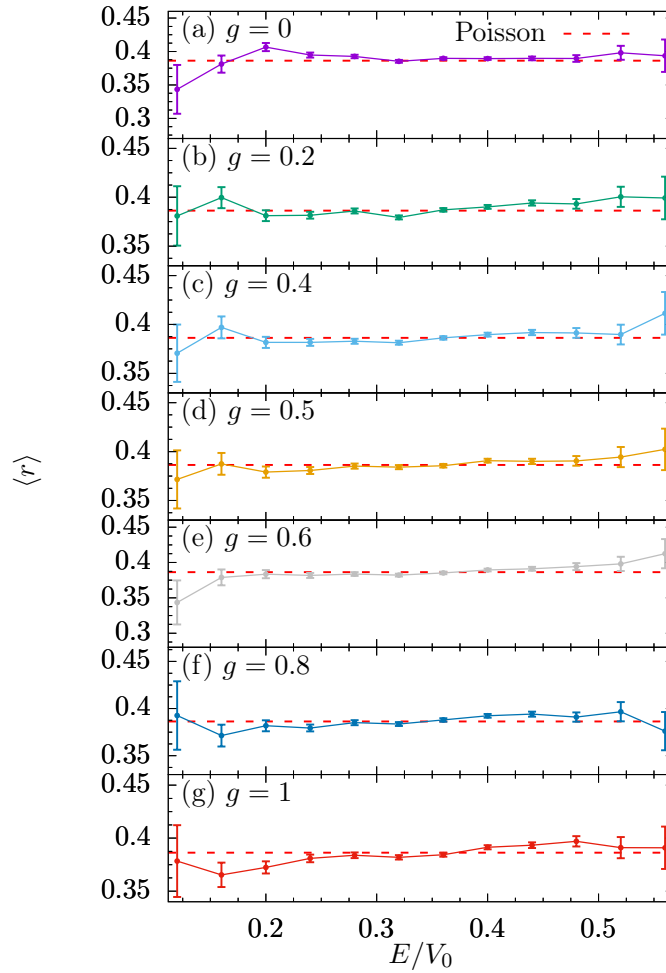
Figure 5.8: Distribution in energy of $\langle r \rangle$ for $N = 2$ bosons in a 1D box with a speckle potential. The numerical results with different interaction strengths g, of a contact potential, are compared with the theoretical value that correspond to a Poisson distribution of the energy gaps.
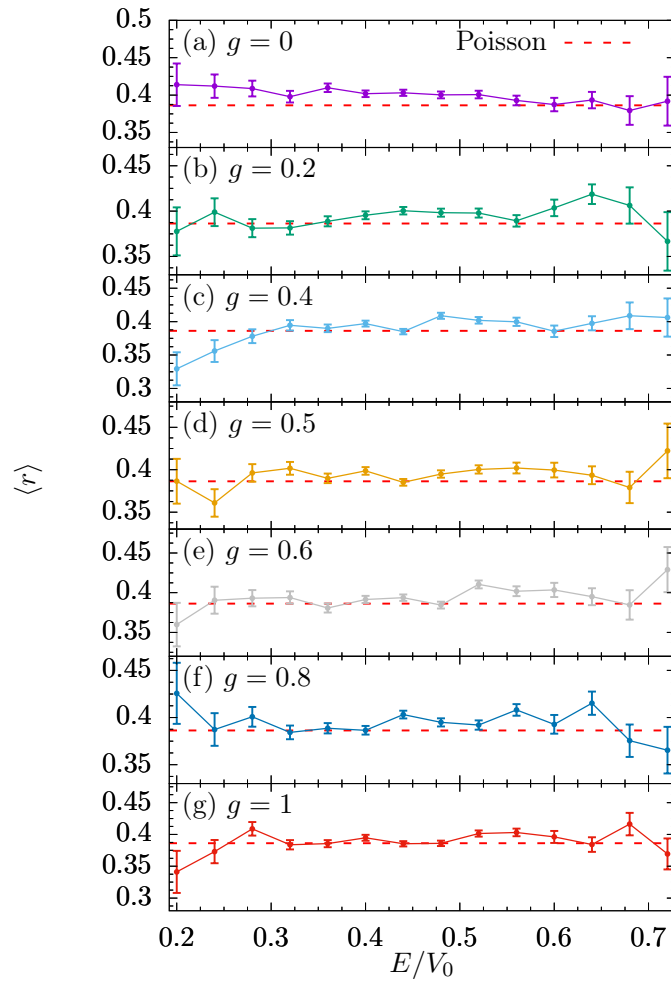
Figure 5.9: Distribution in energy of $\langle r \rangle$ for $N = 3$ bosons in a 1D box with a speckle potential for different interaction strengths. The numerical results are compared with the theoretical predictions corresponding to a Poisson distribution of the energy gaps.

Chapter 6

SPIN-ORBIT COUPLING EFFECTS IN A TWO-DIMENSIONAL HARMONIC TRAP

In this Chapter, as in Chapters 3 and 4, we study a two-dimensional system of bosons in a harmonic trap. Additionally, in this case, the bosons have an extra degree of freedom, they can be in two different pseudospin states. Moreover, we include a Rashba-type spin-orbit coupling which acts on this extra degree of freedom at the single-particle level. The objective is to explore the combined effects of the interaction and the spin-orbit coupling in the system. The first step is to understand how the eigenstates of the single-particle system change with the spin-orbit coupling strength and after to study the two-boson system in several physical situations.

The Chapter is organized as follows. In Sec. 6.1, the ground state of the single-particle system and the first low-energy states are computed and analyzed. We relate the different energy contributions and also the expectation values of different kind of spin-orbit coupling terms by applying the virial theorem. In Sec. 6.2, we study the interacting two-boson system. First, we give the general second-quantized N-boson Hamiltonian and after we diagonalize it for the $N = 2$ case. In second place, we discuss the degeneracy breaking of the ground state. In Sec. 6.3, we analyze the combined effects of the spin-orbit coupling and a spin-independent repulsive interaction in the spectrum. In particular, when we vary the spin-orbit coupling strength, we find a crossover in the ground state characterized by a discontinuity in the energy contributions and a change in the density profiles of the system.

6.1   The single-particle system

The physics of a particle of mass m in a two-dimensional isotropic harmonic potential of frequency ω with Rashba type spin-orbit coupling is described by the Hamiltonian

$$\hat{H}_{\mathrm{sp}} = \frac{1}{2}m\omega^2\left(\hat{x}^2 + \hat{y}^2\right) + \frac{\hat{p}_x^2 + \hat{p}_y^2}{2m} + \frac{\kappa^2}{2m} + \frac{\kappa}{m}\left(\hat{\sigma}_x\hat{p}_x + \hat{\sigma}_y\hat{p}_y\right), \tag{6.1}$$

where κ is the spin-orbit coupling constant and $\hat{\sigma}_x$ and $\hat{\sigma}_y$ are Pauli matrices. As we consider a bosonic system of ultracold spin-0 atoms, the spin part does not refer to the intrinsic spin but to an internal degree of freedom or pseudospin, for instance, two hyperfine atomic states as in Ref. [73]. The Hamiltonian is composed by the kinetic energy, $\hat{K} = (\hat{p}_x^2 + \hat{p}_y^2)/(2m)$, the harmonic potential, $\hat{V}_{\mathrm{ho}} = (m/2)\omega^2\left(\hat{x}^2 + \hat{y}^2\right)$, the spin-orbit coupling, $\hat{V}_{\mathrm{so}} = (\kappa/m)\left(\hat{\sigma}_x\hat{p}_x + \hat{\sigma}_y\hat{p}_y\right)$, and the constant term $\kappa^2/(2m)$. As mentioned in Ref. [99], up to a pseudospin rotation, an alternative and equivalent form of the Rashba term would be $\propto (\hat{\sigma}_x\hat{p}_y - \hat{\sigma}_y\hat{p}_x)$.

From now on, we use harmonic oscillator units, i.e., the energy is measured in units of $\hbar\omega$ and the length in units of $\sqrt{\hbar/(m\omega)}$. The Hamiltonian in Eq. (6.1) is written in terms of annihilation operators, $\hat{a}_x = (\hat{x} + i\hat{p}_x)/\sqrt{2}$ and $\hat{a}_y = (\hat{y} + i\hat{p}_y)/\sqrt{2}$, and the corresponding creation operators, $\hat{a}_x^\dagger$ and $\hat{a}_y^\dagger$, as

$$\hat{H}_{\mathrm{sp}} = \hat{n}_x + \hat{n}_y + 1 + \frac{i\kappa}{\sqrt{2}}\left[\hat{\sigma}_x\left(\hat{a}_x^\dagger - \hat{a}_x\right) + \hat{\sigma}_y\left(\hat{a}_y^\dagger - \hat{a}_y\right)\right] + \frac{\kappa^2}{2}. \tag{6.2}$$

These operators fulfill the commutation relations $[\hat{a}_i, \hat{a}_j^\dagger] = \delta_{ij}$ and $[\hat{a}_i, \hat{a}_j] = [\hat{a}_i^\dagger, \hat{a}_j^\dagger] = 0$, with $i, j = x, y$. We have used the operators $\hat{n}_x = \hat{a}_x^\dagger\hat{a}_x$ and $\hat{n}_y = \hat{a}_y^\dagger\hat{a}_y$, which account for the number of quantum excitations. Notice that κ is not a dimensionless parameter in the original Hamiltonian, Eq. (6.1), and it is written in units of $\sqrt{\hbar m\omega}$ in Eq. (6.2).

The single-particle basis can be labeled as, $\{|n_x, n_y, m_s\rangle\}$, with $n_x, n_y = 0, 1, 2, \ldots$, and $m_s = -1, 1$, where n_x, n_y and m_s are eigenvalues of $\hat{n}_x$, $\hat{n}_y$ and $\hat{\sigma}_z$, respectively. The matrix elements of the single-particle Hamiltonian using this basis read

$$\langle i|\hat{H}_{\mathrm{sp}}|j\rangle = \epsilon_{ij} + \frac{\kappa^2}{2}\delta_{i,j}, \tag{6.3}$$

with

$$
\begin{aligned}
\epsilon_{ij} = {} & \left(n_x(i) + n_y(i) + 1\right)\delta_{i,j} \\
& + \frac{i\kappa}{\sqrt{2}}\delta_{m_s(i),-m_s(j)}\Big(\sqrt{n_x(j)+1}\,\delta_{n_x(i),n_x(j)+1}\,\delta_{n_y(i),n_y(j)} - \sqrt{n_x(j)}\,\delta_{n_x(i),n_x(j)-1}\,\delta_{n_y(i),n_y(j)} \\
& + i\,m_s(j)\sqrt{n_y(j)+1}\,\delta_{n_x(i),n_x(j)}\,\delta_{n_y(i),n_y(j)+1} - i\,m_s(j)\sqrt{n_y(j)}\,\delta_{n_x(i),n_x(j)}\,\delta_{n_y(i),n_y(j)-1}\Big)
\end{aligned} \tag{6.4}
$$

and $|i\rangle \equiv |n_x(i), n_y(i), m_s(i)\rangle$. The index i labels each state of the single-particle basis. The Hamiltonian matrix is fully diagonalized using the first 5112 states in order of increasing energy ϵ_{ii},
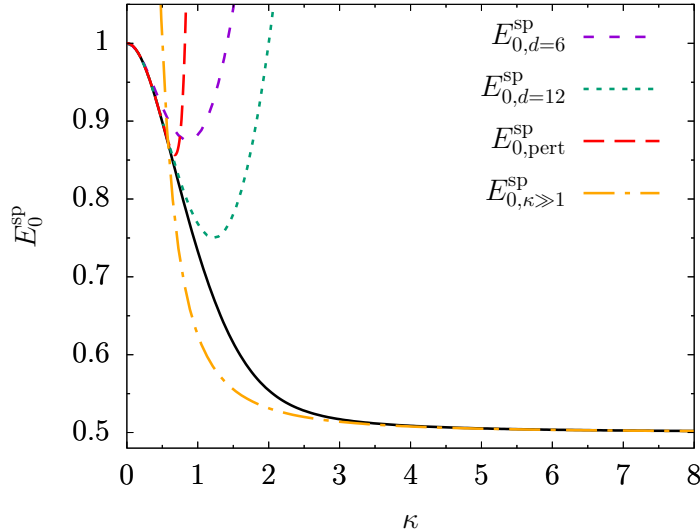
Figure 6.1: Solid black line: Single-particle ground state energy, E_0^{sp}, of the single-particle Hamiltonian in (6.2) computed by numerical diagonalization. Medium-dashed purple line: $E_{0,d=6}^{\mathrm{sp}}$ given in Eq. (6.5). Short-dashed green line: $E_{0,d=12}^{\mathrm{sp}}$ given in Eq. (6.6). Long-dashed red line: Perturbative energy from Ref. [97], $E_{0,\mathrm{pert}}^{\mathrm{sp}}$, given in Eq. (6.7). Dashed-dotted orange line: Limit value for $\kappa \gg 1$, $E_{0,\kappa\gg1}^{\mathrm{sp}}$, from Ref. [87], given in Eq. (6.8).

which corresponds to $(n_x + n_y) \leqslant 70$ and $m_s = -1, 1$. In this truncated Hilbert space, the energies obtained are upper bounds to the exact ones. The method is variational, since we diagonalize in a subspace of the full Hilbert space.

6.1.1 The single-particle ground-state

In this section, we explore the transition from the weak spin-orbit coupling regime, $\kappa < 1$, to the strong spin-orbit coupling one, $\kappa \gg 1$, at the single-particle level. Our diagonalization results are compared with previously derived analytical expressions valid for the $k \gg 1$ limit in Ref. [87], with perturbation theory expressions, $k \ll 1$, derived in Ref. [97], and with our own truncated analytic predictions valid in the $k \lesssim 1$ regime.

In Fig. 6.1 we report the single-particle ground-state energy as a function of κ. The ground state is in all cases two-fold degenerated. For $\kappa = 0$, we recover the harmonic oscillator result, $E_0^{\mathrm{sp}} = 1$. As κ is increased, the ground-state energy decreases towards an almost constant value of $E_0^{\mathrm{sp}} \simeq 0.5$, which is already reached for $\kappa \simeq 3$.

For $\kappa < 1$, we derive analytical approximate expressions for the ground state of the single-particle Hamiltonian and its energy. The variational method consists in truncating the Hilbert space to a small number of modes (see Appendix D.1 for details). Analytic expressions can be

obtained truncating to six or twelve modes,

$$E^{\text{sp}}_{0,d=6} = \frac{1}{2}\left(3 - \sqrt{4\kappa^2 + 1}\right) + \frac{\kappa^2}{2}, \tag{6.5}$$

$$E^{\text{sp}}_{0,d=12} = 2 - \sqrt{2\kappa^2 + 1} + \frac{\kappa^2}{2}. \tag{6.6}$$

The goodness of these expressions is shown in Fig. 6.1, comparing them with the direct diagonalization and also with the perturbative calculations performed in Ref. [97], that we write in our units as:

$$E^{\text{sp}}_{0,\text{pert}} = 1 - \frac{1}{2}\kappa^2 + \frac{1}{2}\kappa^4 - \frac{2}{3}\kappa^6 + \frac{79}{72}\kappa^8 - \frac{274}{135}\kappa^{10} + \frac{130577}{32400}\kappa^{12}. \tag{6.7}$$

Eq. (6.6) is the best approximation to the full diagonalization results, providing an accurate description up to $\kappa = 1$. The perturbative expression of Ref. [97], Eq. (6.7), reproduces well the results up to $\kappa \simeq 0.7$ while the approximation with six modes already fails for $\kappa \simeq 0.5$.

The large κ domain has been studied previously in Refs. [87–91]. In this regime, approximate expressions for the two-degenerate states that define the ground-state subspace are given in Ref. [87], together with an expression for the ground-state energy,

$$E^{\text{sp}}_{0,\kappa \gg 1} = \frac{1}{2} + \frac{1}{8\kappa^2}. \tag{6.8}$$

This approximation is in very good agreement with our numerical results for $\kappa > 2$ (see Fig. 6.1). In particular, they correctly capture the limiting value in the spin-orbit dominated regime, $E^{\text{sp}}_0 \to 1/2$.

6.1.2   The single-particle energy spectrum

One of the important advantages of direct diagonalization methods is that they also provide, besides the ground state properties, the low-energy part of the spectrum. The low-energy spectrum of the single-particle Hamiltonian, Eq. (6.2), is depicted in Fig. 6.2.

In the limiting case of $\kappa = 0$, the eigenstates of the Hamiltonian are the eigenstates of two independent two-dimensional harmonic oscillators, one for each spin component. Therefore, the energies are $E^{\text{sp}}_n = n + 1$ with degeneracy $2(n+1)$ and $n = n_x + n_y$. The case of $\kappa < 1$ is analyzed in Ref. [97], where the exact numerical values are compared with perturbation theory calculations in κ.

For any value of κ, all energy levels are two-fold Kramers-degenerate because the Hamiltonian is time-reversal symmetric [88,89,91,92,95]. This degeneracy can be broken by introducing a Zeeman term [92]. The effect of deforming the trap was considered in Ref. [93], that results in a breaking of the cylindrical symmetry of the system. In our case, the time-reversal symmetry is preserved and, in order to distinguish between the pair of degenerate states, we label them with A and B, respectively, for a given energy E^{sp}. The action of the time reversal operator, $\hat{T} = i\hat{\sigma}_y \mathcal{C}$ [88,89,92,95], with $\mathcal{C}$
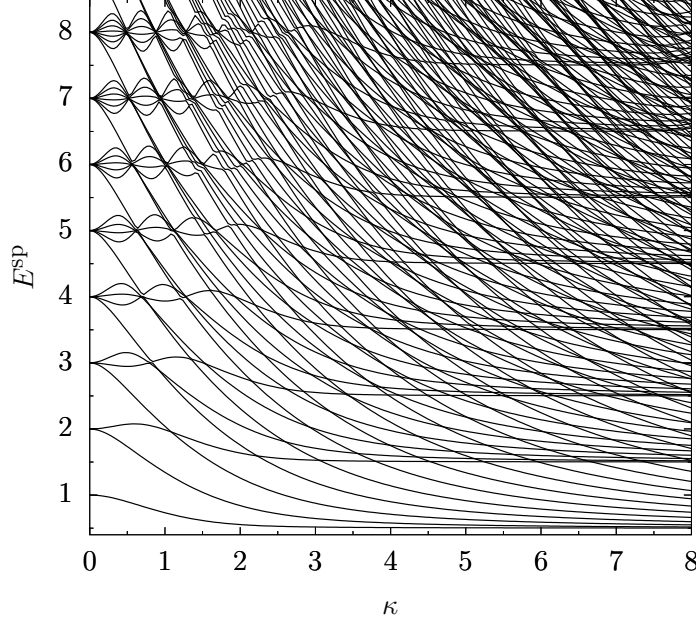
Figure 6.2: Energy spectrum of the single-particle Hamiltonian in Eq. (6.2) depending on the spin-orbit coupling constant κ. Notice that each energy is doubly degenerate so each line in the plot represents two equal energies that can be associated to two orthogonal eigenstates. This energy spectrum is also shown in the left panel of Fig. 1 of Ref. [92] up to $\kappa \approx 1$ and energies up to 20, and in Fig. 3 of Ref. [97] for the lowest-energy eigenstates. The three-dimensional analogous spectrum is presented in Fig. 1 of Ref. [90].

the complex conjugation operator, on the two-fold degenerate eigenstates reads

$$
\begin{aligned}
|\psi_{E,B}^{\mathrm{sp}}\rangle &= \imath\,\hat{\sigma}_y \mathcal{C}\,|\psi_{E,A}^{\mathrm{sp}}\rangle\ , \\
|\psi_{E,A}^{\mathrm{sp}}\rangle &= \imath\,\hat{\sigma}_y \mathcal{C}\,|\psi_{E,B}^{\mathrm{sp}}\rangle\ .
\end{aligned}
\tag{6.9}
$$

The eigenstates of the single-particle Hamiltonian can be written in a basis with a well defined total angular momentum,

$$
\hat{\boldsymbol{J}} = \hat{\boldsymbol{S}} + \hat{\boldsymbol{L}},
\tag{6.10}
$$

where $\hat{\boldsymbol{S}} = (\hat{\sigma}_x, \hat{\sigma}_y, \hat{\sigma}_z)/2$, and $\hat{\boldsymbol{L}} \equiv \hat{\boldsymbol{r}} \times \hat{\boldsymbol{p}} = (0, 0, \hat{L}_z)$. The single-particle Hamiltonian commutes with $\hat{J}^2$ and $\hat{J}_z$. Therefore, the eigenstates of the system can be labeled with the corresponding quantum numbers, j and j_z, respectively, regardless of the value of κ. In particular, in the limiting case $\kappa \gg 1$, an additional radial quantum number, n_r, is introduced to describe the eigenstates of the system (see Ref. [87]) and also the eigenenergies, approximately,

$$
E_{\kappa \gg 1}^{\mathrm{sp}} = n_r + \frac{1}{2} + \frac{j_z^2}{2\kappa^2},
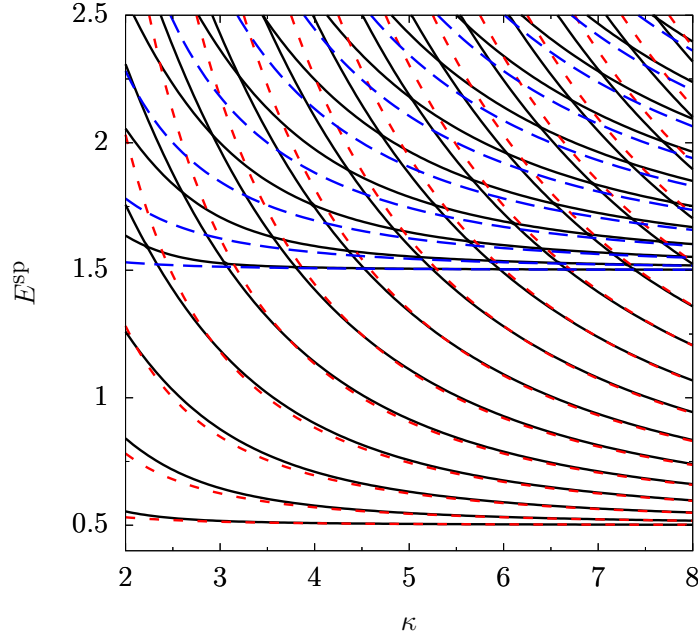\tag{6.11}
$$

Figure 6.3: Solid black lines: Lowest eigenenergies of the single-particle Hamiltonian in Eq. (6.2) computed by diagonalization. Short-dashed red lines: Approximate energy levels computed with Eq. (6.11) and $n_r = 0$. Long-dashed blue lines: Approximate energy levels computed with Eq. (6.11) and $n_r = 1$. Notice that each energy level is doubly degenerate and within each kind of lines the energy increases by increasing j_z^2.

with $n_r = 0, 1, \ldots$, and $j_z = m_l + 1/2$, with $m_l = 0, \pm 1, \ldots$. The two-fold degeneracy is reflected in the fact that the energy depends on j_z^2, so it is independent of its sign. The eigenstates with the same radial quantum number, n_r, tend to become degenerate with increasing κ, forming an energy manifold. This kind of physics has been studied in two and three dimensions, where the same type of Landau-level-like spectrum is found and described in terms of dimensional reduction [87–91].

The approximate expression, Eq. (6.11), works very well for $\kappa \gg 1$, as seen in Fig. 6.3. For a given value of κ, the lowest eigenenergies are well-described and, as expected, the larger is the value of κ the better is the approximation for a larger number of energy levels.

6.1.3   Energy contributions

As it has been shown previously, by increasing κ, the system goes from a harmonic oscillator behavior to a spin-orbit dominated one. The spectral properties are very different in both limits and feature a particularly involved structure in the intermediate region. To better understand the spin-orbit effects, we consider now the different energy contributions to the total energy of the different eigenstates as we vary the value of κ.

In Fig. 6.4, we show, for the first eigenstates of the single-particle system, how the total energy is distributed between the different energy contributions. As can be seen, the degeneracy due to the time-reversal symmetry of the system, that makes all eigenstates two-fold degenerate, is also reflected in the energy contributions. Each pair of degenerate states has also the same kinetic, harmonic potential, and spin-orbit coupling energies.

In the $\kappa = 0$ limit, the eigenstates obey the equipartition relation valid for the harmonic oscillator, $\langle K \rangle = \langle V_{\mathrm{ho}} \rangle$ [see Fig. 6.4 panel (a)]. For a sufficiently small value of the spin-orbit coupling constant, those two contributions are not equal but of the same order of magnitude [see panels (b) and (c) of Fig. 6.4 for the cases $\kappa = 0.5$ and $\kappa = 1$, respectively]. Further increasing the value of κ, the situation changes, and the largest contributions, in absolute value, to the total energy are clearly the spin-orbit and kinetic parts [see Fig. 6.4 panel (d)]. There are, however, large cancellations between these two contributions which result in a total energy comparable to the harmonic oscillator part. Further insights into this energy decomposition and a nontrivial test to our numerical method is provided by the virial theorem (see Appendix E),

$$2 \langle \psi_E^{\mathrm{sp}} | \hat{V}_{\mathrm{ho}} | \psi_E^{\mathrm{sp}} \rangle - 2 \langle \psi_E^{\mathrm{sp}} | \hat{K} | \psi_E^{\mathrm{sp}} \rangle - \langle \psi_E^{\mathrm{sp}} | \hat{V}_{\mathrm{so}} | \psi_E^{\mathrm{sp}} \rangle = 0 \,. \tag{6.12}$$

For all the states considered, we have checked that the virial theorem energy relation is fulfilled, i.e., the left part of Eq. (6.12) represents less than 1% of E^{sp}. Actually, the cancellation needed comes from $\langle K \rangle$ and $\langle V_{\mathrm{ho}} \rangle$ for $\kappa = 0$ and from $\langle K \rangle$ and $\langle V_{\mathrm{so}} \rangle$ in the large κ domain.

6.1.4 Expectation value of the spin-orbit potential

The term that commonly appears in atomic and nuclear physics as spin-orbit coupling is proportional to $\hat{L}_z \hat{\sigma}_z$. The main difference between that kind of term and the Rashba spin-orbit is that in one case the spin is coupled to the angular momentum and in the other to the linear momentum. However, we can relate the expectation values of both types of spin-orbit coupling terms,

$$\langle \psi_E^{\mathrm{sp}} | \hat{V}_{\mathrm{so}} | \psi_E^{\mathrm{sp}} \rangle = -2\kappa^2 \left(1 + \langle \psi_E^{\mathrm{sp}} | \hat{L}_z \hat{\sigma}_z | \psi_E^{\mathrm{sp}} \rangle \right). \tag{6.13}$$

The eigenstates of the single-particle system obtained by exact diagonalization, whose energies are shown in Fig. 6.4, fulfill the previous relation, within a numerical error of less than a 1% in the difference between both sides of Eq. (6.13).

The relation between the expectation values of the two kinds of spin-orbit terms is not a particularity of the pure Rashba case, it also works in a more general case, i.e. a mixture of Rashba and Dresselhaus spin-orbit couplings. Moreover, this property does not depend on the external trapping potential. The derivation of the relation in Eq. (6.13) is presented in Appendix E, where we also generalize it and demonstrate its independence of the external trap.
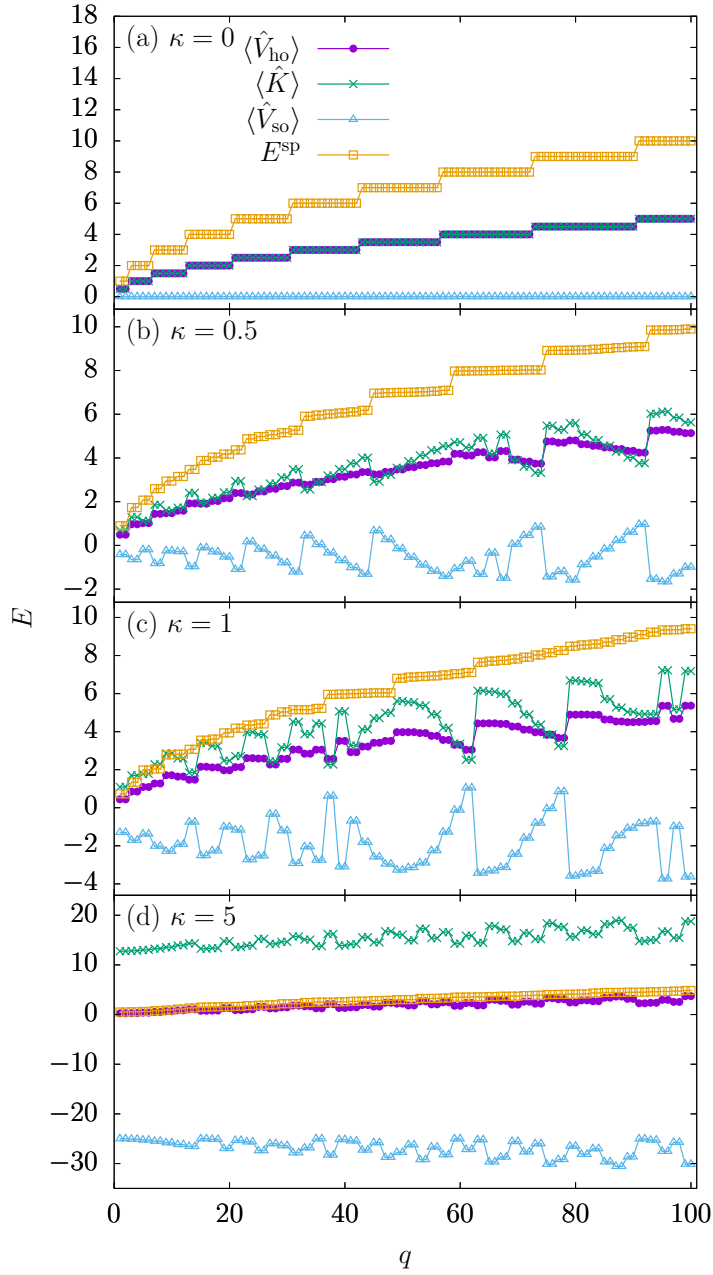
Figure 6.4: Energy contributions to the eigenenergies, $E^{\mathrm{sp}} = \langle \hat{K} \rangle + \langle \hat{V}_{\mathrm{so}} \rangle + \langle \hat{V}_{\mathrm{ho}} \rangle + \frac{\kappa^2}{2}$, for the first 100 eigenstates of the Hamiltonian in Eq. (6.2), labeled with $q = 1, \ldots, 100$. The spin-orbit coupling constant, κ, increases going from panel (a) to panel (d). Notice that each panel of this figure corresponds to a vertical cut in Fig. 6.2. In panel (a), $\langle \hat{K} \rangle$ and $\langle \hat{V}_{\mathrm{ho}} \rangle$ coincide.

6.2   The two-boson system

In this section, we turn to the interacting few-body system. We first present our formalism which is developed for the general case of N interacting bosons. Afterwards, we concentrate on the two-boson case.

Let us thus start with a system of N interacting identical bosons trapped by an isotropic harmonic potential with Rashba spin-orbit coupling. The N-boson Hamiltonian reads

$$\hat{H} = \hat{H}_0 + \hat{H}_{\text{int}} + \frac{N\kappa^2}{2}. \tag{6.14}$$

The first part contains the total harmonic potential energy, $\hat{V}_{\text{ho}}^T$, kinetic energy, $\hat{K}^T$, and spin-orbit energy, $\hat{V}_{\text{so}}^T$,

$$\hat{H}_0 = \hat{V}_{\text{ho}}^T + \hat{K}^T + \hat{V}_{\text{so}}^T, \tag{6.15}$$

with $\hat{V}_{\text{ho}}^T = (1/2)\sum_{i=1}^N \hat{\boldsymbol{x}}_i^2$, $\hat{K}^T = (1/2)\sum_{i=1}^N \hat{\boldsymbol{p}}_i^2$, and $\hat{V}_{\text{so}}^T = \kappa \sum_{i=1}^N (\hat{\sigma}_{x_i} \hat{p}_{x_i} + \hat{\sigma}_{y_i} \hat{p}_{y_i})$.

We model the atom-atom interaction with the Gaussian potential introduced in Sec. 3.2 characterized by a finite range s independent of the spin state and, in the present case, an interaction strength that can vary depending on the spin [97]. In this way, the interaction part is separated in three contributions,

$$\hat{H}_{\text{int}} = \hat{H}_{\uparrow\uparrow} + \hat{H}_{\downarrow\downarrow} + \hat{H}_{\uparrow\downarrow}, \tag{6.16}$$

where,

$$
\begin{aligned}
\hat{H}_{\uparrow\uparrow} &= \sum_{i<j}^N \frac{g_{\uparrow\uparrow}}{\pi s^2} e^{-\frac{(\hat{\boldsymbol{x}}_i - \hat{\boldsymbol{x}}_j)^2}{s^2}} |\uparrow\rangle_i |\uparrow\rangle_j \langle\uparrow|_i \langle\uparrow|_j, \\
\hat{H}_{\downarrow\downarrow} &= \sum_{i<j}^N \frac{g_{\downarrow\downarrow}}{\pi s^2} e^{-\frac{(\hat{\boldsymbol{x}}_i - \hat{\boldsymbol{x}}_j)^2}{s^2}} |\downarrow\rangle_i |\downarrow\rangle_j \langle\downarrow|_i \langle\downarrow|_j, \\
\hat{H}_{\uparrow\downarrow} &= \sum_{i<j}^N \frac{g_{\uparrow\downarrow}}{\pi s^2} e^{-\frac{(\hat{\boldsymbol{x}}_i - \hat{\boldsymbol{x}}_j)^2}{s^2}} \left(|\uparrow\rangle_i |\downarrow\rangle_j \langle\uparrow|_i \langle\downarrow|_j + |\downarrow\rangle_i |\uparrow\rangle_j \langle\downarrow|_i \langle\uparrow|_j \right).
\end{aligned} \tag{6.17}
$$

For simplicity, we have introduced the following notation for the spin variable: $|\uparrow\rangle \equiv |m_s = 1\rangle$, and $|\downarrow\rangle \equiv |m_s = -1\rangle$.

6.2.1   Second-quantized two-boson Hamiltonian

Despite the fact that our approach is in principle valid for a few number of bosons, we concentrate from now on in the two-boson case. The two-boson system provides a nontrivial example where the interplay of interactions and spin-orbit coupling can be studied in detail.

The particles can populate the first M eigenstates of the harmonic trap, including the spin degree of freedom. Consequently, the creation and annihilation operators, $\hat{a}_i^\dagger$ and $\hat{a}_i$, create or annihilate bosons, respectively, in the single-particle state $|i\rangle$, with $i = 1, ..., M$, where the index i

labels the trio of quantum numbers n_x, n_y and m_s, and increases with increasing the energy of the harmonic oscillator eigenstate i, which is $\epsilon_{ii} = n_x(i) + n_y(i) + 1$. The dimension of the truncated two-boson Hilbert space and the number of single-particle modes required where given in Sec. 2.5.2.

The second-quantized version of the single-particle part of Eq. (6.14) is

$$\hat{H}_0 = \sum_{i,j=1}^{M} \epsilon_{ij}\, \hat{a}_i^\dagger \hat{a}_j, \tag{6.18}$$

where the explicit form of ϵ_{ij} is given in Eq. (6.4). The interaction term is written as:

$$
\begin{aligned}
\hat{H}_{\text{int}} &= \frac{1}{2} \sum_{i,j,k,l=1}^{M} \hat{a}_i^\dagger \hat{a}_j^\dagger \hat{a}_k \hat{a}_l\, V_{ijkl} \\
&\times \Big\{ g_{\uparrow\uparrow} \delta_{m_s(i),1}\delta_{m_s(j),1}\delta_{m_s(k),1}\delta_{m_s(l),1} + g_{\downarrow\downarrow}\delta_{m_s(i),-1}\delta_{m_s(j),-1}\delta_{m_s(k),-1}\delta_{m_s(l),-1} \\
&+ g_{\uparrow\downarrow}\Big(\delta_{m_s(i),1}\delta_{m_s(j),-1}\delta_{m_s(k),1}\delta_{m_s(l),-1} + \delta_{m_s(i),-1}\delta_{m_s(j),1}\delta_{m_s(k),-1}\delta_{m_s(l),1}\Big) \Big\},
\end{aligned} \tag{6.19}
$$

where V_{ijkl} are computed analytically from the expressions given in Appendix C, being aware that in the present case the indices i, j, k, and l label the single-particle states in a different way and that the integrals depend on the quantum numbers n_x and n_y corresponding to the previous indices.

In the following section, we use a Hilbert space of dimension $D = 17765$ corresponding to $M = 420$ single-particle basis states. In Sec. 6.3, we need a larger Hilbert space, with $M = 812$ and $D = 63035$.

6.2.2   Ground-state energy and degeneracy

In this section, we compute the ground-state energy and concentrate on understanding the way the interaction lifts the degeneracy of the ground-state manifold. To this aim, we compare our direct diagonalization results with approximate expressions for the energy of the ground state manifold. In all cases discussed below, we set the spin-orbit coupling to a non-zero but small value, $\kappa = 0.3$. Larger values of κ are discussed in Sect. 6.3.

In absence of interactions, the ground state is three-fold degenerated. We obtain approximate analytic expressions for the energies of the three states using the six-mode truncation presented in Sect. 6.1.1. The energies of the three states are denoted, E_0^{AA}, E_0^{AB} and E_0^{BB}. Their explicit expressions are provided in Appendix D.2.

The simplest interacting case we consider is when $g_{\uparrow\uparrow} = g_{\downarrow\downarrow} = g_{\uparrow\downarrow} = g$. In this case, the three orthogonal states that define the ground-state subspace remain quasidegenerate (see Fig. 6.5). As we consider a small finite range, $s = 0.5$, the AB state, approximated by Eq. (D.14) at $g \approx 0$, has a slightly different energy within our approximation, and would be truly degenerate with the other two in the limit of $s \to 0$.
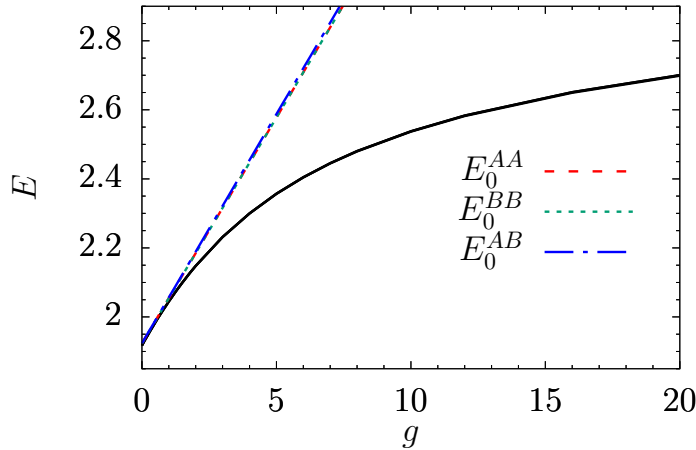
Figure 6.5: The first three energy levels of the two-boson system as a function of $g = g_{\uparrow\uparrow} = g_{\downarrow\downarrow} = g_{\uparrow\downarrow}$ obtained by direct diagonalization (solid black lines). The approximate perturbative calculations are also plotted [see main text for details]. Notice that the three solid black lines overlap and also the dashed and dotted lines. We have used a range $s = 0.5$ and the spin-orbit coupling constant $\kappa = 0.3$.

The three-fold degeneracy of the ground state manifold is lifted whenever the interaction strengths are not equal. For instance, fixing $g_{\downarrow\downarrow} = g_{\uparrow\downarrow} = 0$, and increasing $g_{\uparrow\uparrow}$ we completely break the degeneracy, since the spin-orbit part of the Hamiltonian induces a nonzero, but different, spin-up spin-up component in all three orthogonal two-boson states. Our perturbative calculations are used to identify which energy level corresponds to each kind of state, as we show in Fig. 6.6. For the case of the state of kind AA, the one with a larger spin-up spin-up component, we observe that the prediction of perturbation theory fails for $g_{\uparrow\uparrow} > 1$. In contrast, for the BB state, with a small spin-up spin-up component, its energy is well-approximated perturbatively up to $g_{\uparrow\uparrow} = 20$.

The ground state remains degenerate, although only two-fold, if we set to zero the intraspin interactions, $g_{\downarrow\downarrow} = g_{\uparrow\uparrow} = 0$, and vary the inter-spin one, $g_{\uparrow\downarrow}$. Since the effect on the states of kind AA and BB is the same, they remain degenerate and define the ground-state subspace (see Fig. 6.7). However, the state AB is very sensitive to changes in $g_{\uparrow\downarrow}$, compared to the two previous ones, and its energy increases more rapidly.

The last case we consider is fixing at finite values two of the interaction strengths, e.g. $g_{\downarrow\downarrow}$ and $g_{\uparrow\downarrow}$, and varying the other one, $g_{\uparrow\uparrow}$ (see Fig. 6.8). In this case, we find crossings between the energy levels. The perturbative calculations are useful to predict the value of $g_{\uparrow\uparrow}$ where the crossing occurs, by equating Eqs. (D.15), (D.16) and (D.17), properly, once $g_{\downarrow\downarrow}$ and $g_{\uparrow\downarrow}$ are fixed. In particular, in Fig. 6.8 we see that it happens when $g_{\uparrow\uparrow} = g_{\downarrow\downarrow}$, and also when $g_{\uparrow\uparrow} = g_{\uparrow\downarrow}$.

Finally, we observe that when we further increase the interaction strength, regardless of the spin
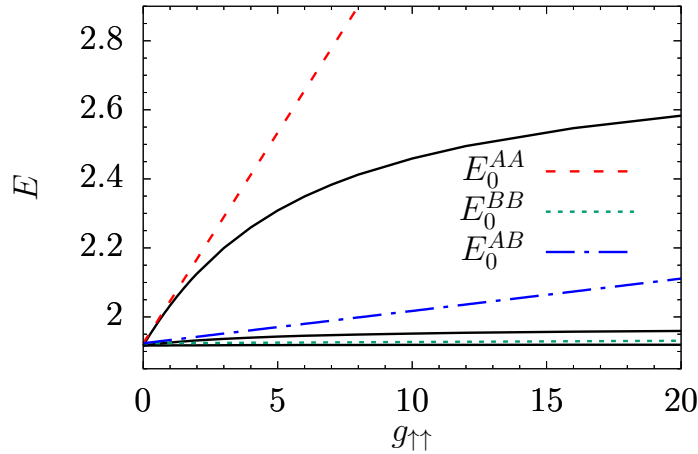
Figure 6.6: The first three energy levels of the two-boson system as a function of $g_{\uparrow\uparrow}$, with $g_{\downarrow\downarrow} = g_{\uparrow\downarrow} = 0$ obtained by direct diagonalization (solid black lines). The approximate perturbative calculations are also plotted [see main text for details]. We have used a range $s = 0.5$ and the spin-orbit coupling constant $\kappa = 0.3$.
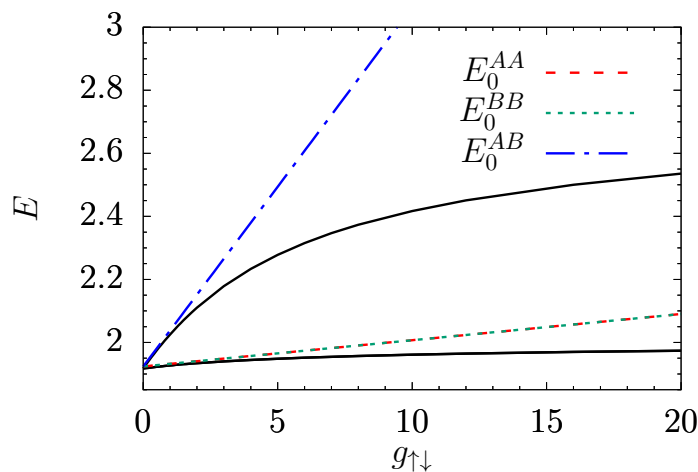

Figure 6.7: The first three energy levels of the two-boson system as a function of $g_{\uparrow\downarrow}$, with $g_{\uparrow\uparrow} = g_{\downarrow\downarrow} = 0$ obtained with direct diagonalization (solid black lines). The approximate perturbative calculations are also plotted [see main text for details]. Notice that two solid black lines and two dashed lines overlap on the bottom part of the figure. We have used a range $s = 0.5$ and the spin-orbit coupling constant $\kappa = 0.3$.

components, the energy levels tend to saturate. This behavior is not captured by the perturbative expressions discussed. This is an indicator that the system becomes correlated in such a way to reduce the total energy by avoiding the atom-atom interaction. This kind of behavior was obtained

6.3. Interaction induced crossover in the $g_{\uparrow\uparrow} = g_{\downarrow\downarrow} = g_{\uparrow\downarrow}$ case
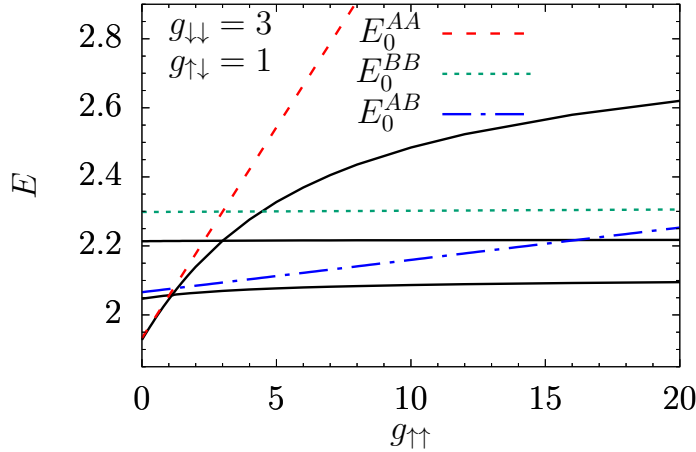
95

Figure 6.8: The first three energy levels of the two-boson system as a function of $g_{\uparrow\uparrow}$, with $g_{\downarrow\downarrow} = 3$ and $g_{\uparrow\downarrow} = 1$, obtained by direct diagonalization (solid black lines). The approximate perturbative calculations are also plotted [see main text for details]. We have used a range $s = 0.5$ and the spin-orbit coupling constant $\kappa = 0.3$.

in a harmonically trapped system of interacting bosons in two dimensions as discussed in Chapters 3 and 4.

6.3 Interaction induced crossover in the $g_{\uparrow\uparrow} = g_{\downarrow\downarrow} = g_{\uparrow\downarrow}$ case

Now, let us broaden our scope and study not only the ground-state manifold but also the lower part of the energy spectrum. The goal is to discuss the combined effects of the spin-orbit term and the atom-atom interaction. For simplicity, we consider the case $g = g_{\uparrow\uparrow} = g_{\downarrow\downarrow} = g_{\uparrow\downarrow}$, with $g > 0$.

The interaction has three main effects, as seen in Fig. 6.9 and Fig. 6.10, where we compare the low energy spectrum for $g = 0$, panel (a), with the corresponding one for $g = 3$, panel (b). In Fig. 6.9 we vary $\kappa \in [0, 1]$, while in Fig. 6.10 we consider a larger region of $\kappa \in [0, 3]$. Due to the repulsive character of the interaction, the energies are shifted to higher values, see for instance the case of the three-fold degenerate ground-state energy level. A second effect, is the breaking of degeneracies. For instance, already at $\kappa = 0$, the first excited state, with degeneracy 8, breaks in two levels with degeneracy 2 for the lowest level and 6 for the highest one. These degeneracies are further broken when increasing κ (see Fig. 6.9). which is the case in the first-excited manifold, corresponding to $E = 3$ at $\kappa = 0$ in panel (a) of Fig. 6.9, where a gap opens and the manifold appears separated in panel (b). Finally, the breaking of degeneracies is accompanied by the presence of more energy-level crossings.

As seen in Fig. 6.10 panel (b), we find a crossing at the ground state level which for $g = 3$
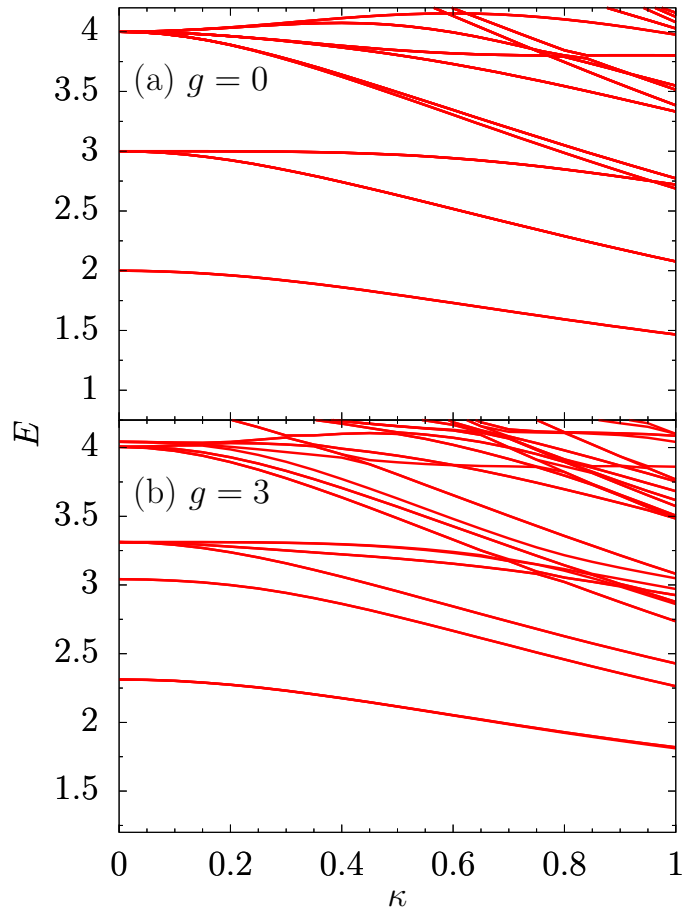
Figure 6.9: Low-energy spectrum of the two-boson system for $\kappa < 1$ with (a) $g = 0$ and (b) $g = 3$. The energies were computed by diagonalization, using $M = 812$ single-particle basis states that corresponds to a Hilbert-space dimension $D = 63035$. We have used a range $s = 0.5$.

appears at $\kappa \approx 2.65$. In the following paragraphs, we concentrate in characterizing this level crossing which corresponds to a change in structure of the ground state induced by the spin-orbit term in the presence of interactions.

Starting from $\kappa = 0$ and $g = 0$, panel (a) of Fig. 6.10, the ground-state is three-fold degenerate. In this case, one could use as a basis of that subspace the two-boson states formed by putting the two bosons in the ground-state of the two-dimensional harmonic trap with parallel spins, both pointing up or both pointing down, and with anti-parallel spins.

For $\kappa > 0$ the previous three states are no longer eigenstates, since the spin-orbit imposes a different structure for the eigenstates at the single-particle level, that was discussed in Sec. 6.1.1. However, the ground-state degeneracy remains unchanged with increasing κ in the noninteracting
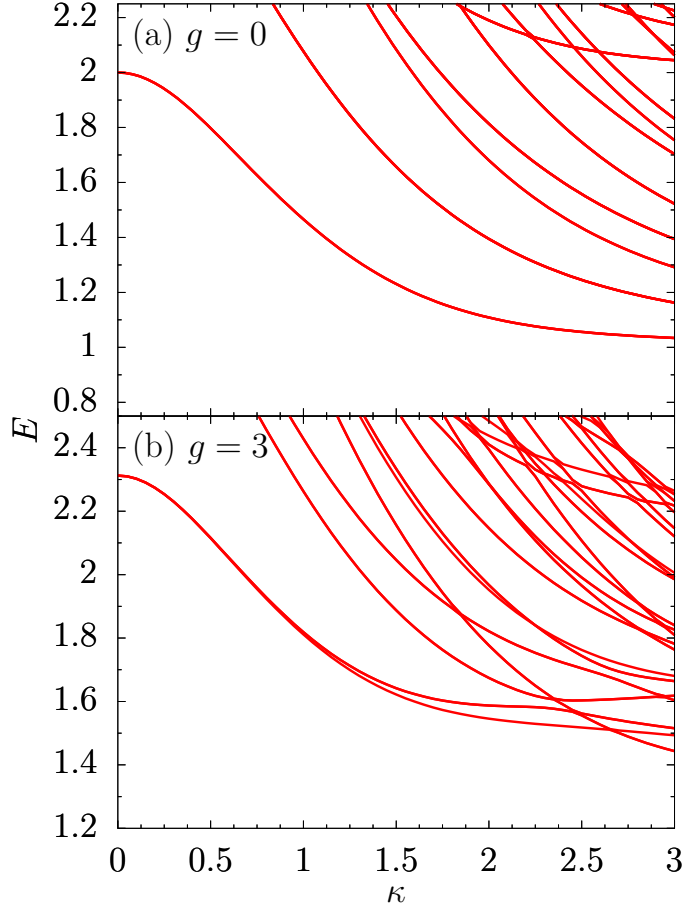
Figure 6.10: The ground-state energy and the first excited states are shown for (a) $g = 0$ and (b) $g = 3$, depending on κ. The energies were computed by diagonalization, using $M = 812$ single-particle basis states that corresponds to a Hilbert-space dimension $D = 63035$. We have used a range $s = 0.5$.

case. The three states that define the ground-state subspace are

$$|\Psi_{0,AA}\rangle = |\psi_{0,A}^{\text{sp}}\rangle |\psi_{0,A}^{\text{sp}}\rangle, \tag{6.20}$$

$$|\Psi_{0,BB}\rangle = |\psi_{0,B}^{\text{sp}}\rangle |\psi_{0,B}^{\text{sp}}\rangle, \tag{6.21}$$

and

$$|\Psi_{0,AB}\rangle = \frac{1}{\sqrt{2}} \left(|\psi_{0,A}^{\text{sp}}\rangle |\psi_{0,B}^{\text{sp}}\rangle + |\psi_{0,B}^{\text{sp}}\rangle |\psi_{0,A}^{\text{sp}}\rangle \right), \tag{6.22}$$

constructed with the two-degenerate single-particle eigenstates, $|\psi_{0,A}^{\text{sp}}\rangle$ and $|\psi_{0,B}^{\text{sp}}\rangle$, of the Hamiltonian in Eq. (6.1).

In the interacting case the three-fold degenerate ground-state subspace splits in two energy levels: the ground state becomes nondegenerate and the first excitation becomes two-fold degenerate.
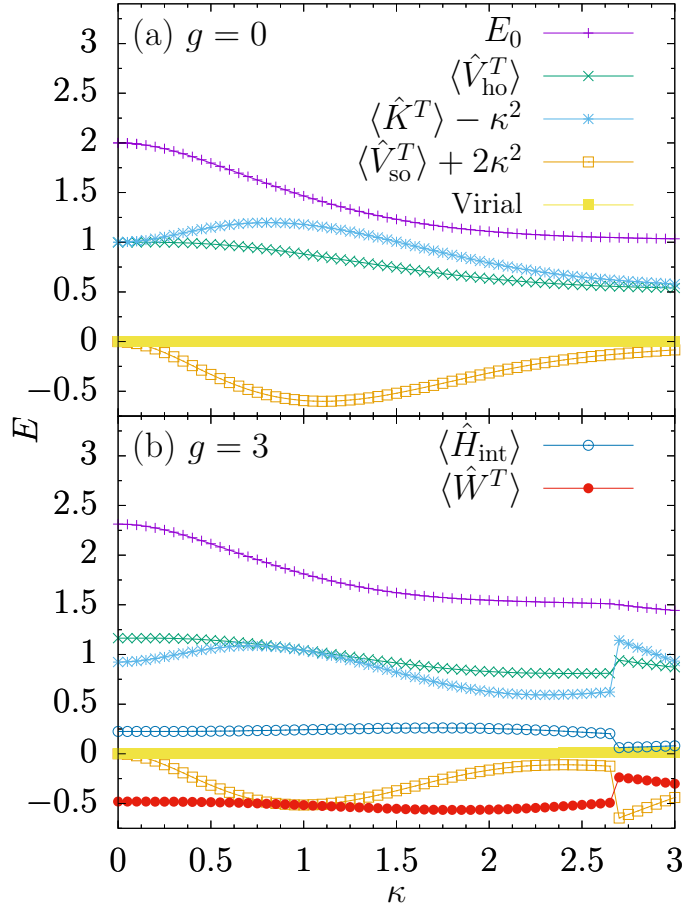
Figure 6.11: The different energy contributions to the two-boson ground-state energy and the terms involved in the virial theorem are depicted depending on the spin-orbit coupling parameter κ. In panel (a) $g = 0$ and in panel (b) $g = 3$. Virial $= 2\langle \hat{V}_{\text{ho}}^T \rangle - 2\langle \hat{K}^T \rangle - \langle \hat{V}_{\text{so}}^T \rangle + \langle \hat{W}^T \rangle$.

This effect is more notorious for larger κ, for instance for $\kappa = 1.5$ in Fig. 6.10 panel (b), where we observe the gap opening. For larger κ we observe the previously mentioned crossing. Then, from $\kappa \approx 2.65$ up to 3, the ground state becomes two-fold degenerate. The level which crosses at $\kappa \approx 2.65$ corresponds to the evolution with κ of a very excited level at $\kappa = 0$. Let us emphasize that this transition is a joint effect of the spin-orbit coupling and the interaction, since it is only observed when both effects are present.

To characterize the crossing in the ground-state energy we have computed its energy contributions in the cases of Fig. 6.10 panels (a) and (b). These results are shown in Fig. 6.11, where we have also tested the fulfillment of the virial theorem energy relation (see Appendix E).

Before the crossing, the dependence on κ of the kinetic, the harmonic potential and the spin-orbit energies is qualitatively similar to the noninteracting case (see Fig. 6.11). In the interacting case, the atoms are farther from the center of the trap resulting in a shift in the harmonic potential
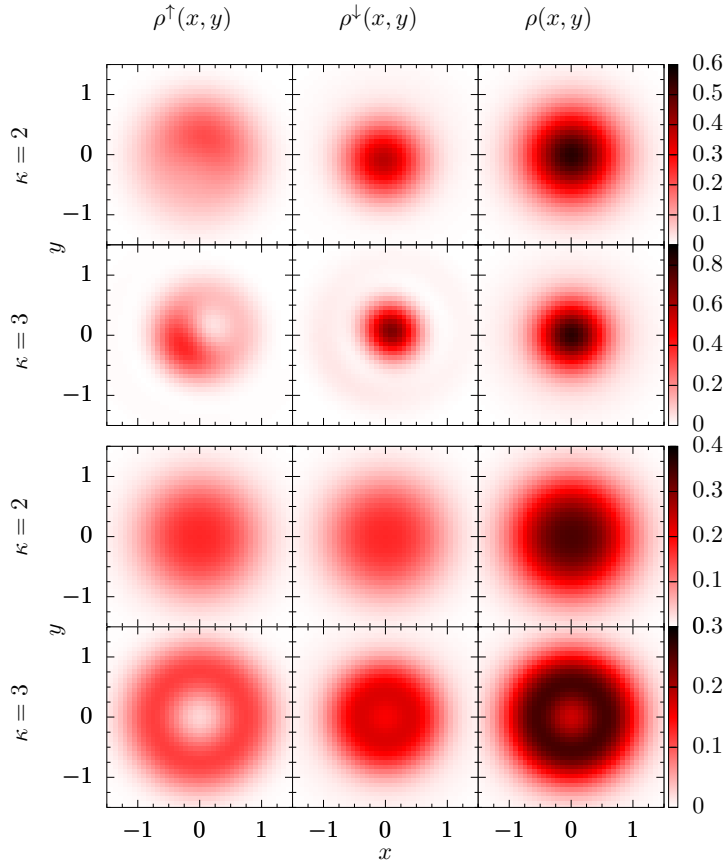
Figure 6.12: Density profiles of each spin-component and the total one for $\kappa = 2$ and $\kappa = 3$. The upper and lower panels correspond to the noninteracting, $g = 0$, and interacting, $g = 3$, cases, respectively.

energy between the $g = 0$ and $g = 3$ cases depicted in Fig. 6.11. The kinetic energy is reduced in the interacting case. The interaction energy and the term coming from the interaction present in the virial relation, $\langle \hat{W}^T \rangle$, are mostly independent of κ. At the crossing, except from the total energy that remains continuous, all other energy terms feature a discontinuity. After the crossing, the ground state has a different structure. In particular, the state is less sensitive to the presence of the repulsive interaction, since the interaction energy is smaller and closer to zero compared to the other energy terms. The harmonic potential and the kinetic energies are larger than before the crossing. Again, this positive terms are compensated by the negative spin-orbit term that is larger in absolute value.

The effects of the crossover become also apparent in the density of the cloud (see Appendix B.1.1 for the explicit expressions). To illustrate this phenomenology we compare the densities for the

$g = 0$ and $g = 3$ cases, for two values before and after the level crossing, $\kappa = 2$ and $\kappa = 3$, respectively. For $\kappa = 2$ we observe that the total density of the cloud is similar in both cases (see Fig. 6.12). The main difference is that the interacting cloud is already larger than the noninteracting one, as expected from the repulsive nature of the atom-atom interactions considered. The densities of the two spin components are different for $g = 0$ and $g = 3$. In the interacting case, both densities are very similar, while in the noninteracting one $\rho^{\downarrow}$ is much smaller and more peaked at the center of the trap. An important effect of the crossing is that the cloud becomes larger after the level crossing, i.e. going from $\kappa = 2$ to $\kappa = 3$ for $g = 3$ (see the total density in Fig. 6.12). This is in contrast with the behavior observed in absence of interactions, where the cloud size gets reduced when going from $\kappa = 2$ to $\kappa = 3$, as seen in Fig. 6.12. This effect is observed also for the densities of each component separately. Another relevant feature is that, after the crossing, the total density has a dip in the center of the trap, while in the noninteracting case it has a maximum.

Chapter 7

SUMMARY AND CONCLUSIONS

In this Chapter, we summarize the contents of the thesis and the main conclusions.

Chapter 2. Methodology and formalism

In this Chapter, we have established the main numerical method used in the thesis: exact diagonalization. We have proposed several strategies to minimizie the size of the Hilbert space while keeping a good quality of the results. We have checked the stability of the method and construct the technology that should allow to consider systems with number larger of particles, or vary the interparticle interaction and the geometry of the trap.

Chapter 3. Few bosons interacting in a two-dimensional harmonic trap

We have studied systems of few bosons trapped in an isotropic 2D harmonic trap interacting by a finite-range Gaussian potential.

First, we have explored in detail the noninteracting case, paying particular attention to the degeneracies of the excitation spectrum of the system. In particular, for the N-boson case, we have explained how to compute the degeneracy of the low-energy states and show its independence respect to the number of particles if it is large enough.

By means of a direct diagonalization of the Hamiltonian in a truncated space, we have studied the interacting system and we have computed the low-energy spectra of the two-, three-, and four-body. We have also proposed a variational ansatz with two-body correlations which provides an accurate description of both the energy and the structure of the ground state in the full range of interaction considered and helps to understand the physical behavior of these systems.

The analysis of the spectra reveals the existence of center-of-mass excitations which are clearly identified. As the interaction is increased, we have shown how the energy of the ground state and of

all low lying states seem to saturate as the interaction strength is increased. The effect of increasing the interaction on the ground state is twofold. On one side, the density at the center of the trap decreases becoming almost flat in the bulk of the gas, with the cloud thus becoming wider. On the other side, the atoms develop strong two-body correlations to avoid the interaction. This is achieved by building holes in the many-body wave function whenever two atoms are at the same position, as is clearly seen in the computed pair correlations or in the explicitly constructed correlated variational wave functions. This mechanism is similar to the one present in the Tonks-Girardeau gas in 1D and is also responsible for the observed saturation of the energies of the system as we increase the interaction strength and reduce the range. Finally, the onset of correlations produces fragmentation on the one-body density matrix, which has been shown to increase with the number of particles. This is an evidence of the existence of correlations beyond the mean-field description

Chapter 4. Fermionic properties of two bosons in a two-dimensional harmonic trap
In two dimensions, the ground state energy of two strongly interacting bosons in a harmonic trap is not equal to the noninteracting two-fermion system in the same potential, contrary to the one-dimensional case. However, the wave function resulting from symmetrizing the corresponding noninteracting fermionic ground state is found to be a very good variational trial wave function if the range of the interaction is properly chosen for a certain value of the interaction strength. This simple variational wave function provides an upper-bound very close to the ground state energy obtained by exact diagonalization and also with a Jastrow-type variational ansatz. Even more, the distribution of the energy between the kinetic and harmonic potential parts is very similar to the one provided by exact diagonalization when the total energy is a good estimation of the ground-state energy. We have shown that the increase of the energy with the interaction strength comes, mostly, from the harmonic potential contribution to the energy since the kinetic energy remains almost constant and the interaction energy is close to zero. In fact, the bosons avoid feeling the interaction by being more separate and, therefore, further from the center of the trap, which is also reflected in the density profiles obtained. The correlations induced by the interaction cause the density profile of the strongly-interacting bosons to tend toward the noninteracting two-fermion profile. For the pair correlation function, we have found qualitatively the same kind of behavior.

Chapter 5. Few-boson localization in a continuum with speckle disorder
One of the open questions associated to the localization of particles in one dimension in the presence of disorder is to elucidate if repulsive interactions can induce delocalization in these systems, which otherwise are localized, according to Anderson's ideas in the absence of interactions. In this Chapter, we have performed a computational investigation to answer this question. While previous computational investigations on this critical issue addressed discrete-lattice models, we

focused here on a model defined in continuous space. Specifically, we considered a one-dimensional model which describes ultracold atoms exposed to random optical speckle patterns, taking into account the structure of the spatial correlations of the disorder field. This is the setup that has been implemented in early cold-atom experiments on the Anderson localization.

The computational procedure we employed is based on exact-diagonalization calculations, combined with the statistical analysis of the levels-spacings statistics familiar from random matrix theory. This is, in fact, one of the most sound criteria commonly employed to identify localized (i.e., nonergodic) phases in noninteracting as well as in interacting disordered systems, where it allows to identify many-body localized phases.

As a preliminary step, we identified the speckle-field intensity required to observe the (Poisson) statistics of localized systems in a finite linear system size that is feasible for our computational approach and for cold-atom experiments.

Our main finding is that, if two or three interacting bosons move in such a speckle field, the localization is stable against zero-range interparticle interactions in a broad range of interaction strengths, ranging from the noninteracting limit, up to moderately strong interactions half way to the strongly-interacting limit. Addressing even stronger interactions is beyond the scope of this study since, on the one hand, it would require larger computational resources and, on the other hand, delocalization effects due to interactions are not expected in this regime since in the strongly-interacting limit the system properties are determined by the single-particle modes. Our results are limited to a low-energy regime, of the order of the speckle-field intensity, where the accuracy of the diagonalization results is under control. It is possible that at higher energies two-body or three-body mobility edges would occur.

Previous studies on the possible occurrence of many-body localization in continuous-space systems have provided contradictory results. The findings reported here establish that in a few-body system localization can be stable against zero-range interactions in a continuous-space models relevant for cold-atom experiments.

Chapter 6. Spin-orbit coupling effects in a two-dimensional harmonic trap

The interpretation of recent experimental developments on the study of spin-orbit effects were demanding for microscopic calculations of the interplay between spin-orbit and interaction effects in bosonic systems. In particular, we have considered one and two bosons with an artificial spin-orbit coupling trapped in a harmonic potential. For the single-particle case, the diagonalization of the Hamiltonian matrix has allowed us to study the properties of the low-energy eigenstates of the system, going from the weak spin-orbit coupling regime to the strong one. We have computed the expectation values of each energy term in the Hamiltonian for the eigenstates, separately, and have derived and tested the virial energy relation between them. In particular, we have found

a relation between the expectation value of different kind of spin-orbit coupling terms, which is independent of the trapping potential. For the ground state of the single-particle system, we have derived approximate analytical expressions that are able to reproduce the ground-state energy in the weak spin-orbit coupling regime and that, for the interacting two-boson system, are used to obtain perturbative expressions that explain the breaking of the degeneracy of the ground-state subspace when changing the values of the spin-dependent interaction strengths. In all cases, we have found that the ground-state energy tends to saturate with increasing interaction, departing from the perturbation-theory prediction. This signals the formation of repulsive correlations in the system. In addition, in the spin-independent interaction case, for the repulsively interacting two-boson system, we have found an abrupt change in the ground-state properties when the spin-orbit coupling parameter is sufficiently large. This transition has been characterized computing the energy contributions to the ground state, that present a discontinuity at the point where there is an energy-level crossing in the ground-state energy. Moreover, this phenomenon has been observed to be apparent in the density profile of the system, which could be experimentally measured. To perform this analysis, and also to test the accuracy of the calculations has been very useful the derivation of the virial theorem in the presence of spin-orbit coupling and finite-range interactions. The numerical calculations fulfill the virial theorem very satisfactory in all the range of spin-orbit coupling and interactions strength explored.

APPENDIX A: COMPUTATION OF DEGENERACIES IN THE NONINTERACTING LIMIT

A.1 The two-boson system in a two-dimensional harmonic trap

We compute the degeneracy of each energy level depending on the excitation energy number, $N_E = E - E_0$, for the two-boson system with the possible states labeled using the quantum numbers of Eq. (3.30). First, we fix the excitation energy number, N_E, and consider it to be even. Then, the values that n_r can take are $n_r = 0, 2, ..., N_E$, so $n_r = 2k$ with $k = 0, 1, ..., N_E/2$. Since we have $n_{cm} + n_r = N_E$, for each value of n_r there is the corresponding n_{cm}. Now, we count the number of states with a given n_r with excitation energy number N_E taking into account the degeneracy due to the quantum numbers m_{cm} and m_r, that is,

$$d_{N_E,k} = (n_{cm} + 1)(n_r + 1) = (N_E - 2k + 1)(2k + 1). \tag{A.1}$$

Therefore, we have to sum over k to find the degeneracy. The sum goes from $k = 0$ to $k = N_E/2$ if N_E is even and to $k = (N_E - 1)/2$ if N_E is odd, which can be generalized using the floor function, summing from $k = 0$ to $k = \lfloor N_E/2 \rfloor$. The degeneracy is

$$
\begin{aligned}
d^b_{N_E} &= \sum_{k=0}^{\lfloor N_E/2 \rfloor} (N_E - 2k + 1)(2k + 1) \\
&= -\frac{1}{3}\left(\left\lfloor \frac{N_E}{2} \right\rfloor + 1\right)\left[4\left\lfloor \frac{N_E}{2} \right\rfloor^2 + (2 - 3N_E)\left\lfloor \frac{N_E}{2} \right\rfloor - 3(N_E + 1)\right].
\end{aligned}
\tag{A.2}
$$

The previous equation, Eq. (A.2), for N_E even is

$$d^b_{N_E} = \frac{1}{12}\left(N_E + 2\right)\left(N_E(N_E + 4) + 6\right), \tag{A.3}$$

and for N_E odd is

$$d^b_{N_E} = \frac{1}{12}\left(N_E + 1\right)\left(N_E(N_E + 5) + 6\right). \tag{A.4}$$

For the spatial fermionic states, which are the ones with $m_r = $ odd and antisymmetric upon exchanging particles 1 and 2, we compute the degeneracy analogously, using that $n_r = $ odd,

$$
\begin{aligned}
d_{N_E}^f &= \sum_{k=0}^{\lfloor N_E/2 \rfloor} (N_E - 2k)(2k + 2) \\
&= -\frac{1}{3} \left(\left\lfloor \frac{N_E}{2} \right\rfloor + 1 \right) \left[4 \left\lfloor \frac{N_E}{2} \right\rfloor^2 + (8 - 3N_E) \left\lfloor \frac{N_E}{2} \right\rfloor - 6N_E \right].
\end{aligned}
\tag{A.5}
$$

A.1.1   Unperturbed energy states

We are also interested in knowing the number of states in each energy level with $m_r \neq 0$. We compute this number of states subtracting from the total number of degenerate states, $d_{N_E}^b$, the ones with $m_r = 0$, that is,

$$
\begin{aligned}
d_{N_E}^U &= d_{N_E}^b - \sum_{k=0}^{\lfloor N_E/2 \rfloor} (N_E - 2k + 1) \\
&= \left(-\frac{4}{3} \left\lfloor \frac{N_E}{2} \right\rfloor + N_E + \frac{1}{3} \right) \left\lfloor \frac{N_E}{2} \right\rfloor \left(\left\lfloor \frac{N_E}{2} \right\rfloor + 1 \right),
\end{aligned}
\tag{A.6}
$$

where we have used Eq. (A.2). As before, we can separate the case with N_E even,

$$
d_{N_E}^U = \frac{1}{12}(N_E + 2)(N_E + 1)N_E,
\tag{A.7}
$$

and the case with N_E odd,

$$
d_{N_E}^U = \frac{1}{12}(N_E + 3)(N_E + 1)(N_E - 1).
\tag{A.8}
$$

APPENDIX B: COMPUTATION OF GROUND-STATE PROPERTIES

B.1 The density profile

B.1.1 First-quantized density operator

For a system of N particles, the density operator in first quantization, normalized to unity, is defined as

$$\hat{\rho}(\vec{x}) \equiv \frac{1}{N} \sum_{i=1}^{N} \delta(\vec{x} - \vec{x}_i). \tag{B.1}$$

The total density is computed as the expectation value of the previous operator. If the atoms have two possible spin components the total density is decomposed as

$$\hat{\rho}(\vec{x}) = \hat{\rho}^{\uparrow}(\vec{x}) + \hat{\rho}^{\downarrow}(\vec{x}), \tag{B.2}$$

with

$$\hat{\rho}^{\uparrow}(\vec{x}) \equiv \frac{1}{N} \sum_{i=1}^{N} \delta(\vec{x} - \vec{x}_i) \left|\uparrow\right\rangle_i \left\langle\uparrow\right|_i \tag{B.3}$$

and

$$\hat{\rho}^{\downarrow}(\vec{x}) \equiv \frac{1}{N} \sum_{i=1}^{N} \delta(\vec{x} - \vec{x}_i) \left|\downarrow\right\rangle_i \left\langle\downarrow\right|_i. \tag{B.4}$$

B.1.2 Density of identical spinless bosons

The density profile for a given state of a system of N identical spinless bosons, $\Psi(\vec{x}_1, ..., \vec{x}_N)$, would be

$$\rho(\vec{x}) = \frac{1}{N} \sum_{i=1}^{N} \int d\vec{x}_1 ... d\vec{x}_N \, \delta(\vec{x} - \vec{x}_i) \left|\Psi(\vec{x}_1, ..., \vec{x}_N)\right|^2 = \int d\vec{x}_2 ... d\vec{x}_N \, \left|\Psi(\vec{x}, \vec{x}_2 ..., \vec{x}_N)\right|^2. \tag{B.5}$$

In particular, for a two-boson system in two dimensions, the previous equation reduces to

$$\rho(x, y) = \int_{-\infty}^{\infty} dx_2 \int_{-\infty}^{\infty} dy_2 \left|\Psi(x, y, x_2, y_2)\right|^2. \tag{B.6}$$

We compute the density profile for the general interacting case, in the harmonic trap, for the ground state of the system as

$$\rho(x, y) = \int_{-\infty}^{\infty} dx_2 \int_{-\infty}^{\infty} dy_2 \frac{2}{\pi} e^{-\frac{1}{2}(\vec{x}+\vec{x}_2)^2} |f(|\vec{x} - \vec{x}_2|)|^2, \tag{B.7}$$

where we have made use of the explicit form of the many-body wave function of the ground state,

$$\Psi(\vec{x}_1, \vec{x}_2) = \sqrt{\frac{2}{\pi}} e^{-\frac{1}{4}(\vec{x}_1+\vec{x}_2)^2} f(|\vec{x}_1 - \vec{x}_2|). \tag{B.8}$$

This way of writing the wave function of the ground state is equivalent to separate the center-of-mass part from the relative part. Using the change of variables $\vec{r} = \vec{x} - \vec{x}_2$ and polar coordinates in Eq. (B.7), we express the density as

$$\begin{aligned}
\rho(x, y) &= \frac{2}{\pi} e^{-2(x^2+y^2)} \int_0^\infty r\, dr\, e^{-\frac{r^2}{2}} |f(r)|^2 \int_0^{2\pi} d\varphi\, e^{-2r(x\cos\varphi + y\sin\varphi)} \\
&= 4 e^{-2(x^2+y^2)} \int_0^\infty r\, dr\, e^{-\frac{r^2}{2}} |f(r)|^2 \mathcal{I}_0\left(2r\sqrt{x^2+y^2}\right).
\end{aligned} \tag{B.9}$$

We have used that

$$\int_0^{2\pi} d\varphi\, e^{A\cos\varphi + B\sin\varphi} = 2\pi\, \mathcal{I}_0\left(\sqrt{A^2 + B^2}\right), \tag{B.10}$$

where $\mathcal{I}_0$ is a modified Bessel function. Notice that, as we would expect, in Eq. (B.9) we have demonstrated that the density only depends on the radial coordinate $X \equiv \sqrt{x^2 + y^2}$, and we can rewrite that equation as

$$\rho(X) = 4 e^{-2X^2} \int_0^\infty r\, dr\, e^{-\frac{r^2}{2}} |f(r)|^2 \mathcal{I}_0(2rX). \tag{B.11}$$

This result is valid not only for our Gaussian-shaped potential but also for any potential dependent only on the modulus of the relative coordinate. In these other cases, the explicit form of the interaction defines the relative wave function $f(r)$. In the noninteracting case, we can compute the integral analytically, by substituting the explicit form of $f_0(r)$,

$$f_0(r) = \frac{1}{\sqrt{2\pi}} e^{-\frac{r^2}{4}}, \tag{B.12}$$

and we recover the known result,

$$\rho_0(X) = \frac{2}{\pi} e^{-2X^2} \int_0^\infty r\, dr\, e^{-r^2} \mathcal{I}_0(2rX) = \frac{1}{\pi} e^{-X^2} = |\varphi_0(X)|^2, \tag{B.13}$$

where $\varphi_0(X)$ is the wave function of the single-particle ground state of the two-dimensional harmonic oscillator. The previous result, $\rho_0(X) = |\varphi_0(X)|^2$, is also valid for the case of N noninteracting bosons in the two-dimensional harmonic potential, since the many-body wave function factorizes, $\Psi_0(\vec{x}_1, \vec{x}_2..., \vec{x}_N) = \varphi_0(\vec{x}_1)...\varphi_0(\vec{x}_N)$. We recover the previous result replacing the factorized wave function into Eq. (B.5).

B.1.3 Second-quantized density operator

For our numerical computations, we make use of the second-quantized form of the density operator,

$$\hat{\rho} = \frac{1}{N} \sum_{i,j=1}^{M} \hat{a}_i^\dagger \hat{a}_j \psi_i^*(\vec{x})\psi_j(\vec{x}). \tag{B.14}$$

For a state written as a sum of Fock states,

$$|\Psi\rangle = \sum_{k=1}^{D} \alpha_k |k\rangle, \tag{B.15}$$

where the index k labels each state of the basis, $|k\rangle = |n_1, ..., n_M\rangle$, and D is the dimension of the Hilbert space, the density profile is computed as

$$\begin{aligned}
\rho(\vec{x}) &= \frac{1}{N} \sum_{k'=1}^{D} \sum_{k=1}^{D} \sum_{i,j=1}^{M} \psi_i^*(\vec{x})\psi_j(\vec{x})\alpha_{k'}^*\alpha_k \langle k'| \hat{a}_i^\dagger \hat{a}_j |k\rangle \\
&= \frac{1}{N} \sum_{k'=1}^{D} \sum_{k=1}^{D} \sum_{i,j=1}^{M} \psi_i^*(\vec{x})\psi_j(\vec{x})\alpha_{k'}^*\alpha_k \langle k'| A_{ij}(k) |p(k)\rangle \\
&= \frac{1}{N} \sum_{k=1}^{D} \sum_{i,j=1}^{M} \psi_i^*(\vec{x})\psi_j(\vec{x})\alpha_{p(k)}^*\alpha_k A_{ij}(k),
\end{aligned} \tag{B.16}$$

where $\psi_i(\vec{x})$ are the single-particle basis states and we have used that $\hat{a}_i^\dagger \hat{a}_j |k\rangle = A_{ij}(k) |p(k)\rangle$, and $\langle k'|p(k)\rangle = \delta_{k',p(k)}$.

B.2 The pair correlation function

The pair correlation operator, normalized to unity, for a system of N particles reads

$$\hat{\eta}(\vec{x},\vec{x}') \equiv \frac{1}{N(N-1)} \sum_{i=1}^{N} \sum_{j \neq i}^{N} \delta(\vec{x}-\vec{x}_i)\delta(\vec{x}'-\vec{x}_j), \tag{B.17}$$

from which we obtain the pair correlation function for a state of the N-boson system, $\Psi(\vec{x}_1, ..., \vec{x}_N)$, as

$$\begin{aligned}
\eta(\vec{x},\vec{x}') &= \frac{1}{N(N-1)} \sum_{i=1}^{N} \sum_{j \neq i}^{N} \int d\vec{x}_1 ... d\vec{x}_N \delta(\vec{x}-\vec{x}_i)\delta(\vec{x}'-\vec{x}_j) |\Psi(\vec{x}_1, ..., \vec{x}_N)|^2 \\
&= \int d\vec{x}_3 ... d\vec{x}_N |\Psi(\vec{x},\vec{x}',\vec{x}_3 ..., \vec{x}_N)|^2.
\end{aligned} \tag{B.18}$$

For the particular case of the ground state of two bosons in two dimensions, we have

$$\eta(\vec{x},\vec{x}') = |\Psi(\vec{x},\vec{x}')|^2, \tag{B.19}$$

where $\Psi(\vec{x},\vec{x}')$ is the corresponding wave function, Eq. (B.8). For the noninteracting case, in the harmonic trap, we know the function of the relative part, Eq. (B.12). In that case, the pair

correlation function is

$$\eta_0\left(\vec{x},\vec{x}'\right) = \frac{1}{\pi^2}e^{-\vec{x}^2}e^{-\vec{x}'^2} = |\varphi_0(\vec{x})|^2\,|\varphi_0(\vec{x}')|^2\,. \tag{B.20}$$

The last result is also valid for the system of N bosons, because then we can factorize, $\Psi_0(\vec{x}_1,\vec{x}_2...,\vec{x}_N) = \varphi_0(\vec{x}_1)\dots\varphi_0(\vec{x}_N)$, and replace the wave function into Eq. (B.18) in order to find the same result.

Now, we fix one particle at the origin, and compute the function

$$\eta\left(x,y\right) \equiv \eta(\vec{x},\vec{0}) = \frac{2}{\pi}e^{-\frac{1}{2}\left(x^2+y^2\right)}\left|f(\sqrt{x^2+y^2})\right|^2\,. \tag{B.21}$$

Notice that the previous function depends only on the radial coordinate $X \equiv \sqrt{x^2+y^2}$, so we can write

$$\eta(X) = \frac{2}{\pi}e^{-\frac{1}{2}X^2}\,|f(X)|^2\,. \tag{B.22}$$

Again, for the noninteracting case we have an analytical expression for the previous function, that reads

$$\eta_0(X) = \frac{1}{\pi^2}e^{-X^2}, \tag{B.23}$$

and is proportional to the density, Eq. (B.13).

The probability density of finding a particle in the space once we have found a particle at the origin is given by the quantity $\eta(X)/\rho(0)$. We verify its normalization to unity in the general case,

$$\int d\vec{x}\,\frac{\eta(\vec{x},\vec{0})}{\rho(\vec{0})} = \frac{\int d\vec{x}\,d\vec{x}_3\dots d\vec{x}_N\left|\Psi(\vec{x},\vec{0},\vec{x}_3\dots,\vec{x}_N)\right|^2}{\int d\vec{x}_2\dots d\vec{x}_N\left|\Psi(\vec{0},\vec{x}_2,\vec{x}_3\dots,\vec{x}_N)\right|^2} = 1, \tag{B.24}$$

where we have used that all the particles are identical, Eq. (B.5) and Eq. (B.18).

B.2.1   Second-quantized pair correlation operator

The second-quantized form of the pair correlation operator is

$$\hat{\eta} = \frac{1}{N(N-1)}\sum_{i,j,p,q=1}^{M}\hat{a}_i^\dagger\hat{a}_p^\dagger\hat{a}_j\hat{a}_q\psi_i^*(\vec{x})\psi_p^*(\vec{x}')\psi_j(\vec{x})\psi_q(\vec{x}'). \tag{B.25}$$

For a state written as a sum of Fock states,

$$|\Psi\rangle = \sum_{k=1}^{D}\alpha_k\,|k\rangle\,, \tag{B.26}$$

where the index k labels each state of the basis, $|k\rangle = |n_1, \ldots, n_M\rangle$, and D is the dimension of the Hilbert space, the density profile is computed as

$$
\begin{aligned}
\eta(\vec{x}, \vec{x}') &= \frac{1}{N(N-1)} \sum_{k'=1}^{D} \sum_{k=1}^{D} \sum_{i,j,p,q=1}^{M} \psi_i^*(\vec{x})\psi_p^*(\vec{x}')\psi_j(\vec{x})\psi_q(\vec{x}')\alpha_{k'}^*\alpha_k \langle k'| \hat{a}_i^\dagger \hat{a}_p^\dagger \hat{a}_j \hat{a}_q |k\rangle \\
&= \frac{1}{N(N-1)} \sum_{k'=1}^{D} \sum_{k=1}^{D} \sum_{i,j,p,q=1}^{M} \psi_i^*(\vec{x})\psi_p^*(\vec{x}')\psi_j(\vec{x})\psi_q(\vec{x}')\alpha_{k'}^*\alpha_k \langle k'| A_{ipjq}(k) |l(k)\rangle \qquad \text{(B.27)} \\
&= \frac{1}{N(N-1)} \sum_{k=1}^{D} \sum_{i,j,p,q=1}^{M} \psi_i^*(\vec{x})\psi_p^*(\vec{x}')\psi_j(\vec{x})\psi_q(\vec{x}')\alpha_{l(k)}^*\alpha_k A_{ipjq}(k),
\end{aligned}
$$

where $\psi_i(\vec{x})$ are the single-particle basis states and we have used that $\hat{a}_i^\dagger \hat{a}_p^\dagger \hat{a}_j \hat{a}_q |k\rangle = A_{ipjq}(k) |l(k)\rangle$, and $\langle k'|l(k)\rangle = \delta_{k',l(k)}$.

B.3 The condensed fraction

The degree of condensation is characterized using the one-body density matrix,

$$
\rho_{i,j}^{|\Psi\rangle} \equiv \frac{1}{N} \langle \Psi| \hat{a}_i^\dagger \hat{a}_j |\Psi\rangle, \qquad \text{(B.28)}
$$

where, $i, j = 1, \ldots, M$. Diagonalizing this matrix, its eigenvalues λ_i are computed, which are the occupations of the corresponding singe-particle eigenstates $|\phi_i\rangle$. The state $|\Psi\rangle$ is fully condensed when $|\Psi\rangle = |\phi_1\rangle^{\otimes N}$ and then, the one-body density matrix has only a single nonzero eigenvalue, $\lambda_1 = 1$. If there is fragmentation in the system, the highest eigenvalue $\lambda_1 < 1$, due to the normalization, $\sum_{i=1}^{M} \lambda_i = 1$.

APPENDIX C: COMPUTATION OF THE INTEGRALS OF INTERACTION

We make an effort to find an analytic expression for the integrals of the interaction part because, in this way, we avoid computing a lot of 4-dimensional integrals numerically, which would mean needing more computational time in order to achieve a good precision before any other calculation. With our method, we have a fast and accurate subroutine that computes V_{ijkl}.

In order to compute the integrals, we write explicitly the single-particle wave functions corresponding to the ith eigenstate of the single-particle Hamiltonian,

$$\psi_{i(n_x,n_y)}(x,y) = N_{n_x} N_{n_y} H_{n_x}(x) H_{n_y}(y) e^{-\frac{x^2+y^2}{2}}, \tag{C.1}$$

with $H_n(x)$ the Hermite polynomials and the normalization constant

$$N_n = \left(\frac{1}{\sqrt{\pi}2^n n!}\right)^{1/2}. \tag{C.2}$$

The Hermite polynomials are written in series representation as

$$H_n(x) = \sum_{m=0}^{\lfloor n/2 \rfloor} \frac{n!(-1)^m 2^{n-2m}}{m!(n-2m)!} x^{n-2m}, \tag{C.3}$$

where $\lfloor n/2 \rfloor$ indicates the floor function of $n/2$. We replace Eq. (C.1) into Eq. (3.10) in order to obtain

$$V_{ijkl} = \frac{1}{\pi s^2} \prod_{i=1}^{4} N_{n_{xi}} N_{n_{yi}} I_{xx'} I_{yy'}, \tag{C.4}$$

with

$$\begin{aligned} I_{xx'} &= \int_{-\infty}^{\infty} dx' H_{n_{x2}}(x') H_{n_{x3}}(x') e^{-Ax'^2} \int_{-\infty}^{\infty} dx H_{n_{x1}}(x) H_{n_{x4}}(x) e^{-Ax^2+Bx} \\ &= \int_{-\infty}^{\infty} dx' H_{n_{x2}}(x') H_{n_{x3}}(x') e^{-Ax'^2} I_x(x'), \end{aligned} \tag{C.5}$$

with the definitions

$$A \equiv 1 + \frac{1}{s^2}, \tag{C.6}$$

$$B \equiv \frac{2x'}{s^2}, \tag{C.7}$$

and analogously for $I_{yy'}$. Now, we use the series representation of the Hermite polynomials, Eq. (C.3), to compute the integral $I_x(x')$,

$$
\begin{aligned}
I_x(x') &= \sum_{k_1=0}^{\lfloor n_{x1}/2 \rfloor} \sum_{k_4=0}^{\lfloor n_{x4}/2 \rfloor} \frac{n_{x1}! n_{x4}! (-1)^{k_1+k_4} 2^Q}{k_1! k_4! (n_{x1}-2k_1)! (n_{x4}-2k_4)!} \int_{-\infty}^{\infty} x^Q e^{-Ax^2+Bx} dx \\
&= \sum_{k_1=0}^{\lfloor n_{x1}/2 \rfloor} \sum_{k_4=0}^{\lfloor n_{x4}/2 \rfloor} \frac{n_{x1}! n_{x4}! (-1)^{k_1+k_4} 2^Q}{k_1! k_4! (n_{x1}-2k_1)! (n_{x4}-2k_4)!} i^{-Q} A^{-\frac{Q+1}{2}} \sqrt{\pi} e^{\frac{B^2}{4A}} U\left(-\frac{Q}{2}; \frac{1}{2}; \frac{-B^2}{4A}\right) \\
&= \sqrt{\frac{\pi}{A}} e^{\frac{B^2}{4A}} \sum_{k_1=0}^{\lfloor n_{x1}/2 \rfloor} \sum_{k_4=0}^{\lfloor n_{x4}/2 \rfloor} \sum_{m=0}^{\lfloor Q/2 \rfloor} \frac{n_{x1}! n_{x4}!}{k_1! k_4! (n_{x1}-2k_1)!} \frac{(-1)^{k_1+k_4} Q!}{(n_{x4}-2k_4)! m! (Q-2m)! A^{Q-m}} B^{Q-2m},
\end{aligned}
$$
$$(C.8)$$

where $U\left(-\frac{Q}{2}; \frac{1}{2}; \frac{-B^2}{4A}\right)$ is a confluent hypergeometric function of the second kind that we have expressed in series and $Q \in \mathbb{N}$ is defined as

$$
Q \equiv n_{x1} + n_{x4} - 2k_1 - 2k_4. \tag{C.9}
$$

The next step is computing the integral in Eq. (C.5) by replacing the explicit form of $I_x(x')$, Eq. (C.8). First, we notice that depending on the parity of the integrand, the integral will be zero since we integrate in a symmetric interval. The possible situations are

$$
\begin{cases}
I_{xx'} = 0 & n_{x1} + n_{x2} + n_{x3} + n_{x4} \text{ odd} \\
I_{xx'} \neq 0 & n_{x1} + n_{x2} + n_{x3} + n_{x4} \text{ even.}
\end{cases} \tag{C.10}
$$

In the second case, we compute the integral replacing again the Hermite polynomials by their series representation and substituting (C.8) into (C.5),

$$
\begin{aligned}
I_{xx'} &= \int_{-\infty}^{\infty} dx' H_{n_{x2}}(x') H_{n_{x3}}(x') e^{-Ax'^2} I_x(x') \\
&= \sum_{k_1=0}^{\lfloor n_{x1}/2 \rfloor} \sum_{k_2=0}^{\lfloor n_{x2}/2 \rfloor} \sum_{k_3=0}^{\lfloor n_{x3}/2 \rfloor} \sum_{k_4=0}^{\lfloor n_{x4}/2 \rfloor} \sum_{m=0}^{\lfloor Q/2 \rfloor} \prod_{i=1}^{4} \frac{n_{xi}!}{k_i! (n_{xi}-2k_i)!} \frac{\sqrt{\pi} Q! (-1)^{\sum_{j=1}^{4} k_j} 2^{Q'} \int_{-\infty}^{\infty} x'^{Q'} e^{-A'x'^2} dx'}{m! (Q-2m)! A^{Q-m+1/2} s^{2Q-4m}} \\
&= \sum_{k_1=0}^{\lfloor n_{x1}/2 \rfloor} \sum_{k_2=0}^{\lfloor n_{x2}/2 \rfloor} \sum_{k_3=0}^{\lfloor n_{x3}/2 \rfloor} \sum_{k_4=0}^{\lfloor n_{x4}/2 \rfloor} \sum_{m=0}^{\lfloor Q/2 \rfloor} \prod_{i=1}^{4} \frac{n_{xi}!}{k_i! (n_{xi}-2k_i)!} \frac{\sqrt{\pi} Q! (-1)^{\sum_{j=1}^{4} k_j} 2^{Q'} A'^{-\frac{Q'+1}{2}} \Gamma\left(\frac{Q'+1}{2}\right)}{m! (Q-2m)! A^{Q-m+1/2} s^{2Q-4m}},
\end{aligned}
$$
$$(C.11)$$

with the definitions

$$
A' \equiv A - \frac{1}{As^4}, \tag{C.12}
$$

$$
Q' \equiv \sum_{i=1}^{4} (n_{xi} - 2k_i) - 2m. \tag{C.13}
$$

The expression is analogous for $I_{yy'}$ and all the sums that appear are finite and have few terms when n_{xi} are small. Now, knowing the form of $I_{xx'}$ and $I_{yy'}$ we have V_{ijkl}. Moreover, many of the integrals are zero

$$\begin{cases} V_{ijkl} = 0 & \sum_{i=1}^{4} n_{xi} \ odd \ \ or \ \ \sum_{i=1}^{4} n_{yi} \ odd \\ V_{ijkl} \neq 0 & \sum_{i=1}^{4} n_{xi} \ even \ \ and \ \ \sum_{i=1}^{4} n_{yi} \ even, \end{cases} \tag{C.14}$$

and we also take profit from the symmetries of $I_{xx'}(n_{x1}, n_{x2}, n_{x3}, n_{x4})$, which verifies

$$I_{xx'}(n_{x1}, n_{x2}, n_{x3}, n_{x4}) = I_{xx'}(n_{x4}, n_{x2}, n_{x3}, n_{x1})$$
$$= I_{xx'}(n_{x1}, n_{x3}, n_{x2}, n_{x4}) = I_{xx'}(n_{x4}, n_{x3}, n_{x2}, n_{x1}). \tag{C.15}$$

Therefore, we are computing four integrals at the same time.

APPENDIX D: ANALYTICAL APPROXIMATIONS IN THE WEAK SPIN-ORBIT COUPLING REGIME

D.1 Single-particle case

In a first approximation, we consider a Hilbert space of dimension 6, where the particle can populate the ground state of the harmonic oscillator or one of the two first-excited states of the trap, considering also the two possible spin orientations. Therefore, we consider the basis $\{|n_x, n_y, m_s\rangle\} = \{|0,0,1\rangle, |0,0,-1\rangle, |1,0,1\rangle, |1,0,-1\rangle, |0,1,1\rangle, |0,1,-1\rangle\}$. In this Hilbert space, we construct the Hamiltonian matrix and diagonalize it analytically with *Mathematica*. In this way, we find approximate expressions for the ground state and its energy depending on the spin-orbit coupling constant κ. The single-particle ground-state energy is approximately given by,

$$E_{0,d=6}^{\mathrm{sp}} = \frac{1}{2}\left(3 - \sqrt{4\kappa^2 + 1}\right) + \frac{\kappa^2}{2}. \tag{D.1}$$

The ground state is two-fold degenerate, and we label with A and B the orthogonal states,

$$|\psi_{0,A}^{\mathrm{sp}}\rangle_{d=6} = -C_0 |0,0,1\rangle + C_1 (i |1,0,-1\rangle - |0,1,-1\rangle), \tag{D.2}$$

and

$$|\psi_{0,B}^{\mathrm{sp}}\rangle_{d=6} = C_0 |0,0,-1\rangle + C_1 (-i |1,0,1\rangle - |0,1,1\rangle), \tag{D.3}$$

where C_0 and C_1 are given by

$$C_0(\kappa) = \frac{\kappa\sqrt{4 + \frac{1+\sqrt{1+4\kappa^2}}{\kappa^2}}}{\sqrt{2 + 8\kappa^2}}, \tag{D.4}$$

and

$$C_1(\kappa) = \frac{1}{\sqrt{4 + \frac{1+\sqrt{1+4\kappa^2}}{\kappa^2}}}. \tag{D.5}$$

Repeating the previous procedure with a Hilbert space of dimension 12, we obtain more accurate expressions for the ground-state energy, given by,

$$E_{0,d=12}^{\mathrm{sp}} = 2 - \sqrt{2\kappa^2 + 1} + \frac{\kappa^2}{2}. \tag{D.6}$$

and also for the coefficients of the two degenerate states

$$|\psi_{0,A}^{\text{sp}}\rangle_{d=12} = -D_0 |0,0,1\rangle + D_1 (i |1,0,-1\rangle - |0,1,-1\rangle) + D_2 (|0,2,1\rangle + |2,0,1\rangle), \tag{D.7}$$

and

$$|\psi_{0,B}^{\text{sp}}\rangle_{d=12} = D_0 |0,0,-1\rangle + D_1 (-i |1,0,1\rangle - |0,1,1\rangle) - D_2 (|0,2,-1\rangle + |2,0,-1\rangle), \tag{D.8}$$

where D_0, D_1 and D_2 are given by

$$D_0(\kappa) = \sqrt{\frac{\kappa^2 + 1 + \sqrt{2\kappa^2 + 1}}{4\kappa^2 + 2}}, \tag{D.9}$$

$$D_1(\kappa) = \frac{\kappa \left(1 + \sqrt{2\kappa^2 + 1}\right)}{2\sqrt{(2\kappa^2 + 1)\left(\kappa^2 + 1 + \sqrt{2\kappa^2 + 1}\right)}}, \tag{D.10}$$

and

$$D_2(\kappa) = \frac{\kappa^2}{2\sqrt{(2\kappa^2 + 1)\left(\kappa^2 + 1 + \sqrt{2\kappa^2 + 1}\right)}}. \tag{D.11}$$

D.2   Two-boson case

Within the first single-particle approximation for small κ, discussed in Sec. 6.1.1, we compute the energy of the following two-boson states:

$$|\Phi_{0,AA}\rangle = |\psi_{0,A}^{\text{sp}}\rangle_{d=6} |\psi_{0,A}^{\text{sp}}\rangle_{d=6}, \tag{D.12}$$

$$|\Phi_{0,BB}\rangle = |\psi_{0,B}^{\text{sp}}\rangle_{d=6} |\psi_{0,B}^{\text{sp}}\rangle_{d=6}, \tag{D.13}$$

and

$$|\Phi_{0,AB}\rangle = \frac{1}{\sqrt{2}} \left(|\psi_{0,A}^{\text{sp}}\rangle_{d=6} |\psi_{0,B}^{\text{sp}}\rangle_{d=6} + |\psi_{0,B}^{\text{sp}}\rangle_{d=6} |\psi_{0,A}^{\text{sp}}\rangle_{d=6}\right), \tag{D.14}$$

up to first order in perturbation theory for the interaction strength parameters $g_{\uparrow\uparrow}$, $g_{\downarrow\downarrow}$, and $g_{\uparrow\downarrow}$. The previous three states describe, approximately, the degenerate two-boson ground-state subspace in the noninteracting limit. The approximation becomes exact in the limit of $\kappa \to 0$. The first part of the energy for all of them is computed multiplying the single-particle energy given in Eq. (6.5) by the number of particles, that is 2. The interaction part arises from computing the expectation values $\langle\Phi_{0,AA}| \hat{H}_{\text{int}} |\Phi_{0,AA}\rangle$, $\langle\Phi_{0,BB}| \hat{H}_{\text{int}} |\Phi_{0,BB}\rangle$, and $\langle\Phi_{0,AB}| \hat{H}_{\text{int}} |\Phi_{0,AB}\rangle$, since $\langle\Phi_{0,AA}| \hat{H}_{\text{int}} |\Phi_{0,BB}\rangle = \langle\Phi_{0,AA}| \hat{H}_{\text{int}} |\Phi_{0,AB}\rangle = \langle\Phi_{0,BB}| \hat{H}_{\text{int}} |\Phi_{0,AB}\rangle = 0$. Therefore, the energies are

$$E_0^{AA} = 3 - \sqrt{4\kappa^2 + 1} + \kappa^2 + \frac{g_{\uparrow\uparrow}C_0^4}{\pi(2 + s^2)} + \frac{g_{\downarrow\downarrow}4C_1^4(2 + 2s^2 + s^4)}{\pi(2 + s^2)^3} + \frac{g_{\uparrow\downarrow}4C_0^2C_1^2}{\pi(2 + s^2)^2}, \tag{D.15}$$

$$E_0^{BB} = 3 - \sqrt{4\kappa^2 + 1} + \kappa^2 + \frac{g_{\downarrow\downarrow}C_0^4}{\pi(2+s^2)} + \frac{g_{\uparrow\uparrow}4C_1^4(2+2s^2+s^4)}{\pi(2+s^2)^3} + \frac{g_{\uparrow\downarrow}4C_0^2C_1^2}{\pi(2+s^2)^2}, \quad \text{(D.16)}$$

and

$$E_0^{AB} = 3 - \sqrt{4\kappa^2 + 1} + \kappa^2 + \frac{(g_{\uparrow\uparrow} + g_{\downarrow\downarrow})\,2C_0^2C_1^2}{\pi(2+s^2)} + g_{\uparrow\downarrow}\left(\frac{C_0^4}{\pi(2+s^2)} - \frac{4C_0^2C_1^2}{\pi(2+s^2)^2} + \frac{8C_1^4}{\pi(2+s^2)^3}\right),$$
$$\text{(D.17)}$$

where C_0 and C_1 depend on κ and are given in Eq. (D.4) and Eq. (D.5) of Appendix D.1, respectively.

A particular limit case of interest is the short-range limit, $s \to 0$. In that case, the previous expressions reduce to

$$E_{0,s\to0}^{AA} = 3 - \sqrt{4\kappa^2 + 1} + \kappa^2 + \frac{g_{\uparrow\uparrow}C_0^4 + g_{\uparrow\downarrow}2C_0^2C_1^2 + g_{\downarrow\downarrow}2C_1^4}{2\pi}, \quad \text{(D.18)}$$

$$E_{0,s\to0}^{BB} = 3 - \sqrt{4\kappa^2 + 1} + \kappa^2 + \frac{g_{\downarrow\downarrow}C_0^4 + g_{\uparrow\downarrow}2C_0^2C_1^2 + g_{\uparrow\uparrow}2C_1^4}{2\pi}, \quad \text{(D.19)}$$

and

$$E_{0,s\to0}^{AB} = 3 - \sqrt{4\kappa^2 + 1} + \kappa^2 + \frac{g_{\uparrow\downarrow}\left(C_0^4 + 2C_1^4\right) + (g_{\uparrow\uparrow} + g_{\downarrow\downarrow} - g_{\uparrow\downarrow})\,2C_0^2C_1^2}{2\pi}. \quad \text{(D.20)}$$

APPENDIX E: VIRIAL RELATIONS

E.1 Virial theorem energy relation

For the eigenstates, $|\Psi_E\rangle$, of the Hamiltonian in (6.14), i.e., $\hat{H}|\Psi_E\rangle = E|\Psi_E\rangle$, the virial theorem establishes that

$$\langle\Psi_E|\,[\hat{H},\hat{\mathcal{O}}^T]\,|\Psi_E\rangle = \langle\psi_E|\left(\hat{H}\hat{\mathcal{O}}^T - \hat{\mathcal{O}}^T\hat{H}\right)|\psi_E\rangle = \langle\psi_E|\left(E\hat{\mathcal{O}}^T - \hat{\mathcal{O}}^T E\right)|\psi_E\rangle = 0, \qquad \text{(E.1)}$$

with $\hat{\mathcal{O}}^T = \sum_{i=1}^{N}(\hat{x}_i\hat{p}_{x_i} + \hat{y}_i\hat{p}_{y_i})$. The explicit computation of the expectation value of the commutator on the left part of the previous equation results in:

$$2\langle\Psi_E|\,\hat{V}_{\text{ho}}^T\,|\Psi_E\rangle - 2\langle\Psi_E|\,\hat{K}^T\,|\Psi_E\rangle - \langle\Psi_E|\,\hat{V}_{\text{so}}^T\,|\Psi_E\rangle$$
$$+ \langle\Psi_E|\,\hat{W}^{\uparrow\uparrow}\,|\Psi_E\rangle + \langle\Psi_E|\,\hat{W}^{\uparrow\downarrow}\,|\Psi_E\rangle + \langle\Psi_E|\,\hat{W}^{\downarrow\downarrow}\,|\Psi_E\rangle = 0, \qquad \text{(E.2)}$$

where the last three terms come from the interaction part of the Hamiltonian (6.16) and the operators involved read:

$$\hat{W}^{\uparrow\uparrow} = -\sum_{i<j}^{N}\frac{2g^{\uparrow\uparrow}}{\pi s^4}(\hat{\boldsymbol{x}}_i - \hat{\boldsymbol{x}}_j)^2 e^{-\frac{(\hat{\boldsymbol{x}}_i - \hat{\boldsymbol{x}}_j)^2}{s^2}}|\!\uparrow\rangle_i|\!\uparrow\rangle_j\,\langle\uparrow|_i\,\langle\uparrow|_j\,, \qquad \text{(E.3)}$$

$$\hat{W}^{\downarrow\downarrow} = -\sum_{i<j}^{N}\frac{2g^{\downarrow\downarrow}}{\pi s^4}(\hat{\boldsymbol{x}}_i - \hat{\boldsymbol{x}}_j)^2 e^{-\frac{(\hat{\boldsymbol{x}}_i - \hat{\boldsymbol{x}}_j)^2}{s^2}}|\!\downarrow\rangle_i|\!\downarrow\rangle_j\,\langle\downarrow|_i\,\langle\downarrow|_j\,, \qquad \text{(E.4)}$$

and

$$\hat{W}^{\uparrow\downarrow} = -\sum_{i<j}^{N}\frac{2g^{\uparrow\downarrow}}{\pi s^4}(\hat{\boldsymbol{x}}_i - \hat{\boldsymbol{x}}_j)^2 e^{-\frac{(\hat{\boldsymbol{x}}_i - \hat{\boldsymbol{x}}_j)^2}{s^2}}\left(|\!\uparrow\rangle_i|\!\downarrow\rangle_j\,\langle\uparrow|_i\,\langle\downarrow|_j + |\!\downarrow\rangle_i|\!\uparrow\rangle_j\,\langle\downarrow|_i\,\langle\uparrow|_j\right). \qquad \text{(E.5)}$$

We also define the operator:

$$\hat{W}^T \equiv \hat{W}^{\uparrow\uparrow} + \hat{W}^{\downarrow\downarrow} + \hat{W}^{\uparrow\downarrow}. \qquad \text{(E.6)}$$

In the noninteracting case, with the relation in Eq. (E.2) we can write the eigenenergies of the Hamiltonian in Eq. (6.14) as:

$$E = 3\langle\Psi_E|\,\hat{V}_{\text{ho}}^T\,|\Psi_E\rangle - \langle\Psi_E|\,\hat{K}^T\,|\Psi_E\rangle + \frac{N\kappa^2}{2}. \qquad \text{(E.7)}$$

In the single-particle case, the virial theorem energy relation, Eq. (E.2), reduces to Eq. (6.12).

E.2   Angular momenta and spin-orbit virial relation

Following the same procedure of previous Sec. E.1, we compute the expectation value of the following commutator:

$$\langle \Psi_E | \, [\hat{H}^{RD}, \hat{\mathcal{O}}^T] \, | \Psi_E \rangle = 0, \tag{E.8}$$

with $\hat{\mathcal{O}}^T = \sum_{i=1}^{N} \kappa \left(\hat{x}_i \hat{\sigma}_{x_i} + \eta \hat{y}_i \hat{\sigma}_{y_i} \right)$. In this case, we have used the general many-body Hamiltonian, that describes a noninteracting system,

$$\hat{H}^{RD} = \hat{V}^T + \hat{K}^T + \hat{V}_{\text{so}}^{RD,T}, \tag{E.9}$$

where the external trap is an arbitrary potential of the form

$$\hat{V}^T = \sum_{i=1}^{N} \hat{V}(\hat{x}_i, \hat{y}_i), \tag{E.10}$$

and the spin-orbit term is a mixture of Rashba and Dresselhaus of the form:

$$\hat{V}_{\text{so}}^{RD,T} = \kappa \sum_{i=1}^{N} \left(\hat{\sigma}_{x_i} \hat{p}_{x_i} + \eta \hat{\sigma}_{y_i} \hat{p}_{y_i} \right). \tag{E.11}$$

As a result, we find that

$$\langle \Psi_E | \, \hat{V}_{\text{so}}^{RD,T} \, | \Psi_E \rangle = -\kappa^2 \left(N \left(1 + \eta^2 \right) + 2\eta \, \langle \Psi_E | \sum_{i=1}^{N} \hat{L}_{z_i} \hat{\sigma}_{z_i} \, | \Psi_E \rangle \right), \tag{E.12}$$

where now, $|\Psi_E\rangle$ are the eigenstates of $\hat{H}^{RD}$. The independence of the external trapping potential arises from the fact that

$$[\hat{V}^T, \hat{\mathcal{O}}^T] = 0. \tag{E.13}$$

In the single-particle case and with a pure Rashba-type spin-orbit coupling the relation of Eq. (E.12) is equivalent to Eq. (6.13).

Bibliography

[1] C. Chin, R. Grimm, P. Julienne, and E. Tiesinga, Rev. Mod. Phys. **82**, 1225 (2010).

[2] L. Pitaevskii and S. Stringari, *Bose-Einstein Condensation*, Clarendon Press (2003).

[3] I. Bloch, J. Dalibard, and W. Zwerger, Rev. Mod. Phys. **80**, 885 (2008).

[4] M. Lewenstein, A. Sanpera, and V. Ahufinger, *Ultracold Atoms in Optical Lattices: Simulating quantum many-body systems*, Oxford University Press (2012).

[5] I. Bloch, Nat. Phys. **1**, 23 (2005).

[6] W. S. Bakr, J. I. Gillen, A. Peng, S. Fölling, and M. Greiner, Nature **462**, 74 (2009).

[7] G. Zürn, F. Serwane, T. Lompe, A. N. Wenz, M. G. Ries, J. E. Bohn, and S. Jochim, Phys. Rev. Lett. **108**, 075303 (2012).

[8] D. Blume, Rep. Prog. Phys. **75**, 046401 (2012).

[9] T. Langen, R. Geiger, and J. Schmiedmayer, Annu. Rev. Condens. Matter Phys. **6**, 201 (2015).

[10] D. Guéry-Odelin, A. Ruschhaupt, A. Kiely, E. Torrontegui, S. Martínez-Garaot, and J. G. Muga, arXiv:1904.08448.

[11] I. Bloch, J. Dalibard, and S. Nascimbène, Nat. Phys. **8**, 267 (2012).

[12] C. Gross and I. Bloch, Science **357**, 995 (2017).

[13] P. Mujal, E. Sarlé, A. Polls, and B. Juliá-Díaz, Phys. Rev. A **96**, 043614 (2017).

[14] W. S. Bakr, A. Peng, M. E. Tai, R. Ma, J. Simon, J. I. Gillen, S. Fölling, L. Pollet, and M. Greiner, Science **329**, 547 (2010).

[15] J. F. Sherson, C. Weitenberg, M. Endres, M. Cheneau, I. Bloch, and S. Khur, Nature **467**, 68 (2010).

[16] R. Islam, R. Ma, P. M. Preiss, M. E. Tai, A. Lukin, M. Rispoli, and M. Greiner, Nature **528**, 77 (2015).

[17] M. Girardeau, J. Math. Phys. **1**, 516 (1960).

[18] B. Paredes, A. Widera, V. Murg, O. Mandel, S. Fölling, I. Cirac, G. V. Shlyapnikov, T. W. Hänsch, and I. Bloch, Nature **429**, 277 (2004).

[19] T. Kinoshita, T. Wenger, and D. S. Weiss, Science **305**, 1125 (2004).

[20] G. Pupillo, A. M. Rey, C. J. Williams, and C. W. Clark, New J. Phys. **8**, 161 (2006).

[21] M. A. García-March, B. Juliá-Díaz, G. E. Astrakharchik, Th. Busch, J. Boronat, and A. Polls, Phys. Rev. A **88**, 063604 (2013).

[22] M. A. García-March, B. Juliá-Díaz, G. E. Astrakharchik, Th. Busch, J. Boronat, and A. Polls, New J. Phys. **16**, 103004 (2014).

[23] M. Pyzh, S. Krönke, C. Weitenberg, and P. Schmelcher, New J. Phys. **20**, 015006 (2018).

[24] E. Tempfli, S. Zöllner, and P. Schmelcher, New J. Phys. **10**, 103021 (2008).

[25] F. Deuretzbacher, J. C. Cremon, and S. M. Reimann, Phys. Rev. A **81**, 063616 (2010).

[26] P. Kościk, Few-Body Syst. **52**, 49 (2012).

[27] R. E. Barfknecht, A. S. Dehkharghani, A. Foerster, and N. T. Zinner, J. Phys. B: At. Mol. Opt. Phys. **49**, 135301 (2016).

[28] M. A. García-March, B. Juliá-Díaz, G. E. Astrakharchik, J. Boronat, and A. Polls, Phys. Rev. A **90**, 063605 (2014).

[29] B. Wilson, A. Foerster, C.C.N. Kuhn, I. Roditi, and D. Rubeni, Phys. Lett. A **378**, 1065 (2014).

[30] T. Busch, B.-G. Englert, K. Rzazewski, and M. Wilkens, Found. Phys. **28**, 549 (1998).

[31] R. A. Doganov, S. Klaiman, O. E. Alon, A. I. Streltsov, and L. S. Cederbaum, Phys. Rev. A **87**, 033631 (2013).

[32] X.-J. Liu, H. Hu, and P. D. Drummond, Phys. Rev. B **82**, 054524 (2010).

[33] J. Christensson, C. Forssén, S. Åberg, and S. M. Reimann, Phys. Rev. A **79**, 012707 (2009).

[34] M. Imran and M. A. H. Ahsan, Adv. Sci. Lett. **21**, 2764 (2015).

[35] M. Imran and M. A. H. Ahsan, arXiv:1511.03165.

[36] O. I. Kartavtsev and A. V. Malykh, Phys. Rev. A **74**, 042506 (2006).

[37] P. Shea, B. P. van Zyl, R. K. Bhaduri, Am. J. Phys. **77**, 511 (2009).

[38] A. Farrell and B. P. van Zyl, J. Phys. A Math. Theor. **43**, 015302 (2010).

[39] N. T. Zinner, J. Phys. A Math. Theor. **45**, 205302 (2012).

[40] K. M. Daily, X. Y. Yin, and D. Blume, Phys. Rev. A **85**, 053614 (2012).

[41] I. Stetcu, B. R. Barrett, U. van Kolck, and J. P. Vary, Phys. Rev. A **76**, 063613 (2007).

[42] X.-J. Liu, H. Hu, and P. D. Drummond, Phys. Rev. A **82**, 023619 (2010).

[43] P. Mujal, A. Polls, and B. Juliá-Díaz, Condens. Matter **3(1)**, 9 (2018).

[44] M. D. Girardeau, E. M. Wright, and J. M. Triscari, Phys. Rev. A **63**, 033601 (2001).

[45] P. Kościk and T. Sowiński, Sci. Rep. **8**, 48 (2018).

[46] I. Brouzos and P. Schmelcher, Phys. Rev. Lett. **108**, 045301 (2012).

[47] I. Romanovsky, C. Yannouleas, and U. Landman, Phys. Rev. Lett. **93**, 230405 (2004).

[48] P. Mujal, A. Polls, S. Pilati, and B. Juliá-Díaz, Phys. Rev. A **100**, 013603 (2019).

[49] P. W. Anderson, Phys. Rev. **109**, 1492 (1958).

[50] L. Fleishman and P. W. Anderson, Phys. Rev. B **21**, 2366 (1980).

[51] M. P. A. Fisher, P. B. Weichman, G. Grinstein, and D. S. Fisher, Phys. Rev. B **40**, 546 (1989).

[52] B. L. Altshuler, Yu. Gefen, A. Kamenev, and L. S. Levitov, Phys. Rev. Lett. **78**, 2803 (1997).

[53] I. V. Gornyi, A. D. Mirlin, and D. G. Polyakov, Phys. Rev. Lett. **95**, 206603 (2005).

[54] D. M. Basko, I. L. Aleiner, and B. L. Altshuler, Ann. Phys. (Amsterdam) **321**, 1126 (2006).

[55] I. L. Aleiner, B. L. Altshuler, and G. V. Shlyapnikov, Nat. Phys. **6**, 900 (2010).

[56] G. Bertoli, V. P. Michal, B. L. Altshuler, and G. V. Shlyapnikov, Phys. Rev. Lett. **121**, 030403 (2018).

[57] R. Nandkishore, Phys. Rev. B **90**, 184204 (2014).

[58] I. V. Gornyi, A. D. Mirlin, M. Müller, and D. G. Polyakov, Ann. Phys. (Berlin) **529**, 1600365 (2017).

[59] F. Ancilotto, D. Rossini, S. Pilati, Phys. Rev. B **97**, 155107 (2018).

[60] M. Schreiber, S. S. Hodgman, P. Bordia, H. P. Lüschen, M. H. Fischer, R. Vosk, E. Altman, U. Schneider, and I. Bloch, Science **349**, 842 (2015).

[61] H. P. Lüschen, P. Bordia, S. Scherg, F. Alet, E. Altman, U. Schneider, and I. Bloch, Phys. Rev. Lett. **119**, 260401 (2017).

[62] J.-Y. Choi, S. Hild, J. Zeiher, P. Schauss, A. Rubio-Abadal, T. Yefsah, V. Khemani, D. A. Huse, I. Bloch, C. Gross, Science **352**, 1547 (2016).

[63] A. Lukin, M. Rispoli, R. Schittko, M. E. Tai, A. M. Kaufman, S. Choi, V. Khemani, J. Léonard, M. Greiner, Science **364**, 6437, 256 (2019).

[64] P. Lugan, D. Clément, P. Bouyer, A. Aspect, M. Lewenstein, and L. Sanchez-Palencia, Phys. Rev. Lett. **98**, 170403 (2007).

[65] M. Piraud, P. Lugan, P. Bouyer, A. Aspect, and L. Sanchez-Palencia, Phys. Rev. A **83**, 031603(R) (2011).

[66] P. Mujal, A. Polls, and B. Juliá-Díaz, arXiv:1907.13355.

[67] J. Dalibard, F. Gerbier, G. Juzeliūnas, and P. Öhberg, Rev. Mod. Phys. **83**, 1523 (2011).

[68] V. Galitski and I. B. Spielman, Nature **494**, 49 (2013).

[69] N. Goldman, G. Juzeliūnas, P. Öhberg, and I. B. Spielman, Rep. Prog. Phys. **77**, 126401 (2014).

[70] H. Zhai, Rep. Prog. Phys. **78**, 026001 (2015).

[71] A. Machon, H. C. Koo, J. Nitta, S. M. Frolov, and R. A. Duine, Nat. Mater. **14**, 871 (2015).

[72] Y. Zhang, M. E. Mossman, T. Busch, P. Engels, and C. Zhang, Front. Phys. **11**, 118103 (2016).

[73] Y.-J. Lin, K. Jiménez-García, and I. B. Spielman, Nature **471**, 83 (2011).

[74] S.-C. Ji, J.-Y. Zhang, L. Zhang, Z.-D. Du, W. Zheng, Y.-J. Deng, H. Zhai, S. Chen, and J.-W. Pan, Nat. Phys. **10**, 314 (2014).

[75] X. Luo, L. Wu, J. Chen, Q. Guan, K. Gao, Z.-F. Xu, L. You, and R. Wang, Sci. Rep. **6**, 18983 (2016).

[76] Z. Wu, L. Zhang, W. Sun, Z.-T. Xu, B.-Z. Wang, S.-C. Ji, Y. Deng, S. Chen, X.-J. Liu, and J.-W. Pan, Science **354**, 6308 (2016).

[77] F. Grusdt, T. Li, I. Bloch, and E. Demler, Phys. Rev. A **95**, 063617 (2017).

[78] D. Yamamoto, I. B. Spielman, and C. A. R. Sá de Melo, Phys. Rev. A **96**, 061603(R) (2017).

[79] M. A. Khamechi, K. Hossain, M. E. Mossman, Y. Zhang, T. Busch, M. M. Forbes, and P. Engels, Phys. Rev. Lett. **118**, 155301 (2017).

[80] C. Wang, C. Gao, C.-M. Jian, and H. Zhai, Phys. Rev. Lett. **105**, 160403 (2010).

[81] Y. Li, L. P. Pitaevskii, and S. Stringari, Phys. Rev. Lett. **108**, 225301 (2012).

[82] T. Ozawa and G. Baym, Phys. Rev. A **85**, 013612 (2012).

[83] T. Ozawa and G. Baym, Phys. Rev. Lett. **109**, 025301 (2012).

[84] T. Ozawa and G. Baym, Phys. Rev. Lett. **110**, 085304 (2013)

[85] G. Baym and T. Ozawa, J. Phys.: Conf. Ser. **529**, 012006 (2014).

[86] E. Kawasaki and M. Holzmann, Phys. Rev. A **95**, 051601(R) (2017).

[87] S. Sinha, R. Nath, and L. Santos, Phys. Rev. Lett. **107**, 270401 (2011).

[88] H. Hu, B. Ramachandhran, H. Pu, and X.-J. Liu, Phys. Rev. Lett. **108**, 010402 (2012).

[89] Y. Li, X. Zhou, and C. Wu, Phys. Rev. B **85**, 125122 (2012).

[90] B. M. Anderson and C. W. Clark, J. Phys. B: At. Mol. Opt. Phys. **46**, 134003 (2013).

[91] X. Zhou, Y. Li, Z. Cai and C. Wu, J. Phys. B: At. Mol. Opt. Phys. **46** 134001 (2013).

[92] O. V. Marchukov, A. G. Volosniev, D. V. Fedorov, A. S. Jensen, and N. T. Zinner, J. Phys. B: At. Mol. Opt. Phys. **46** 134012 (2013).

[93] O. V. Marchukov, A. G. Volosniev, D. V. Fedorov, A. S. Jensen, and N. T. Zinner, J. Phys. B: At. Mol. Opt. Phys. **47**, 195303 (2014).

[94] X-F. Zhou, J. Zhou and C. Wu, Phys. Rev. A **84** 063624 (2011).

[95] B. Ramachandhran, B. Opanchuk, X.-J. Liu, H. Pu, P. D. Drummond, and H. Hu, Phys. Rev. A **85**, 023606 (2012).

[96] J. Armaitis, J. Ruseckas, H. T. C. Stoof, and R. A. Duine, Phys. Rev. A **96**, 053625 (2017).

[97] X. Y. Yin, S. Gopalakrishnan, and D. Blume, Phys. Rev. A **89**, 033606 (2014).

[98] Q. Guan, X. Y. Yin, S. E. Gharashi, and D. Blume, J. Phys. B: At. Mol. Opt. Phys. **47**, 161001 (2014).

[99] C. D. Schillaci and T. C. Luu, Phys. Rev. A **91**, 043606 (2015).

[100] Q. Guan and D. Blume, Phys. Rev. A **92**, 023641 (2015).

[101] B. Ramachandhran, H. Hu, H. Pu, Phys. Rev. A **87**, 033627 (2013).

[102] J. Sánchez-Baena, J. Boronat, F. Mazzanti, Phys. Rev. A **98**, 053632 (2018).

[103] D. Raventós, T. Graß, M.Lewenstein, and B. Juliá-Díaz, J. Phys. B: At. Mol. Opt. Phys. 50, 113001 (2017).

[104] M. Płodzień, D. Wiater, A. Chrostowski, and T. Sowiński, arXiv:1803.08387.

[105] J. H. Bruinier and K. Ono, Adv. Math. **246**, 198 (2013).

[106] Y. Choliy and A. V. Sills, Ann. Comb. **20**, 301 (2016).

[107] http://oeis.org/A005380

[108] http://oeis.org/A000219

[109] Q. Guan, V. Klinkhamer, R. Klemt, J. H. Becher, A. Bergschneider, P. M. Preiss, S. Jochim, and D. Blume, Phys. Rev. Lett. **122**, 083401 (2019).

[110] T. M. Whitehead, L. M. Schonenberg, N. Kongsuwan, R. J. Needs, and G. J. Conduit, Phys. Rev. A **93**, 042702 (2016).

[111] S. Klaiman, A. U. J. Lode, A. I. Streltsov, L. S. Cederbaum, and O. E. Alon, Phys. Rev. A **90**, 043620 (2014).

[112] G. C. Katsimiga, S. I. Mistakidis, G. M. Koutentakis, P. G. Kevrekidis, and P. Schmelcher, New J. Phys. **19**, 123012 (2017).

[113] V. J. Bolsinger, S. Krönke, and P. Schmelcher, J. Phys. B At. Mol. Opt. Phys. **50**, 034003 (2017).

[114] P. Jeszenski, A. Y. Cherny, and J. Brand, Phys. Rev. A **97**, 042708 (2018).

[115] M. Wouters, J. Tempere, and J. T. Devreese, Phys. Rev. A **68**, 053603 (2003).

[116] R. Jastrow, Phys. Rev. **98**, 1479 (1955).

[117] P. Kościk, M. Płodzień, and T. Sowiński, Europhys. Lett. **123**, 36001 (2018).

[118] N. L. Harshman, Few-Body Syst. **57**, 11 (2016).

[119] J. Reidl, G. Bene, R. Graham, and P. Szépfalusy, Phys. Rev. A **63**, 043605 (2001).

[120] M. Pyzh, S. Krönke, C. Weitenberg, and P. Schmelcher, New J. Phys. **21**, 053013 (2019).

[121] M. McDonald, J. Trisnadi, K.-X. Yao, and C. Chin, Phys. Rev. X **9**, 021001 (2019).

[122] S. Subhankar, Y. Wang, T.-C. Tsui, S. L. Rolston, and J. V. Porto, Phys. Rev. X **9**, 021002 (2019).

[123] B. Hirshberg, V. Rizzi, and M. Parrinello, arXiv:1905.09053.

[124] G. Roati, C. D'Errico, L. Fallani, M. Fattori, C. Fort, M. Zaccanti, G. Modugno, M. Modugno, M. Inguscio, Nature **453**, 895 (2008).

[125] J. Billy, V. Josse, Z. Zuo, A. Bernard, B. Hambrecht, P. Lugan, David Clément, L. Sanchez-Palencia, P. Bouyer, A. Aspect, Nature **453**, 891 (2008).

[126] M. L. Mehta, Random Matrices (Academic, Amsterdam, 2004).

[127] F. Haake, Quantum Signatures of Chaos (Springer, Berlin, 2010).

[128] B. I. Shklovskii, B. Shapiro, B. R. Sears, P. Lambrianides, and H. B. Shore, Phys. Rev. B **47**, 11487 (1993).

[129] E. Hofstetter and M. Schreiber, Phys. Rev. B **49**, 14726 (1994).

[130] F. Milde, R. A. Römer, and M. Schreiber, Phys. Rev. B **61**, 6028 (2000).

[131] L. Schweitzer and H. Potempa, J. Phys. Condens. Matter **10**, L431 (1998).

[132] E. Fratini and S. Pilati, Phys. Rev. A **91**, 061601(R) (2015).

[133] E. Fratini and S. Pilati, Phys. Rev. A **92**, 063621 (2015).

[134] V. Oganesyan and D. A. Huse, Phys. Rev. B **75**, 155111 (2007).

[135] A. Pal, and D. A. Huse, Phys. Rev. B **82**, 174411 (2010).

[136] E. Cuevas, M. Feigel'man, L. Ioffe, and M. Mezard, Nat. Commun. **3**, 1128 (2012).

[137] D. J. Luitz, N. Laflorencie, and F. Alet, Phys. Rev. B **91**, 081103(R) (2015).

[138] C. R. Laumann, A. Pal, and A. Scardicchio, Phys. Rev. Lett. **113**, 200405 (2014).

[139] P. Naldesi, E. Ercolessi, T. Roscilde, SciPost Phys. **1**, 010 (2016).

[140] P. Sierant, D. Delande, J. Zakrzewski, Phys. Rev. A **95**, 021601 (2017).

[141] P. Sierant, J. Zakrzewski, New J. Phys. **20**, 043032 (2018).

[142] J. Goodman, Speckle Phenomena in Optics: Theory and Applications (Roberts, Englewood, CO, 2007).

[143] M. Olshanii, Phys. Rev. Lett. **81**, 938 (1998).

[144] J. M. Huntley, Appl. Opt. **28**, 4316 (1989).

[145] M. Modugno, Phys. Rev. A **73**, 013606 (2006).

[146] T. Okamoto and S. Fujita, J. Opt. Soc. Am. A **25**, 3030 (2008).

[147] S. Pilati, S. Giorgini, M. Modugno, and N. Prokof'ev, New J. Phys. **12**, 073003 (2010).

[148] D.L. Shepelyansky, Phys. Rev. Lett. **73**, 2607 (1994).

[149] F. Stellin and G. Orso, Phys. Rev. B **99**, 224209 (2019).

[150] M. Hilke and E. Hichem, Ann. Phys. **529**, 1600347 (2017).

[151] E. Abrahams, P. W. Anderson, D. C. Licciardello, and T. V. Ramakrishnan, Phys. Rev. Lett. **42**, 673 (1979).

[152] A. Weinrib, Phys. Rev. B **26**, 1352 (1982).

[153] F. Jendrzejewski, A. Bernard, K. Müller, P. Cheinet, V. Josse, M. Piraud, L. Pezzé, L. Sanchez-Palencia, A. Aspect, and P. Bouyer, Nat. Phys. **8**, 398 (2012).

[154] Y. Y. Atas, E. Bogomolny, O. Giraud, and G. Roux, Phys. Rev. Lett. **110**, 084101 (2013).

[155] F. Deuretzbacher, K. Bongs, K. Sengstock, D. Pfannkuche, Phys. Rev. A **75**, 013614 (2007).